This is to certify that the

thesis entitled

THE EFFECT OF LASER INDUCED SURFACE MELTING
AND CUTTING ON CORDIERITE SUBSTRATES

presented by

Vincent J. Pilletteri

has been accepted towards fulfillment
of the requirements for

M.S. degree in Materials Science and
Engineering

Eldon D. Case

Major professor

Date August 28, 1989

THE EFFECT OF LASER INDUCED SURFACE MELTING AND CUTTING ON CORDIERITE SUBSTRATES

BY

VINCENT PILLETTERI

A THESIS

Submitted to
Michigan State University
in partial fulfillment of the requirements
for the degree of

MASTER OF SCIENCE

Department of Metallurgy, Mechanics
and Materials Science

August 1989

ABSTRACT

THE EFFECT OF LASER INDUCED SURFACE MELTING AND CUTTING ON CORDIERITE SUBSTRATES

BY

Vincent Pilletteri

Thin, porous cordierite substrates (nominally $2MgO*2Al_2O_3*5SiO_2$) were laser surface-processed using a 2 kilowatt continuous carbon dioxide laser and a pulsed Nd:YAG laser. This laser treatment successfully eliminated surface porosity, which reduced the potential for the deleterious effects of water absorption. The CO_2 laser also successfully cut the specimens and simultaneously sealed these edges, thereby reducing the potential for water absorption through the sides of the specimen. Scanning Electron Micrographs illustrate these effects. Surface Profilometer traces show that the average surface roughness of laser treated specimens has been reduced by at least 37,000 angstroms. This is a conservative estimate since the Dektak IIA is not sensitive to small pores (these pores are studied with the scanning electron microscope). X-ray diffraction experiments showed the existance of a glass in the melted layer. Thermal anneals at temperatures up to $900^{o}C$ partially recrystallized the glassy phase in the surface layer.

DEDICATION

I would like to dedicate this work to my parents, Carl and Judy. Without their support and encouragement, I could not have made it this far. I love you, and thanks.

ACKNOWLEDGEMENTS

I would like to thank Dr. Eldon Case for his advice, assistance, and enthusiasm through the duration of this project.

I would also like to thank Dr. Kalinath Mukherjee, Narendra Dahotre, and Dr. Parwaiz Khan for their assistance with the carbon dioxide and YAG lasers.

I would also like to thank Chris Fetters for his assistance with the technical drawings.

TABLE OF CONTENTS

List of Tables

List of Figures

Laser Surface Processing of Cordierite

Introduction

1.1 MATERIALS AND METHODS

Cordierite ceramics (nominally $2MgO*2Al_2O_3*5SiO_2$) are particularly useful, since they have a very low coefficient of thermal expansion (i.e. good thermal shock resistance) [1]. This thermal shock resistance is based on the extent of crack propagation or retained load-bearing ability following the initiation of thermal stress fracture [2].

The thermal expansion of cordierite can vary with the processing technique [3]. For example, extrusion of high purity cordierite ceramics can result in unusually low thermal expansions because of the orientation of the cordierite crystallites with their low expansion direction parallel to the plane of extrusion [4].

Cordierite has been used to manufacture items such as rotary generators because of its high-temperature capabilities and good corrosion resistance [5]. Appendix A lists the physical, mechanical, thermal, and electrical properties of cordierite. This material has also been used for automobile exhaust gas control, gas turbine engines, and and industrial heat exchangers [6]. Other uses include heating element supports and burner tips [7]. Cordierite's good thermal shock resistance and its relatively low dielectric constant make it useful as a microwave substrate material.

This thesis will focus the use of cordierite as an electronic substrate material.

The cordierite specimens have been tape cast into easily handled microwave substrate materials. The high density (> 95 percent of theoretical) obtainable for the cordierite yields dielectric constants in the 4.2 to 4.6 range. The dielectric constant ϵ', and the loss tangent $\tan\delta$, can be modified for a given substrate material by varying the processing conditions. For example, by underfiring cordierite bodies to lower densities, dielectric constants in the 3 to 4 range can be obtained. However, this type of processing is not very efficient in terms of repeat production of good cordierite substrates. When a cordierite body is underfired, sintering will not eliminate the porosity within the inner-bulk of the material. Therefore, the specimen will contain hidden voids and pores which will serve to inhibit the strength of the material. The cordierite substrates studied in this thesis have the following properties: 1) an as-received density of 2.54 g/cc, 2) a dielectric constant of 3.0, and 3) a loss tangent of 0.0001 [8].

For high frequency, high speed electronic applications [9], the heat losses in an electronic material are proportional to the angular frequency of the signal, the dielectric constant of the material, and the electric field strength. This concept can be illustrated in the following manner: the heat energy, Q, produced in the substrate (per unit time) is the product I * V of the electrical current I

and the voltage V. Q is expressed in units of watts or energy per unit time. The heat produced per unit volume is thus

$$q(\text{density}) = Q/\text{volume} = I/A * V/d = J\ E \qquad (1)$$

where Q is heat produced, I/A is the current density (J), and V/d is electric field strength (E). For this dielectric substrate, current density (J_d) is expressed as:

$$J_d = \omega\ \epsilon''E \qquad (2)$$

where ω is angular frequency, and ϵ'' is the imaginary part of the dielectric constant. Therefore, the heat energy per unit volume due to Joule heating can be expressed as:

$$q(\text{density}) = \omega\,\epsilon''\,E^2 = \omega\,\epsilon'\,\tan\delta\,E^2 \qquad (3)$$

where ϵ' is the real part of the dielectric constant, and $\tan\delta$ is the dielectric loss tangent (where $\tan\delta$ is defined as ϵ''/ϵ') [10]. Here, q(density) is the instantaneous value of the heat energy produced per unit volume.

Since $E = E_o \sin\omega t$, the time averaged q(density) can be expressed as:

$$\langle q(\text{density})\rangle = \omega\,\epsilon'\,\tan\delta\,E_o^2/2 \qquad (4)$$

As is evident from equations (3) and (4), the heat energy produced in an electronic substrate can be reduced by reducing ω, ϵ', $\tan\delta$, or E. The values of the frequency and the electric field strength E are set by the electronic

requirements of the particular application. For microwave substrates, E will often be relatively low, but microwave frequencies are on the order of 10^8 to 10^9 Hz, which are relatively high frequencies. Thus, in order to reduce the Joule heating of substrates at microwave frequencies, one can attempt to minimize the material parameters ϵ' and $\tan\delta$. As discussed previously, the dielectric constant ϵ' and loss tangent $\tan\delta$ can be successfully reduced by increasing the specimen porosity.

High bulk porosity leads to undesirable water absorbtion and does not provide for a smooth, nearly defect-free surface suitable for metallization of fine-line circuitry. Water absorbed into the substrate will raise the dielectric constant and consequently the dielectric heating. The dielectric constant of water high. Therefore, the amount of water absorbtion into the substrate must be minimized.

For this project very thin samples (ranging in thickness from 0.3 to 0.9 millimeters) of cordierite electronic substrates were used. A CO_2 laser melted the top and bottom surfaces of the sample, thus sandwiching the original cordierite material between two thin layers of glass-like appearance. During this experimentation, the thickness of the melted glass layers ranged from 20 to 100 microns, depending on the laser processing parameters. In addition, the cordierite substrates were cut using the CO_2 laser, yielding a smooth, crack-free specimen

edge that will likely resist water absorption. The laser cut edges and the laser melted surfaces act to help seal the cordierite specimen against water absorption. Thus, the laser processing will alter, and hopefully improve, the various thermal, mechanical, and electrical properties of the cordierite.

Differential Thermal Analysis (DTA) and cavity perturbation are possible techniques for measuring changes in the thermal and electronic properties of laser-treated ceramics. Infrared spectral absorption techniques [11] can measure the quantity of absorbed water in the cordierite. Also, microindentation techniques [12] can be employed to evaluate quantitatively the mechanical strength and adhesion of the melted surface layer. This study took advantage of x-ray diffraction, scanning electron microscopy, and surface roughness analysis.

1.2 A Review of Laser-Material Interactions

The propagation of a beam of light in a solid is affected in two important ways. First, as the beam penetrates farther into the medium, some decrease in intensity will occur. Secondly, the beam's velocity in the medium will be impeded as compared to its velocity in free space. The loss of intensity is primarily due to absorption, but scattering can also play an important part [13].

Conducting media, or metals, play an important role in optics because their high reflectivity make metallic surfaces excellent mirrors. There is, however, partial penetration of light into the metallic surface which allows one to obtain information about the absorption constants and the mechanism of absorption from observations of the reflected light [14].

Experimentally, reflectance not only depends on the type of metal but also on the preparation of the surface and the direction and wavelength of the incident light. If plane-polarized light is reflects from a metal at other than normal incidence, the incident electric vector is reflected with a phase difference which causes an elliptical polarization. For all metals, plane-polarized light (like that of a laser beam) is not reflected as plane-polarized light except when it vibrates either perpendicular to or within the plane of incidence [13].

When a laser beam is incident upon a metallic surface, traditional optical theory may no longer apply since the incident beam may to alter the material in some way. W. T. Walter has shown [15] that direct real-time measurements of a target material's optical properties can describe surface deformation and plasma formation during laser irradiation. Three physical processes account for the large decrease in reflectance when a laser beam is incident on a metallic surface: (1) the plasma formation (which will be discussed in this section in greater detail) (2) the surface deformation, and (3) a non-linear process which causes an increased absorption in the metal. Specular reflectance can accurately predict the amount and type of surface deformation [15].

When a material is processed with a gaussian laser heat source, the incident radiation is partially absorbed and partially reflected according to the value of surface reflectivity [16]. At any point on the surface, where the temperature is greater than the boiling point, the reflectivity is considered to be zero. This is because a "keyhole", which acts as a black body, has formed [16]. The fraction of the incident beam which falls on a keyhole loses power by reflection and absorption from the plasma generated. A concentric gas jet on the surface enhances conductive heat transfer [16] which is used for sheilding in welding and various surface treatments.

Carbon dioxide and Nd:YAG lasers provide directed energy beams which are far more intense than flames, arcs, or plasma arcs. Compared to electron beams, carbon dioxide lasers are more easily focussed, have a shallower absorption depth, a more controllable distribution of intensity, and no hazard of x-rays. Due to these features, lasers may induce material transformations, including martensite transformation in ferrous alloys. These lasers can also be used for alloying and cladding, encorporation of hard dispersoids, and formation of metastable phases [17]. The high intensity of laser heat sources allows rapid heating and cooling of materials with negligible heating outside the transformed zone. Copley developed a method for determining the thermal diffusivity, the fraction of incident power absorbed, and the volumetric specific heat of a metal [17]. Copley welded a thermo-couple to the surfaces of the materials of interest and used the Rosenthal solution [17], which predicts the temperature distribution for a point source moving in the positive x-direction at a constant velocity.

P. Gay and G. Manassero [18] presented experimental data which supported a two-dimensional mathematical description of the heating process when a metal sample is exposed to laser radiation. Sample heating was described with a finite difference model based on a Fourier heat transfer equation (a numerical representation was not presented). Coatings on the base material increased laser energy utilization, since absorption coefficients of pure

metals are relatively low. At low surface temperatures, the laser-heating process is determined only by the absorption coefficients of the various coatings. Graphite coatings were applied to a 1045 carbon steel base material. At high temperatures, still below the melting point of the surface material, the process is determined by the interaction between the coating and the base material. At the melting point, the heating process is dominated by laser power absorption by the liquid phase (which resembles absorption by the pure metal). Experimental devices and techniques which increase the liquid surface's absorptivity of laser energy would improve laser energy coupling with the material [18].

Thus, laser surface-processing techniques depend on the specimen being heated by the incident beam. Therefore, the temperature distribution at the laser heated melt pool should be known, at least approximately. By directly measuring laser-induced temperatures, predictability and reproducability can be achieved in certain surface-treating processes. R. Jeanloz and D. L. Heinz measured temperatures between 1500^{o}K and 7000^{o}K in Mg-silicate perovskite specimens under continuous wave irradiation from a Nd:YAG laser using a spectroradiometer (at wavelengths of 400 to 850 nanometers). A slit-scanning (tomographic) technique yielded two and three-dimensional temperature distributions [19].

Laser heating produces a temperature distribution in time and space. Let q denote the heat production rate per unit volume per unit time as a function of position and time. The important material parameters for a laser irradiated specimen include K the thermal conductivity, c the specific heat, α the thermal diffusivity, and ρ the mass density. If the laser spot diameter is much greater than the penetration depth of the beam (along the coordinate axis, z), then a one dimensional problem can be considered:

$$\partial^2 T(z,t)/\partial z^2 - (\partial T(z,t)/\partial t)/\alpha = -q(z,t)/K \qquad (5)$$

where:

$$q(z,t) = F(t)(1/\delta)EXP[-z/\delta] \qquad (6)$$

F(t) is I(1-R), where I is the irradiance (power per unit area) and R is the reflectance of the specimen surface. In most metals $(1/\delta)$, where δ is the skin depth, is approximately equal to 10^5 to 10^6 cm^{-1}. The skin depth or "skin effect" is a measure of the depth of penetration of the incident radiation [14]. Substitution of equation (6) into equation (5) and solving the differential equation ultimately yields [20]:

$$T(z,t) = [2F_o(\alpha t)^{1/2}/K]ierfc[z(\alpha t)^{1/2}] \qquad (7)$$

$$\text{and} \quad T(o,t) = (2F_o/K)(\alpha t/\pi)^{1/2} \qquad (8)$$

where ierfc represents the integral of the complimentary error function. Other parameters have the same meaning as in equations (5) and (6). The time-temperature profile at the specimen

surface may be approximated by equation (8).

The absorption and reflectance of a laser beam can be be quite different for metals than it is for ceramics. A laser beam incident upon a ceramic will again alter the material in some way by a number of different phenomena. First of all, there will still be a certain degree of reflection of the beam off of the surface. Conversely, the remainder of the beam will be scattered and absorbed by the material. This interaction will cause a cloud of vapor, or plasma, to be given off. Plasma has been defined as "a gas of free positive and negative charges which is achieved before any absorption of the laser irradiation" [21]. The plasma (electron, ion, and neutral atom) density at the specimen surface is increased by: 1) an increase in surface temperature, 2) photoelectric and thermoelectric phenomena which increase electron density, and 3) a vaporization of surface asperities which will add material atoms, thermal electrons, and ions to the surface region. When plasma generation is desirable, it can be responsible for the bulk of the heat input into the surface. This effect, known as "enhanced coupling", can contribute as much as 50 percent of the incident power density. The plasma absorbs the laser radiation and a pressure wave, called an LSA or Laser Supported Absorption wave propagates along the axis of the laser beam. If the LSA wave velocity is less than or equal to the gas particle velocity, and is subsonic, the LSA wave is said to be a Laser Supported Combustion (LSC) wave. If the LSA wave is supersonic, it

travels at the shock wave velocity and is called a Laser Supported Detonation (LSD) wave. By properly controlling the laser output to achieve a LSC wave near the specimen, high amounts of incident energy can be achieved to process the material's surface [21].

Ultimately, a crater (or melt pool, or weld pool) forms at the beam-material interaction point. Heat then flows into the material, away from the melt pool. These interaction phenomena allow for the use of lasers for various types of ceramic material modifications.

Researchers have observed that periodic surface waves on metals and semiconductors may result from laser irradiation. Hutchinson, Lee, Murphy, Beri, and George [22] studied laser-induced surface ripples using Nd:YAG and Nd:glass lasers at power densities between 10 MW/cm^2 and 1 GW/cm^2. The surface periodicity shows a number of parallel grooves, perpendicular to the electric field of the incident beam which was not observed if the specimens surfaces were randomly scratched before the lasing operation. A secondary ripple pattern, parallel to the incident electric field has been explained in the following way. First, if the plasma frequency of the metal is similar to the frequency of the incident laser beam, then surface plasmons will be excited in the metal. A surface polariton forms when the plasmons (quantized plasma waves) couple with the electromagnetic field. The polariton produces maxima and minima in the

electric field of the surface, which causes surface atoms to rearrange themselves to minimize their energy in the electric field. Another explanation is that the initial surface roughness couples with the incident beam to produce a dipole moment in the surface layer. A field produced by this dipole moment interferes with the refracted beam in the substrate. This interference leads to an inhomogeneous energy absorption thereby redistributing the surface atoms [22]. Maracas, Harris, Lee, and McFarlane [23] consider the periodic surface structure on laser-irradiated GaAs to be a standing wave having a velocity close to that of a longitudinal acoustic phonon of the substrate. Phonons excited by the laser and subsequently "frozen" in place by the cooling of the lattice would constitute the surface ripples [23].

Others have employed experimental procedures and report results similar to those of this thesis [24-26]. G. S. Fischman [24] used a 10 kilowatt continuous wave CO_2 laser to (1) seal zirconia coatings, on stainless steel substrates, from penetration by corrosive agents, and (2) improve the adherence of the zirconia coating to the metal substrate. A time-dependent decay of the coating-substrate adherence depends on the rates at which moisture and other corrosive, deleterious environmental species penetrate the coating. The CO_2 laser, at an output power of 1.5 kilowatts and a beam diameter of 1.0 millimeter produced a power density of 190 KW/cm^2. Helium was used as the shielding gas.

Irradiated surfaces and cross-sections of both the laser-glazed and untreated coatings indicated that the surface treatment was very effective. By varying the laser processing parameters, markedly different effects could be achieved. Lower output power and higher table speeds melted the coating without changing the coating-substrate interface. Conversly, higher output power and lower table speeds fused the entire coating to the metal substrate, improving the integrity of the ceramic-metal contact (as compared to the initial as-sprayed surface). Extensive cracking of the zirconia coatings often occurred [24,25], and was typically described as an "important problem to be dealt with". No solutions of the cracking problem were discussed [24,25].

Micrographs of the plasma-sprayed zirconia coatings showed that porosity was markedly reduced by the laser surface melting [24], although extensive cracking was observed. Remedies for the cracking problem may include an improved design of the plasma spraying system, which may minimize shrinkage and cracking during the laser glazing operation. Also, further optimization of laser surface melting parameters is being explored [24,25].

Laser surface processing of plasma-sprayed Stellite coatings produced microstructural changes which resulted in improved wear and corrosion resistance [26]. An AVCO HPL 10 kW continuous wave CO_2 laser was used for the surface treatment. Capp et. al. designed and built a processing system named

LAMP (laser-assisted materials processor) to be used for the surface treatment. Important laser parameters, such as table speed, working distance, and laser output power were not discussed by Capp and Rigsbee [26]. Initially, the plasma-sprayed coatings were quite porous, which in turn degraded the wear and corrosion properties of the Stellite coating material. Microstructural studies of the coating after the laser surface treatment showed an enhancement of coating strength, elimination of porosity, and a better bonding at the coating-substrate interface [26]. No mention was made as to whether or not cracking was induced during the laser treatment. Microstructural and microchemical examination of the laser-fused coating before and after laser processing showed an enhancement of coating chemical homogeniety and strength. According to Capp and Rigsbee [26], this would improve the performance of the coating where interfacial stresses would be produced by thermal cycling. The elimination of porosity would enhance service life where a harsh corrosion environment exists [26].

2. EXPERIMENTAL PROCEDURE

2.1 EXPERIMENTAL APPARATUS

2.1.1 Carbon Dioxide Laser

Cordierite substrates can be fabricated in a "sandwich" configuration as shown in figure 1a by using a 2 kilowatt carbon dioxide laser. Figure 1b depicts the experimental procedure with which these "sandwich" specimens will be fabricated. This figure shows that the specimen is translated under a stationary laser beam.

The CO_2 laser head assembly is depicted in figure 2. The laser head comprises an H-section beam which has mounted on it an optical system and four horizontal glass discharge tubes. The H-beam is supported on a floor mounted steel frame. Contained in the main frame are a gas blower, a vacuum pump, and a heat exchanger unit (see figure 3). The output of the laser is switched by a shutter mirror which can be moved in and out of the laser output path. When the shutter mirror is moved into the path of the laser, the beam is directed into the calorimeter, which is used as a power dump (to be discussed further). With the shutter mirror clear of the laser beam, the power output is able to pass out of the laser head and into an external workhandling system [27]. See figure 4a for an overhead view of the laser path.

The power density of the beam is measured using a

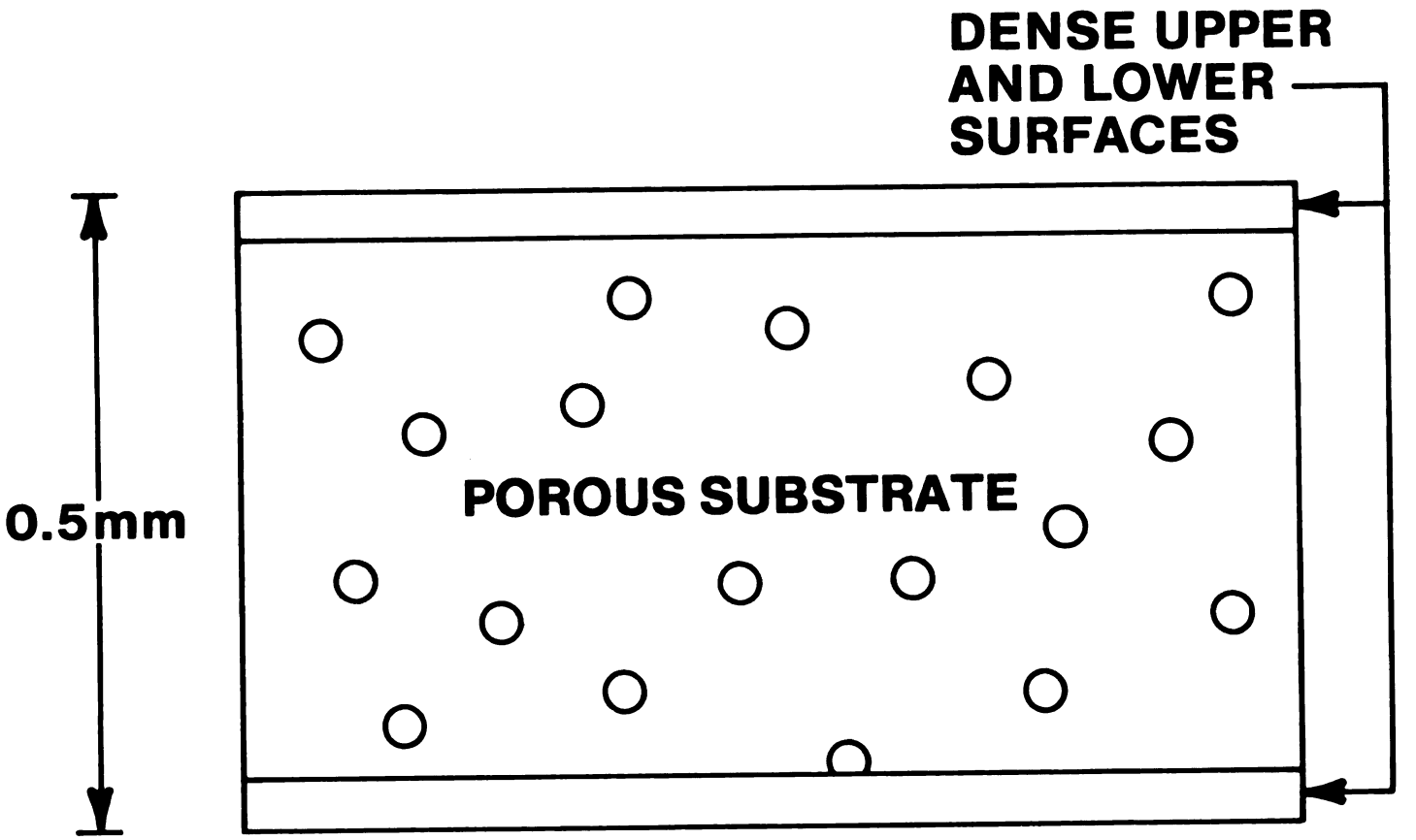

Figure 1a. Cross-section of cordierite substrate. This figure illustrates the "sandwich" specimen.

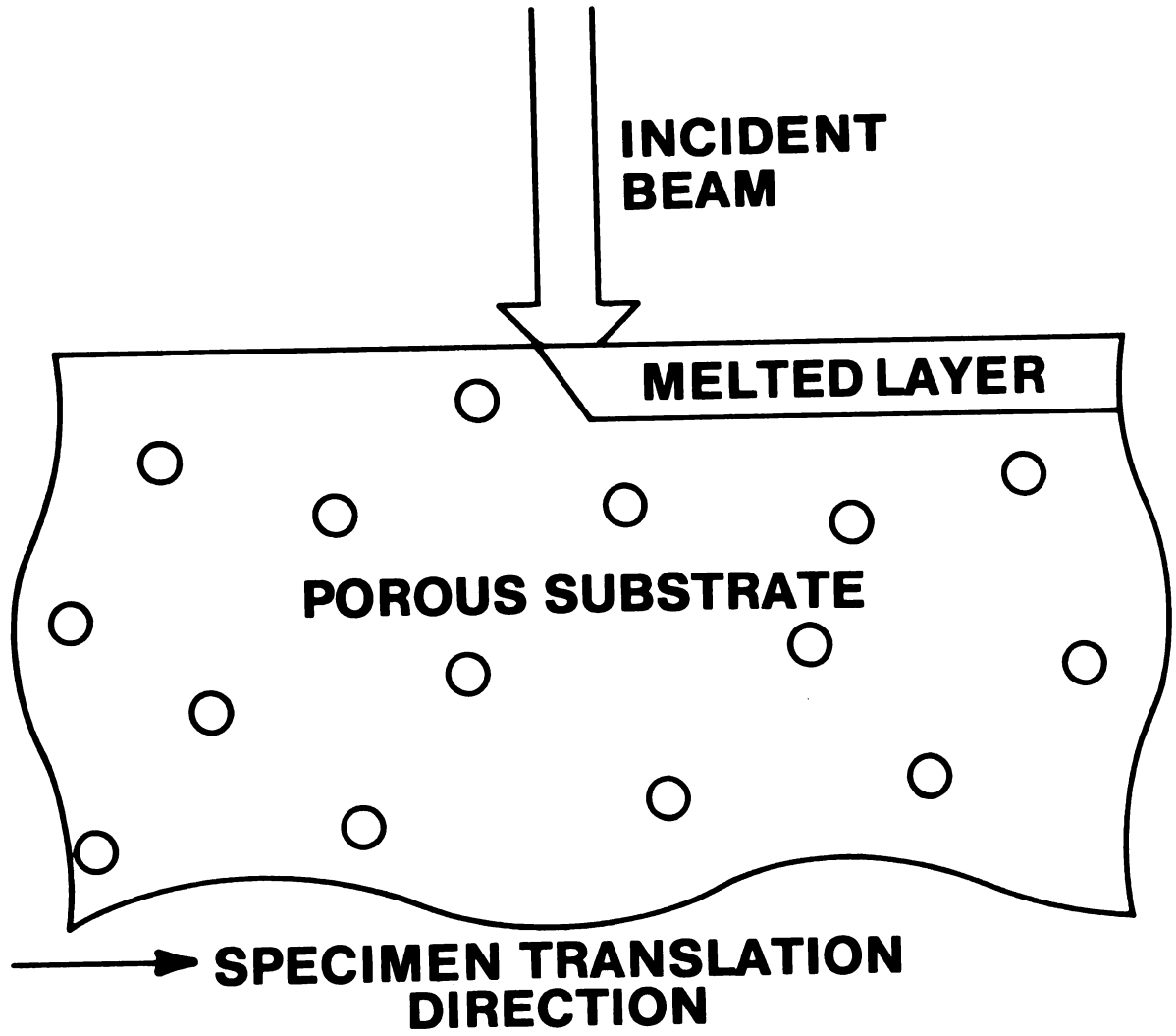

Figure 1b. Experimental procedure with which surface-treated specimens are fabricated. The specimen is shown translating under a stationary beam.

calorimeter made by the British Oxygen Company. When the CO_2 laser beam exits the charging tubes, gold-plated mirrors reflect the beam into the calorimeter. The calorimeter is eight inches long with a 2 inch diameter opening. It consists of a pure copper cone surrounded by a plastic water jacket. In this jacket, water flows around eight evenly-spaced thermocouples. Four of these thermocouples measure the temperature of the incoming water and the other four measure the temperature of the outgoing water. The temperature of the outgoing water is greater than that of the incoming water because the water is heated by the energy of the incident laser beam. The difference in temperature between the incoming water and the outgoing water creates an electro-motive force which is calibrated in terms of watts. The inner core of the copper cone is black in color to assure maximum absorbtion of the energy of the beam.

The distance between the specimen and the focal plane was measured using a helium-neon laser beam directed through the outer reflection mirrors of the CO_2 laser. The helium-neon laser produces a visible red beam which makes it possible to easily locate the focal plane. The procedure for determining the focal plane is as follows: the specimen is placed on the X-Y table in the path of the beam. The vertical height of the sample is then adjusted so that the dot produced by the beam is as sharply defined (focused) as possible--this is the focal plane of the beam. Distances from the focal plane are

measured by hand using a metric ruler. Vertical motion of the X-Y table can be controlled manually by raising and lowering the support apparatus and tightening the set screw by hand (see figure 2). A small mark made on this vertical adjustment, at the focal plane, serves as a reference when making measurments of the vertical distance from the focal plane. A beam focussing chart indicates the laser beam diameter at various distances from the focal plane (figure 4b). Knowledge of the beam diameter is essential for power density calculations. Our CO_2 laser uses a 5 inch focal length lens.

2.1.2 X-Y Tables

Two different X-Y tables were used during the course of this work. The first table, built by Narendra Dahotre, then a graduate student at Michigan State University, was a variable speed table which used a control circuit external to the laser circuitry. A speed of 45 cm./min. controlled horizontal movement of the specimen during laser treatment. This was the table's maximum cross speed (minimum speed was 4 centimeters per minute). The table speeds were calibrated by attaching a pointer to the rods which move under the table. Table speed was measured by observing the distance travelled by the pointer along the linear scale (attached beneath the table) in a known interval of time. By adjusting the variables of table speed, laser output power, and distance from the focal plane, the surface of the

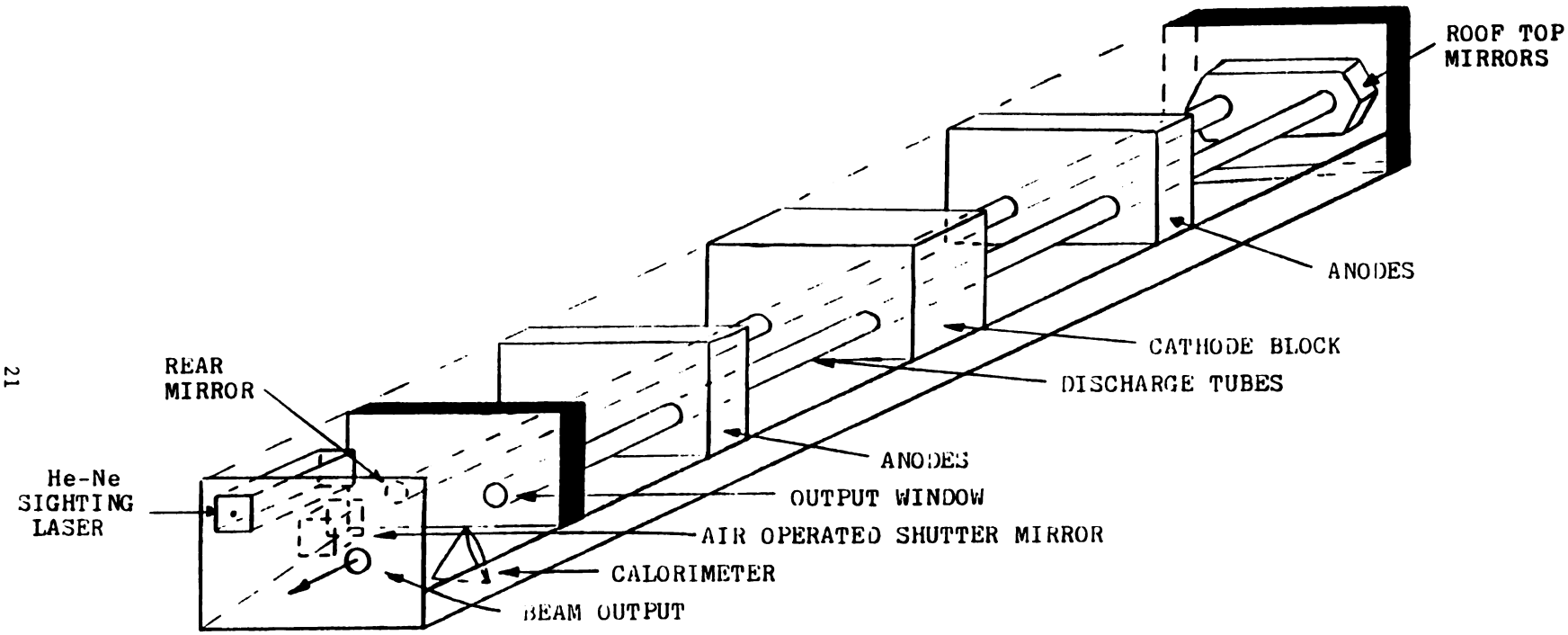

Figure 2. General view of CO_2 laser head.

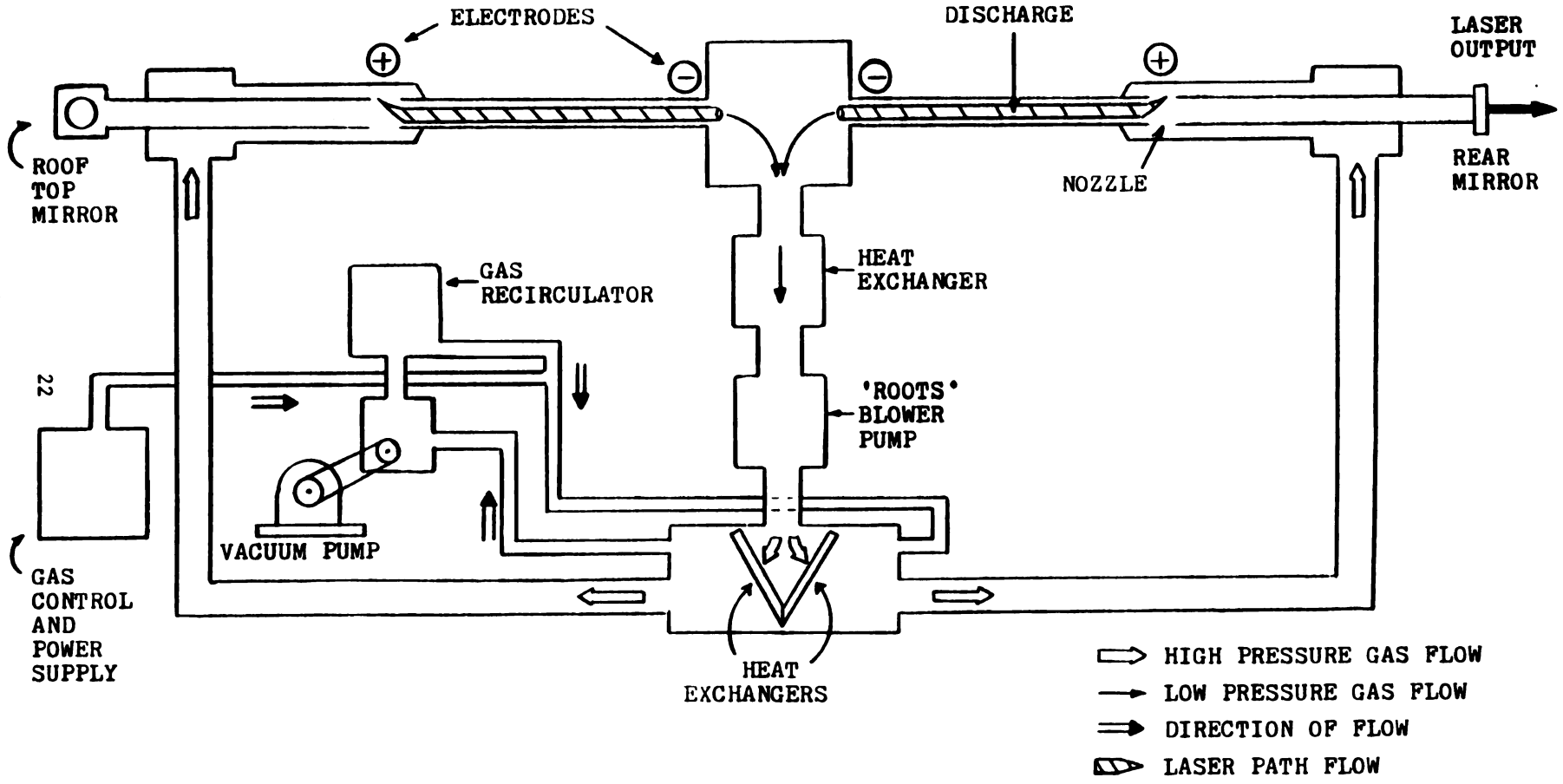

Figure 3. Gas and discharge paths of the CO_2 laser.

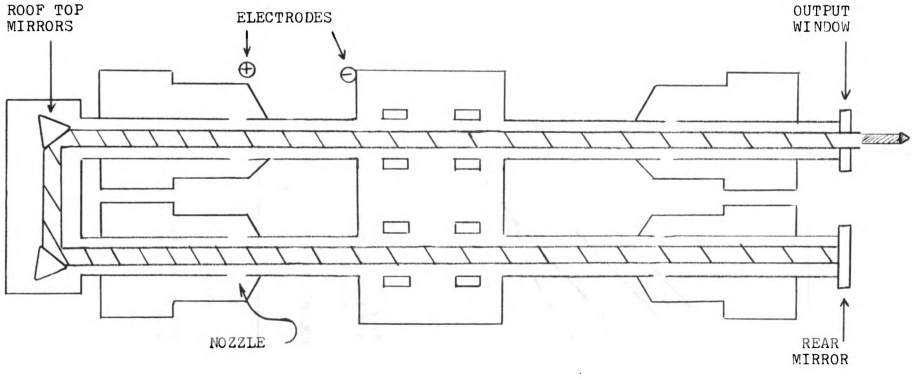

Figure 4a. Overhead view of CO_2 laser path.

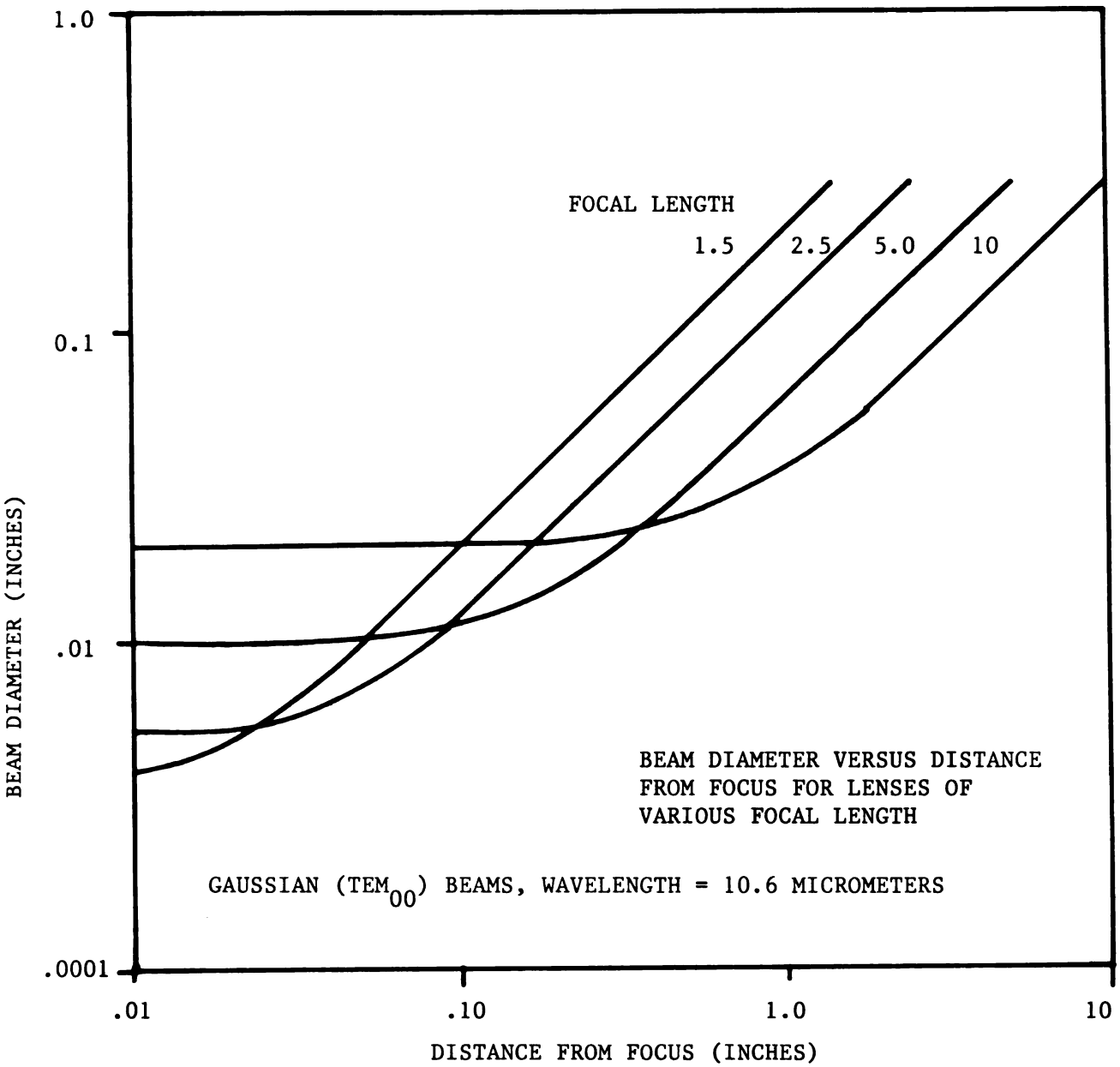

Figure 4b. Beam focussing chart which allows for the determination of laser beam spot size at various points in the path of the laser beam. [28]

cordierite was melted without cutting the sample.

The second X-Y table (currently in use) is a CNC table made by Laser Machining, Inc., of Somerset Wisconsin. It has a minimum crosshead speed of 0.1 inches per minute and a maximum speed of 600 in./min. (for a straight cut operation). For edge cutting (turning corners) the maximum speed is 300 in./min. After the upgrading of the X-Y table, it became possible to carry out surface processing experiments much more efficiently. The new table was much more versatile, with a greater range of available speeds. It was now possible to vary all three of the important processing parameters (working distance, output power, and table speed).

The original cordierite specimens were placed on two specimen setters made of 1018 plain carbon steel. Each setter had a width of 0.188 inches, a height of 0.125 inches, and a length of one inch. The purpose of the setters was to prevent fusion of the workpiece to the X-Y table during laser treatment by raising the specimen off the table.

The specimen setter used with the new X-Y table was again a plain carbon steel plate. This setter had a width of 5 inches, a height of one eighth of an inch, and a length of 9 inches.

The specimens, as they were recieved, had the dimensions of 60mm by 60mm by 0.5mm. These substrates were broken up by hand into pieces approximately 10mm by 20mm. The first few attempts made to melt the surface of the cordierite resulted

in cutting of the samples. Cutting occurred at beam powers of greater than 600 watts, at a distance of approximately 10 millimeters from the focal point of the beam. In an attempt to melt surface of one of these pieces without cutting it, the sample was lowered to a position one hundred millimeters from the focal plane of the beam. This greatly decreased the power density of the beam and, at the same time, increased the beam diameter by 0.29 inches.

2.1.3 Nd:YAG Laser

It should be mentioned at this point that a pulsed Nd:YAG laser (1.06 microns wavelength) was also used to surface-treat the specimens. The pulsing effect of the Nd:YAG laser made it impossible to achieve a smooth edge cut. When the edge cutting was attempted, a stirated or jagged cut was made which all but destroyed the specimen.

The YAG laser, however, was moderately successful in surface-melting the substrates. As it will later be seen, the YAG laser produced varying degrees of surface melting. Also, the surface texture seemed to vary from melt to melt.

2.2 LASER SURFACE MELTING AND CUTTING OF THE CORDIERITE SPECIMENS

For the initial surface melting experiments, the output power of the CO_2 laser was lowered to 550 watts. This is the lowest attainable power output of the 2 kilowatt CO_2

laser. At a power of less than 550 watts, charging voltage is lost in current tube number 3 which, in turn, cuts off output of the beam. This CO_2 laser is rated at a maximum power output of 2 kilowatts. Although the laser is actually capable of producing powers of up to 2400 watts, 2000 watts is the highest power at which the laser can be operated safely.

Specimens were prepared by using the laser to cut out samples approximately $1cm^2$. The cutting energy of the beam was 800 watts and the focal point of the beam was used to make the cuts. The surfaces of the samples were then melted using the same parameters described previously (550 watts laser output power, 45 cm./min. X-Y table speed, and a 3 millimeter spot size resulting from a 100 millimeter working distance from the focal plane of the beam). This produced a power density for the CO_2 laser of 7.5×10^6 J/m^2sec.

The surface melting using the Nd:YAG laser occurred at output powers ranging from 35 watts to 80 watts, 48 cm/min table speed, and a 110 mm working distance from the focal plane of the beam producing a spot size of 2 millimeters. Optimal surface melting (without cracks) occurred at an output power of 45 watts, a table speed of 48 cm/min, and a working distance of 110 mm. This produced a power density of 1.88×10^6 J/m^2sec.

As was previously mentioned, the arrival of the new X-Y table allowed a wider range of table speeds to be used. It was now possible to decrease processing power densities by increasing the X-Y table speed. In addition, the table

could be programmed to move in an arbitrary pattern in the x-y plane (normal to the incident laser beam).

The most commonly used program for X-Y table movement was a back-and-forth pattern which caused the laser beam to scan the entire area of interest. Upon the completion of one pass, the table was programmed to translate over 6 millimeters, and then make another pass. After the completion of this pass, the table would translate over another 6 millimeters and then make another pass. This program would proceed until the entire surface of the substrate was melted. Initially, the X-Y table was not programmed due to a shortage of available specimens since one or two passes was all that could be accomodated on a relatively small specimen (approximately 1x2 cm). If after one pass, another pass was needed, the specimen was translated manually by approximately 3 millimeters. Another pass would then be made, and so on, until the processing was complete.

More cordierite specimens were received later and it was possible to take advantage of the scanning ability of the new X-Y table. An entire as-recieved specimen (60mm x 60mm x 0.9mm) could be placed on the table and be entirely surface-processed in a one-step operation. The laser scanned the entire length of the specimen, translated over one centimeter, and scanned back across the length of the specimen. This proceeded until the operation was complete.

Although cracking was evident during the operation, samples large enough for x-ray diffraction analysis could be fabricated.

To produce the thinnest, crack-free melted layer possible, the power densities had to be lower than 7.5×10^6 J/m^2-sec. What was not so obvious was how they were to be lowered. The possibilities were: 1) lower the output power 2) defocuss the beam further, or 3) increase the table speed. Lowering the output power any further was not possible because charging would be lost in tube 3 (previously explained).

A multitude of variations in the second and third criteria were explored. Table speeds ranging from 30 to 120 in/min were combined with output powers ranging from 650 to 1000 watts and working distances ranging from 50 to 140 mm. The results of various combinations of parameters always produced one of the following outcomes: 1) no melting 2) a slight degree of melting with cracks 3) a slight degree of melting without cracks, or 4) complete melting (destruction of the specimen). The third of these possible outcomes was the goal and was ultimately achieved with the following parameters: 700 watts output power, 80 in/min X-Y table speed, and 5.5 inches working distance. This produced a power density of 2.31×10^6 J/m^2sec. These parameters were also adequate to fabricate crack-free "sandwich" specimens. Table B1 lists power densities and the corresponding results.

2.3 SCANNING ELECTRON MICROSCOPY OF UNTREATED AND LASER TREATED SPECIMEN SURFACES

The microstructure of untreated and laser-treated cordierite specimens were studied using a Hitachi S-415A scanning electron microscope and a JEOL JSM-35C scanning electron microscope (see appendix A for specimen dimensions). To allow the use of an SEM, the ceramic material must be coated with a metallic layer in order to permit electrical conductivity on the surface. This metallic layer was produced on the samples using a Polaron E5175 SEM sputter coater. During sputter coating, the specimens were placed in the coating chamber and the chamber was evacuated and back-filled with argon gas. The working voltage and current were 2.5 kilovolts and 25 milliamperes, respectively. The distance from the target to the specimen was 5 centimeters. The coating was then done for one minute. Experiments using interferometric techniques have shown that the thickness of a gold coating sputtered in argon gas can be calculated at 2.5 kV according to [29] :

$$th = 7.5*I*t \quad \text{(in angstroms)} \tag{9}$$

Where th = thickness of sputtered coating (in angstroms), I = working current (in milliamperes), and t = time (in minutes). Therefore, given the operating conditions used in this work, equation (9) yielded the estimate that 187.5 angstroms of pure gold had been deposited on the surface of

the specimen.

For SEM examination, the cordierite specimens were mounted on stubs prepared from cylindrical aluminum blanks. Stubs 12mm in diameter and 6mm in length were cut from blanks using a band saw. The circular faces of the stubs were then sanded using a belt sander and roughly polished using sandpaper strips. A flat mounting surface is important, as it promotes better adherance of the specimens to the stubs.

The cordierite specimens were mounted onto the aluminum stubs using Duco cement. After the glue had dried thoroughly (for approximately two hours) GC Electronics silver paint was applied to the mounted samples and stubs with a toothpick in air at room temperature. A thin strip of the silver paint (approximately 1mm wide) was applied from the center of the mounting stub, up to the edge of the specimen, and ended at the top surface of the sample. This conductive paint permitted the flow of incident electrons from the gold-coated surface of the sample to the metallic stub. This particular pattern of application allowed for an even, continuous electron flow without defacing the specimen surface. After application of the paint was complete, the samples were dried overnight in a covered plastic specimen container. SEM examination was normally carried out the next day.

2.4 SURFACE PROFILOMETRY OF UNTREATED AND LASER TREATED SURFACES

Surface roughness measurements were obtained on the untreated and laser treated specimen surfaces by a Sloan Technology Corporation Dektak IIA profilometer. The Dektak IIA is microprocessor-based and is capable of making accurate measurements on changes in vertical features on various surfaces. During operation, the specimen is translated beneath a diamond-tipped stylus which has a standard radius of 12.5 microns.

During operation, differences in topographical features cause the stylus to translate up or down according to the surface topography. The vertical movements of the stylus (analog) are digitized by the Dektak using an integrated A-D converter. The instrument then stores the data and displays it on a video screen. At this point, various measurements and calculations can be made. Also, hard copies or print-outs can be made.

Options available to the user include an identification number for experimental runs and a scan length from 50 microns to 30 millimeters. Three different scanning speeds are available (low, medium, and high). The medium speed is usually used which combines good horizontal resolution with reasonably fast processing time. Two different options for the range are available--AUTO range and Pre-Set. In AUTO

range mode, the computer chooses the specific range that modifies the profile so that 80 percent of the screen is filled. In Pre-Set mode, the user can choose any range from 200 to 655,000 angstroms.

Three different profiles are available--peaks, valleys, or peaks and valleys combined. If the peaks option is chosen, the computer zeros the line at 10 percent of full scale (making the screen range from -65,000 to 599,000 angstroms). The valleys option will do just the opposite. If peaks and valleys is chosen, the screen scale splits, making the range of vertical inflection the same above and below the zero axis.

R and M (Reference and Measurement respectively) cursors delimit desired areas in the profilometer trace for various calculations. Directional keys on the keyboard position these cursors. The most important parameter that can be calculated (for this work) between the R and M cursors is the Arithmetic Roughness Average (RA). The roughness average is computed by determining a mean straight line through the profilometer trace. The computer then calculates the average deviation from the mean line and displays it in the lower right hand corner of the cathode ray tube (and subsequently, the print-out). The following section compares the roughness averages for various as-recieved and laser-treated specimen surfaces. See appendix C for a more complete set of the Dektak IIA specifications.

2.5 X-Ray Diffraction/Surface Characterization

X-ray diffraction experiments on the untreated and laser treated specimen surfaces were performed on a General Electric diffractometer (copper radiation, nickel filter). The chart recorder was a Speedomax made by the Leeds & Northrup Company.

The difractometer measures the intensity and angular distribution of x-rays of known wavelength diffracted by crystalline and non-crystalline materials. A diffracted beam is composed of a large number of scattered rays constructively reinforcing one another. Therefore all rays, in phase, scattered by a particular crystal will contribute to the diffracted beam.

During operation, an electronic "counter" directly measures the intensity of the diffracted beams. These counters convert the incoming x-rays into surges of electric current in the counter circuit. The counter registers the number of current pulses per unit time, which is directly proportional to the x-ray intensity [30].

For these experiments, the initial 2θ angle was 5 degrees, with a maximum 2θ that ranged from 70^{o} to 90^{o}. The range varied from 1000 to 2000 cps. The x-ray tube current and voltage were 115 milliamps and 33 kilovolts respectively. A time constant of 1 was used for the counter.

During operation, the entire applicable range of 2θ values is scanned by the counter, at a constant angular velocity through increasing values of 2 theta. The strip-chart recorder simultaneously moves at a constant speed, incrementally proportional to 2 theta. The resulting charts are presented and analyzed in the Results and Discussion section. These charts give the diffracted intensity versus diffraction angle (2 theta).

Due to their small size and fragility, the cordierite specimens were attached to glass slides by Duco cement. The glass slides provided the necessary mechanical support during the x-ray diffraction experiments. After completing the diffraction experiments on a given specimen, and prior to beginning annealing experiments, the specimens were removed from the glass slides by heating in an electrical resistance furnace, in air, at 340^{o}C for two and a half hours.

Annealing experiments were conducted in a General Signal Lindberg furnace at temperatures between 700 and 900 degrees Celsius. The laser-treated cordierite specimens were then placed on spinel blocks for the furnace treatment. Thermal shock damage was prevented by furnace-cooling the specimens through a 24 hour period. After the normal two hour anneal, the temperature in the furnace was lowered 200^{o}C every hour until 100^{o}C was reached. The furnace was then turned off and the specimens allowed to cool overnight.

The cordierite specimens were then re-attached to a glass microscope slide for further x-ray diffraction analysis.

3. RESULTS AND DISCUSSION

3.1 Scanning Electron Micrographs of Treated and Untreated Specimens

SEM Micrographs for the treated and untreated cordierite surfaces are presented in figures 5 through 29. Figures 5 through 10 are micrographs of the untreated cordierite (specimen numbers C1-C3). Figures 11 through 29 are micrographs of the treated specimens (specimen numbers C4-C13).

3.1.1 Untreated Cordierite Microstructure

The white lettering and numbering at the bottom these micrographs indicates the following: The first number (15 KV) shows that the micrograph was taken at an electron accelerating voltage of 15 kilovolts. The second number (X100) indicates one hundred times magnification. The third number (0002) shows that the micrograph was the second one taken during that particular session. The fourth number indicates the size scale for that particular micrograph. In this example, 100.0U means that the length of the white line above it represents one hundred microns of length in the micrograph. The lettering shown in the lower right corner (CEO 87) stands for "Center for Electron Optics", 1987.

Figure 5 is a low magnification micrograph of the corner of untreated cordierite specimen C1. Even at this low magnification (100 times) porosity is evident in the specimen.

The lower right hand quadrant shows the surface of the cordierite. The cloudy white appearance of this region indicates a large amount of porosity. The black arrow in the center of the figure points to the edge of the surface where a "chip" has broken off. The removal of this chip exposed the interior of untreated cordierite for closer examination.

Figure 6 is a higher magnification micrograph (430 times) of the interior region of cordierite specimen C1 pointed out in figure 5. The upper left hand portion of the figure has a cloudy white appearance indicative of a large amount of interior porosity. The edge boundary evident in figure 5 appears in the lower left quadrant of figure 6. This boundary separates the the interior view from the darker surface region.

Figure 7 is a higher magnification (600 times) view of the edge of untreated specimen C2. The arrow in the center of the micrograph points out the center of the edge of the specimen. This gray colored region shows a more exaggerated view of the edge porosity. The right portion of the figure is a dark colored region showing the surface of the sample (this region is out of focus due to the limited "depth of field" of the electron microscope).

Figure 8 is more or less the reverse image of figure 7. The white region on the left side of specimen C2 is the edge described in figure 7 and is out of focus due to the limited depth of field. The black arrow in micrograph 8 lies in a cloudy white region which is the edge of the

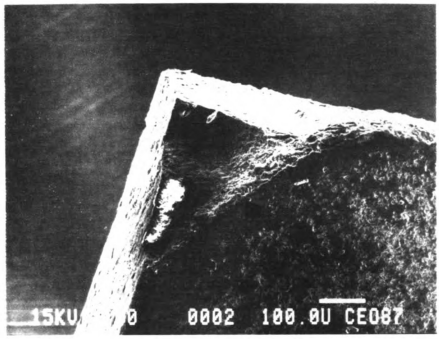

Figure 5. Corner of untreated cordierite specimen C1.

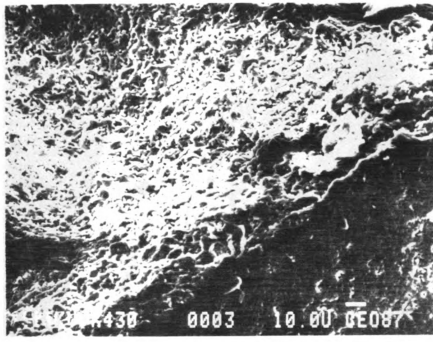

Figure 6. Corner of untreated cordierite specimen C1 at higher magnification.

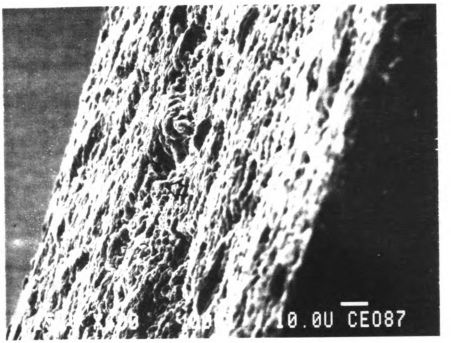

Figure 7. View of edge of unfractured, untreated cordierite specimen C2.

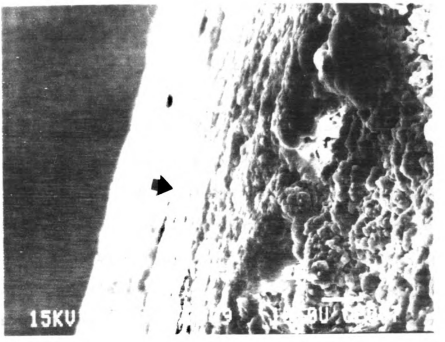

Figure 8. View of surface of unfractured, untreated cordierite specimen C2.

specimen. The arrow is pointing to the surface of the specimen. At 900 times magnification, surface porosity is still more evident.

Figure 9 is a high magnification micrograph (2000 times) of the surface of untreated cordierite specimen C3. Pore sizes range from approximately one to eight microns. The black arrow in the center of the micrograph points to the pore shown at very high magnification (15000 times) in figure 10. This pore is approximately six microns long and three microns wide.

3.1.2 Microstructure of CO_2 Laser-Treated Specimens, Where Laser Treatment was Performed on X-Y Table With a Maximum Translational Speed of 45 cm/min.

Figures 11 through 15 are scanning electron micrographs of laser treated cordierite specimens C4 and C5. In particular, figures 11 and 12 illustrate the graduation of surface melting which has occurred for specimen C4. The upper right-hand corner of figure 11 shows a section of the untreated cordierite, which appears as a rectangularly shaped, cloudy white region indicative of a large amount of porosity. The area surrounding the untreated region is a "transition zone" that has been slightly laser treated (by the outskirts of the gaussian intensity profile of the laser beam). The transition zone is less porous than the untreated region. Pores in this transition zone appear spheroidal, consisting of a dark inner core surrounded by a light colored border. The pores in the

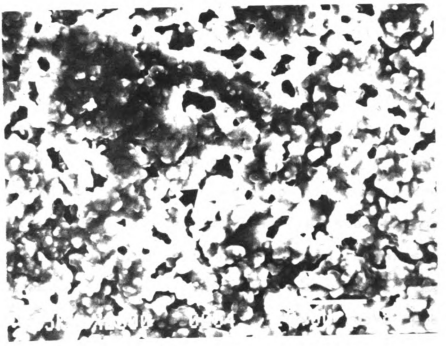

Figure 9. Untreated cordierite specimen (C3) surface.

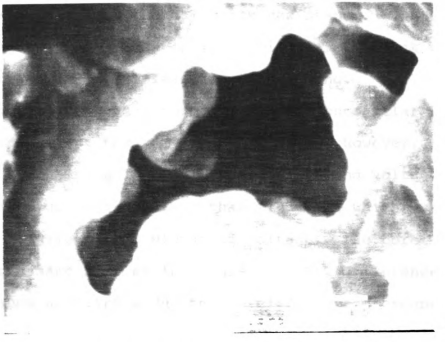

Figure 10. Enlarged view of the surface pore indicated by the black arrow near the center of figure 9.

transition zone are on average about 0.007 millimeters in diameter (approximately 15 pores extend along the length of the size scale which is 0.1 millimeters in length). Further away from the porous region (toward the lower left-hand corner) the porosity decreases further. The porosity thus decreases as we approach the areas of the sample treated by the highest laser beam intensities (that is, near the geometric center of the beam). The lower left-hand corner shows some cracking which has taken place during the laser treatment of this particular specimen (C4). These cracks appear as an interconnected network of hair-like white lines of lengths varying from 50 microns to 100 microns. No through-plate cracks or fractures entirely through the specimen were ever observed. However, as was previously mentioned, cordierite has good thermal shock resistance. The as-recieved specimens were only 0.4 millimeters thick which also acted to prevent large-scale cracking.

Figure 12 shows a porosity graduation similar to that in figure 11 for the same specimen (C4). However, micrograph 12 was taken using 15 kilovolts accelerating voltage and shows much greater contrast than figure 11 which was taken with a 25 kilovolt accelerating voltage. The pores appear to be the same size as in figure 11. Any differences in appearance are likely due to the electron microscope settings. Since a greater contrast was used while taking the micrograph, the cloudy white porous region appears to be much brighter. No cracking is evident in figure 12.

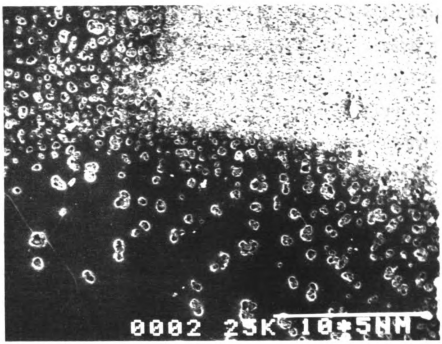

Figure 11. Graduation of porosity in laser-treated cordierite specimen C4.

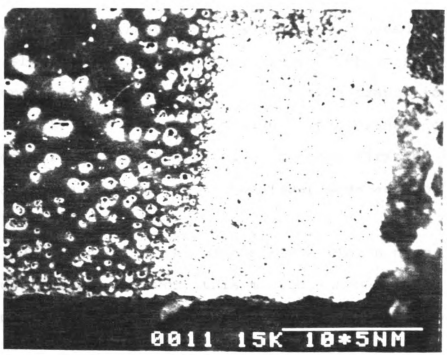

Figure 12. Graduation of porosity in laser-treated cordierite specimen C4.

Figure 13 includes a laser-induced crack in the center of the micrograph, on the left-hand side. This crack appears as a wavy, light-colored line approximately 0.025 millimeters wide. The segment of the crack included in figure 13 is approximately 0.9 millimeters in length. This micrograph was taken at 25 kilovolts and shows a small amount of porosity. Five spheroidal pores which vary from approximately 0.01 millimeters to 0.025 millimeters in diameter are evident in figure 13.

Figures 14 and 15 illustrate the cut specimen C5. Both micrographs were taken using 5 kilovolts. Figure 14 is at higher magnification with a scale line length of 0.06 millimeters. The lower left portion of the figure shows the laser-cut edge. This "glassy" appearing melted region, approximately 0.06 millimeters wide, contains neither cracks nor pores. The upper right-hand corner of the micrograph illustrates the untreated porous region discussed previously. Midway between the glassy edge-cut region and the untreated porous region exists another transition zone approximately 0.05 millimeters wide. This transition zone has been slightly laser treated by the outskirts of the gaussian intensity profile of the laser beam and contains a small amount of porosity.

Figure 15 depicts the same surface finish seen in the previous figure. However, this micrograph was taken at a lower magnification (scale line length is 0.1 millimeters).

Figure 13. Laser-induced crack (cordierite specimen C4).

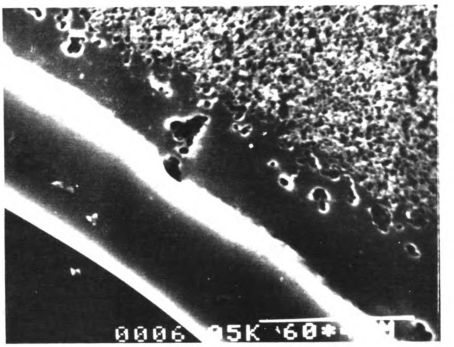

Figure 14. Laser edge-cut (cordierite specimen C5).

FIGURE 15. Laser edge-cut (cordierite specimen C5).

3.1.3 Microstructure of Nd:YAG Laser-Treated Specimens

Figures 16 through 18 are micrographs of the Nd:YAG surface-melted specimens. Figure 16 shows a very irregular melt region, indicating a spuratic and random melting behavior. Several spheroidal pores in the melted region range in size from 10 to 100 microns. Also visible is a network of cracks that terminate at these pores. The cracks range from 100 to 500 microns in length.

The interface between the melted and unmelted regions for Nd:YAG processed specimen C7 (75 watts of output power) is abrupt with no distinct transition zone (figure 17). Also, a rather large crack appears in the upper left-hand corner.

Optimal surface melting, using the YAG laser, occurred at an output power of 45 watts. The glassy, melted region shows a cobblestone-like texture (figure 18). Also, no cracking is evident and a transition zone does exist. This power density of 1.88 X 10^6 J/m^2-sec seemed to exhibit the best melting behavior.

3.1.4 Microstructure of CO_2 Laser Surface-Melted Specimens, where Laser Treatment was Performed on X-Y Table with a Maximum Translational Speed of 600 in/min.

Figures 19 through 30 are micrographs taken of surface-treated specimens using the CO_2 laser and the Laser Machining

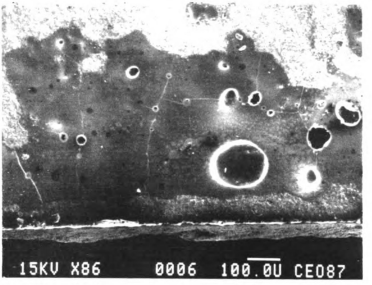

Figure 16. Nd:YAG laser-treated surface, indicating a spuratic, irregular melting behavior (cordierite specimen C6).

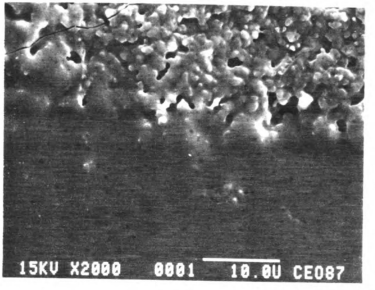

Figure 17. Nd:YAG laser-treated surface. No distinct transition zone is evident (cordierite specimen C7).

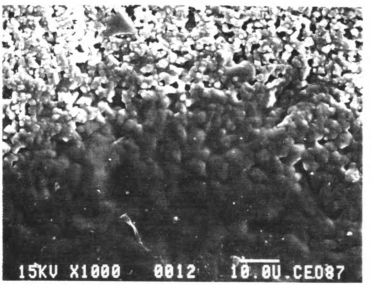

Figure 18. Nd:YAG laser-treated surface. The melted region appears to have a cobblestone-like texture (cordierite specimen C8).

Co. X-Y table. Figure 19 shows an unbroken edge of a laser-treated sample. The melted layer , which traverses diagonally in the lower right hand corner of the micrograph, is approximately 100 microns wide (over one quarter of the total thickness of the substrate). Although no cracking is evident, the melted layer is much too thick and would increase the dielectric constant by reducing the porosity (an increase in porosity decreases the dielectric constant). At this point, it was obvious that further optimization of processing parameters was needed.

Specimen C9 was fractured in bend, along a plane oriented normal to the melted surface in order to measure the thickness of the melted layer along a cross-section of the specimen. This melted layer which is about 100 microns thick (figure 20) contains a few widely dispersed pores with a diameter of approximately 5 microns. The melted layer seems to adhere well to the porous substrate and no cracks are apparent. The thickness of the melted layer was uniform along the entire fracture surface. The only problem was that the layer was too thick.

The laser processing parameters were adjusted and a preliminary result can be seen in figure 21. This edge-mounted unbroken surface of specimen C10 showed a large amount of sub-surface cracking. An immense network of cracks visible by the unaided eye ran along the surface of the treated specimen. The particular crack shown in this figure (21) ran along the entire length of the edge-mounted specimen. The positive result here was that the melted layer was now only

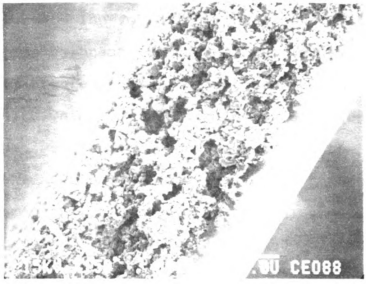

Figure 19. Unbroken edge of a CO_2 laser-treated specimen. The melted layer is over 100 microns thick (cordierite specimen C9).

Figure 20. Fracture surface of an edge-mounted, laser-treated specimen. The melted layer is still over 100 microns thick (cordierite specimen C9).

20 microns wide and was quite uniform.

Further variations in the processing parameters were then explored. The following micrographs (figures 22 through 26) show the thinnest, crack-free melted layer that was obtained. Figure 22 depicts an edge-mounted, unbroken surface melted layer which varied from 10 to 20 microns along the entire specimen length. Good adhesion to the porous inner-bulk of the substrate of obvious, as is the absence of any type of cracking. It should be emphasized at this point that this melted layer geometry was the ultimate goal of my processing efforts (see table B1 for the optimal processing parameters). The following five micrographs examine this layer in greater detail.

Edge-mounted specimen C11 (figure 22) was fractured in bend, exposing a melted layer of uniform thickness (figures 23 and 24). The thin layer adhered well, without cracking (figure 23).

A higher magnification (2000 X, figure 24) allows a clearer view of the melt zone and the interface for specimen C11. Only one sub-micron pore can be seen in the melt zone (half way down on the right side of the micrograph).

In a better overall view of the fracture surface (figure 25), the melted layer appears as a white band approximately 20 microns wide running vertically along the right side of specimen C11. This micrograph gives an important comparison of the thickness of the melted layer with

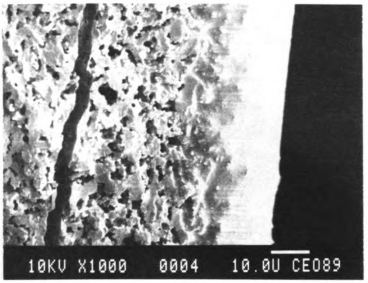

Figure 21. Edge-mounted, unbroken laser-treated cordierite specimen C10. A large crack traversed the entire length of the specimen.

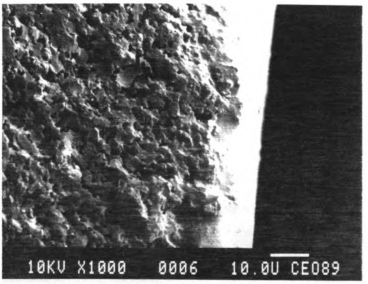

Figure 22. Edge-mounted, unbroken laser-treated cordierite specimen C11. Note thickness of melted layer and absence of cracks.

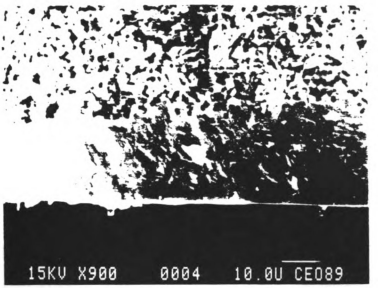

Figure 23. Edge-mounted cordierite specimen C11 fractured in bend, shows melted layer is of uniform thickness.

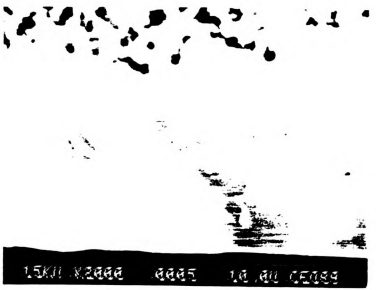

Figure 24. A higher magnification micrograph of edge-mounted cordierite specimen C11 fractured in bend. Allows a more careful inspection of the surface.

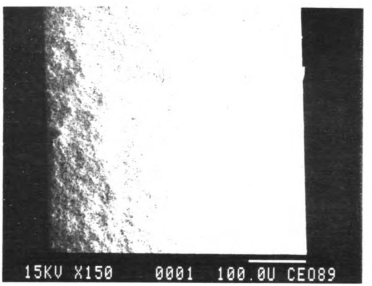

Figure 25. Overall view of the edge-mounted cordierite fracture specimen C11. Note absence of cracks and thickness of melted layer.

the entire thickness of the substrate. The melted layer now comprises less than one tenth of the entire thickness of the treated substrate. A layer this thin would likely only slightly affect the dielectric properties of the substrate. In addition, the absence of cracks indicates that the mechanical properties should not be affected adversely.

Figure 26 illustrates the graduation in surface porosity for the thinnest melted layer obtained. The upper left-hand corner of the micrograph shows the non-porous, melted region free of surface cracks. As one looks down toward the lower right-hand corner, a gradual increase in porosity is evident. Finally, the as-recieved (untreated) surface is seen in the lower right-hand corner.

After achieving the thin, crack-free layer, the next step was to "sandwich" the porous inner bulk of the substrate between two melted layers. The same "optimal" processing parameters (table 1) were used (figure 27a). The melted layers run horizontally along the top and bottom of the substrate (specimen C12). The thickness of the bottom layer varies from approximately 30 to 70 microns, while the top layer is of a constant 100 micron thickness. One relatively large spheroidal pore approximately 10 microns in diameter is seen in the bottom layer. Again, no cracking is evident. We assume that this material now is "sealed" from the elements.

The graduation in surface porosity for the surface of the "sandwich" specimen in figure 27b exhibits the same

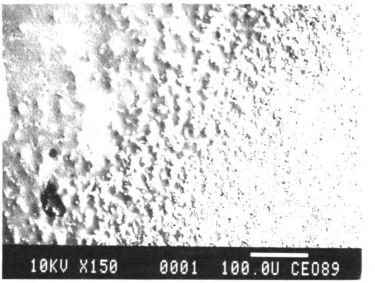

Figure 26. Graduation in surface porosity for the thinnest melted layer obtained (cordierite specimen C11).

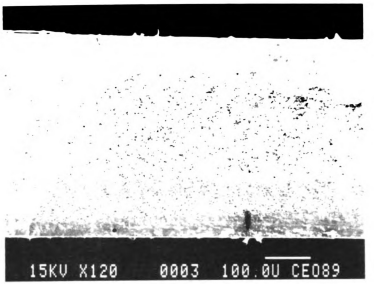

Figure 27a. Cordierite specimen C12 fabricated in a "sandwich" configuration. Note absence of cracking.

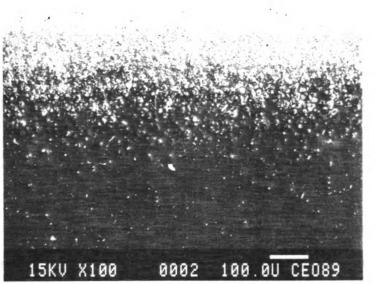

Figure 27b. Graduation in surface porosity for the cordierite "sandwich" specimen (C12).

characteristics as the previously mentioned treated surfaces. A number of white "flecks" can be seen in the transition region. These flecks are randomly distributed with an approximate average number density of 24 in a 400 square micron area. These flecks are not seen in the regions treated by the geometric center of the laser beam path.

Partially-treated colonies exist in the surface of treated specimen C13 (figure 29). A melted region surrounds a dark, amoeba-shaped partially melted colony. Flecks of unmelted material appear in this colony as well as zones of partially melted material. These colonies likely affect the roughness measurements carried out on the Dektak IIA. The profilometer results are discussed in detail in section 3.2.

3.1.5 Microstructure of CO_2 Laser Edge-Cut Specimens where Laser Cutting was Performed on X-Y Table with Maximum Translational Speed of 600 in/min.

Figures 29a through 29e illustrate cut edges of cordierite specimens C19 and C20. Figure 29a is a low magnification (10X) micrograph of a rectangular specimen cut from a 0.9mm thick as-received substrate. This figure clearly shows the CO_2 laser is capable of cutting the substrates rather than driving a crack through the material. The interior region of this specimen shows a dark, amoeba-shaped region surrounded by a brighter white region. This entire surface is untreated, and the contrast is likely due to charging effects in the scanning electron microscope. Also, a crack can be seen in the untreated surface, winding

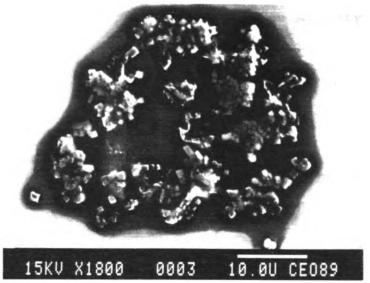

Figure 28. Partially melted colony in the surface of a laser-melted cordierite specimen (C13).

around the darker center region.

Figure 29b is the same specimen (C19) at higher magnification (30X). The edge-cut region is crack-free and clearly shows a smooth, uniform cut.

Figure 29c exposes a cross-section of edge-cut specimen C20. This specimen was fractured in bend, along a plane oriented normal to the specimen surface. A semi-circular melted region is shown as well as the porous, inner-bulk of the substrate. A high-viscosity melt and a rapid quench allowed the melted region to maintain a semi-circular shape during solidification. A ring of interior pores or "bubbles" is seen in the melted region. These pores do not reach the surface of the melt zone and would not likely inhibit the dielectric properties of the substrate.

Figure 29d is a higher magnification micrograph depicting the interface between the melted region and the porous inner-bulk of specimen C20. A dark pore approximately 40 microns in diameter is seen as well as a spheroidal "bubble" approximately 60 microns in diameter (a number of smaller bubbles and pores are also evident). A crack is seen running vertically through the 40 micron pore and terminating at the untreated interface. Good adhesion of the melted region to the untreated region is evident.

A higher magnification (1500X) clearly shows good adhesion of the melted region to the porous, inner-bulk of specimen C20 (figure 29e). No pores or cracks are

Figure 29a. Rectangular cordierite specimen C19 cut with the CO_2 laser from an as-received substrate.

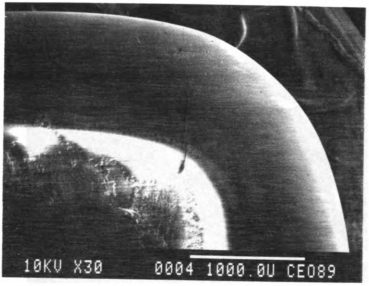

Figure 29b. Cordierite specimen C19 at higher magnification. Shows smooth, crack-free edge cut.

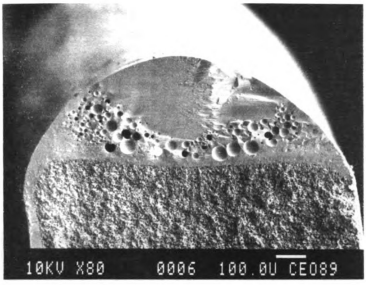

Figure 29c. Cross-section of edge-cut cordierite specimen C20.

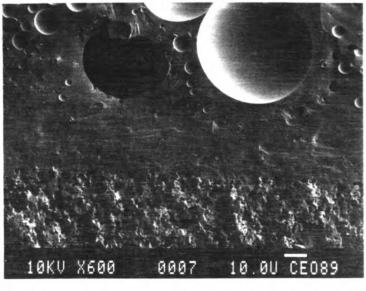

Figure 29d. Cordierite specimen C20 at higher magnification. Shows the interface between the melted region and the porous inner-bulk of the specimen.

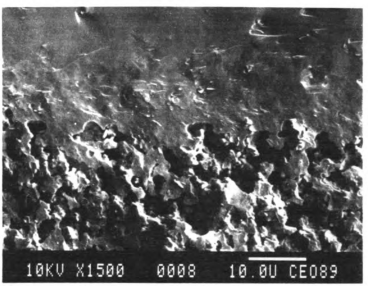

Figure 29e. Cordierite specimen C20 at even higher magnification. Shows good adhesion of the melted region to the porous, inner-bulk of the substrate.

evident in the laser-melted region at this higher magnification.

An idealized calculation of the volume of cordierite densified during laser treatment, compared to the remaining porous volume, shall be considered here. Consider an as-received cordierite substrate of dimensions 1cm x 1cm x .9mm. After CO_2 laser treatment, the substrate is densified. With a 10 micron thick densified layer on upper and lower surfaces of the substrate, the final thickness of the substrate is 0.88mm. Also consider that each of the four specimen edges were laser cut which resulted in a densified zone shaped (approximately) as a half-cylinder of radius 0.45mm (see figure 29c). The following ratios then can be calculated for this particular example: (1) neglecting edge-cuts, the ratio of the volume of densified material to the porous volume is approximately 0.022, (2) including edge-cuts, the ratio of the volume of densified material to the porous volume is approximately 0.13, and (3) the total reduction in volume due to laser-treatment is six percent. This calculation overestimates the densified volume, since the volume densified during edge-cutting is a segment of a cylinder with volume less than a half-cylinder (figure 29c).

3.2 Profilometry Results

Surface roughness profilometer traces taken on the Sloan Dektak IIA (figures 30 through 44) give insight into the practicality or useability of the laser-treated cordierite substrates. Surface roughness measurements on glass slides will be presented first as a comparative study. Untreated and laser-treated cordierite traces will then be analyzed. The goal is that the surface of the melted layer will be smooth enough to permit metallization of fine-line circuitry.

3.2.1 Profilometry of Glass Microscope Slides Used as Roughness Standards.

Figures 30 and 31 are profilometer traces of glass microscope slides (specimens G1 and G2) with pristine surfaces. The two slides were carefully removed from a new package of slides. The mirror-like finish on a microscope slide serves as a good reference for roughness measurements. Glass slide G1 (figure 30) exhibited a root-mean-square average roughness value of 299 angstroms. This number (RA = 299A) appears in the lower right-hand corner of the trace. The total vertical scale is a very sensitive 16,000 angstroms. Slide G2 had a roughness average of a mere 209 angstroms (figure 31). We now have a reference to work from. The sensitivity of the Dektak IIA is such that the rms values of the roughness of two glass microscope slides can vary by as much as 100 angstroms. What is more important is that we bear in mind that

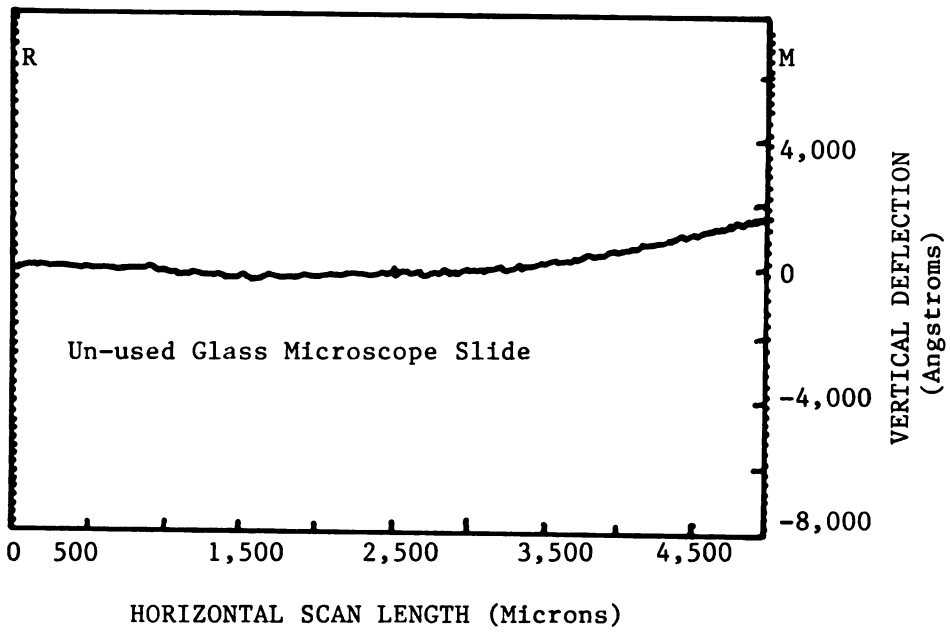

Figure 30. Profilometer trace of un-used glass microscope slide G1.

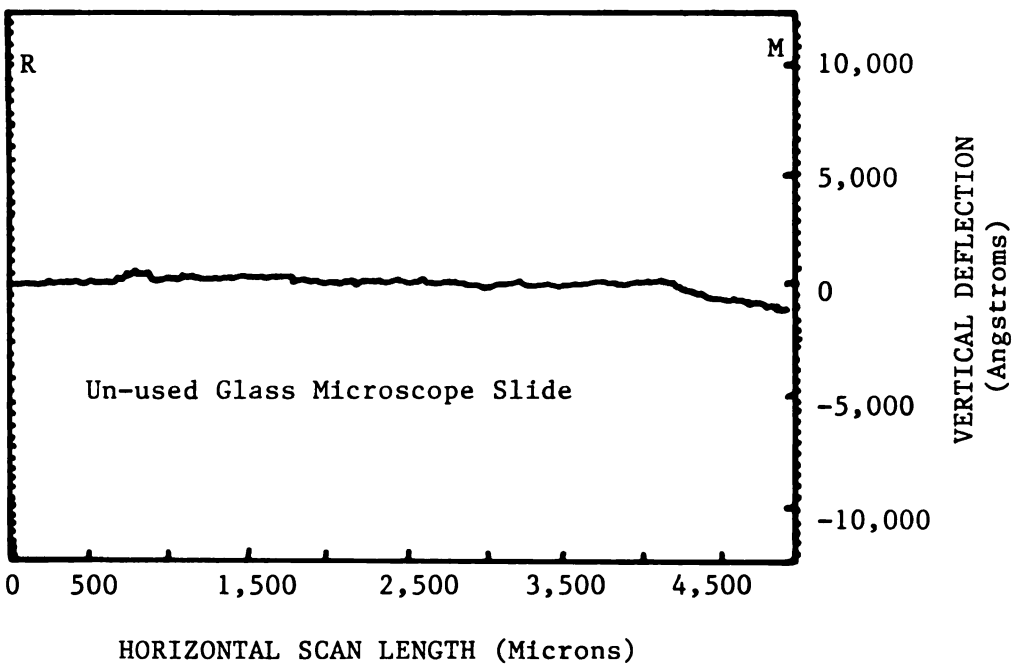

Figure 31. Profilometer trace of un-used glass microscope slide G2.

approximately 250 angstroms (average of the two slides) represents the average roughness of a glass slide.

3.2.2 Profilometry of As-Received Cordierite

Figures 32 through 34 show the surface roughness of untreated cordierite (specimens C14 through C16). A profilometer trace taken of the as-recieved, 0.4 millimeter thick cordierite specimen C14 shows a maximum peak reading of 150,000 angstroms and a minimum peak reading of -275,000 angstroms (figure 32). Roughness averages of this material appear in later figures, as the treated specimens were all of the 0.4mm thick substrates.

The average roughness of the as-recieved 0.9mm thick specimen C15 is 33,338 angstroms (figure 33a). The large-scale deflections such as the one shown in figures 33a and 33b are not included in the average roughness calculation. These topographical features are included in the profilometer trace but are ignored by the Dektak IIA for rms surface roughness calculations. Only local vertical perturbations are of interest (see figure 33b) in computing the average surface roughness.

Figure 34 shows a roughness average of 36,236 angstroms for the as-recieved 0.3mm thick specimen C16. This material generally showed a large amount of topographical roughness. These substrates were virtually un-useable because of their extensive surface roughness and were only briefly studied.

3.2.3 Profilometry of Laser-Treated Cordierite

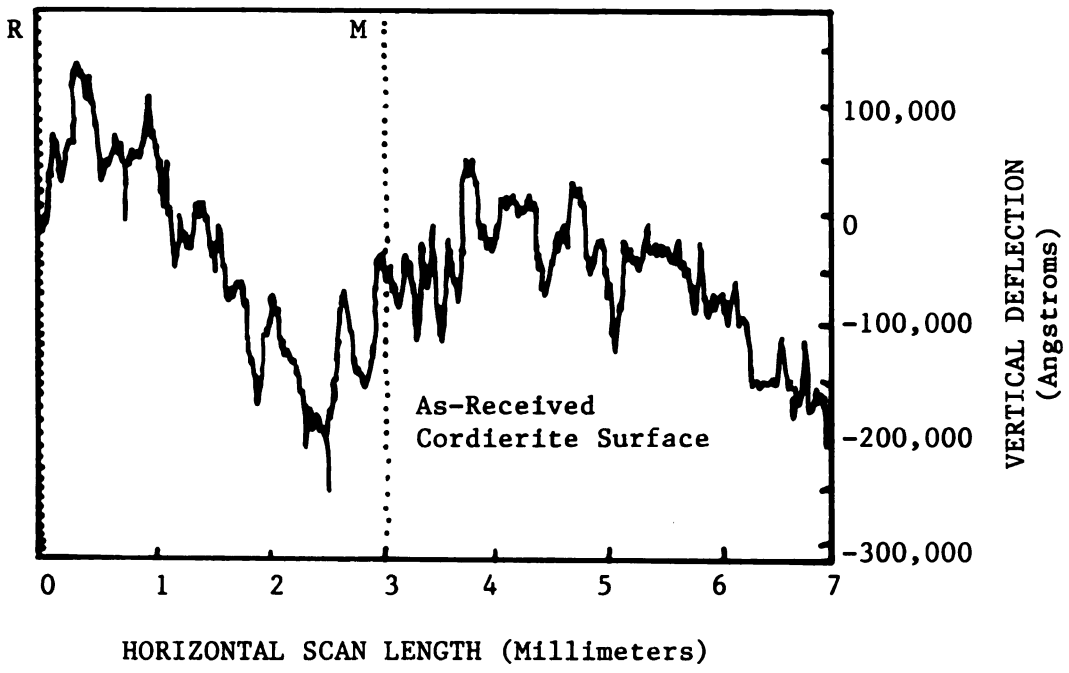

Figure 32. Profilometer trace of as-received cordierite specimen C14.

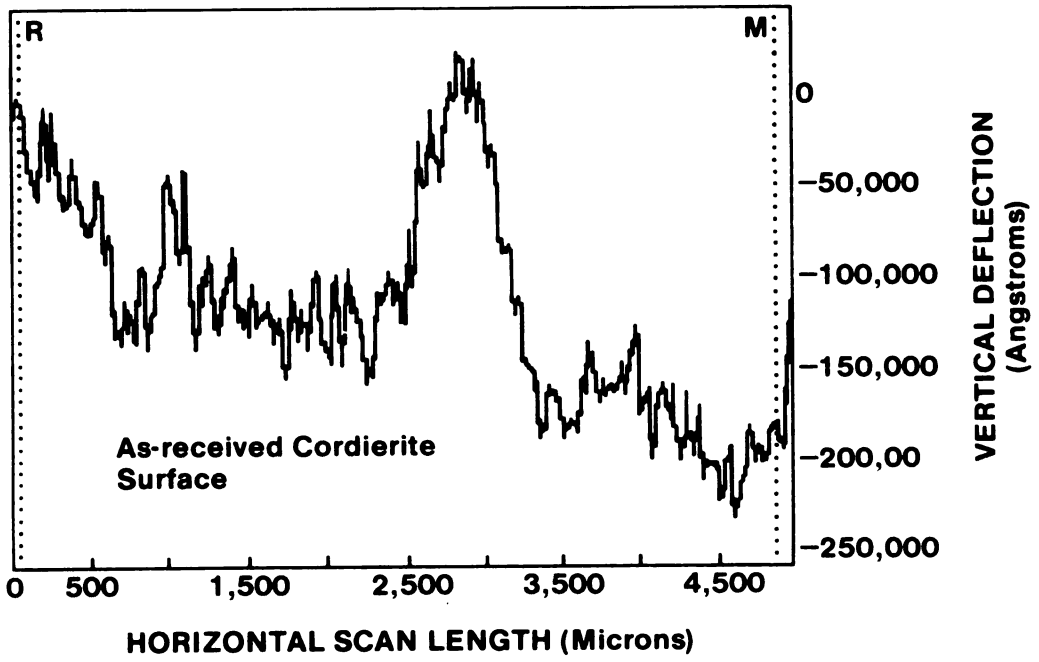

Figure 33a. Profilometer trace of as-received, 0.9mm thick cordierite specimen C15.

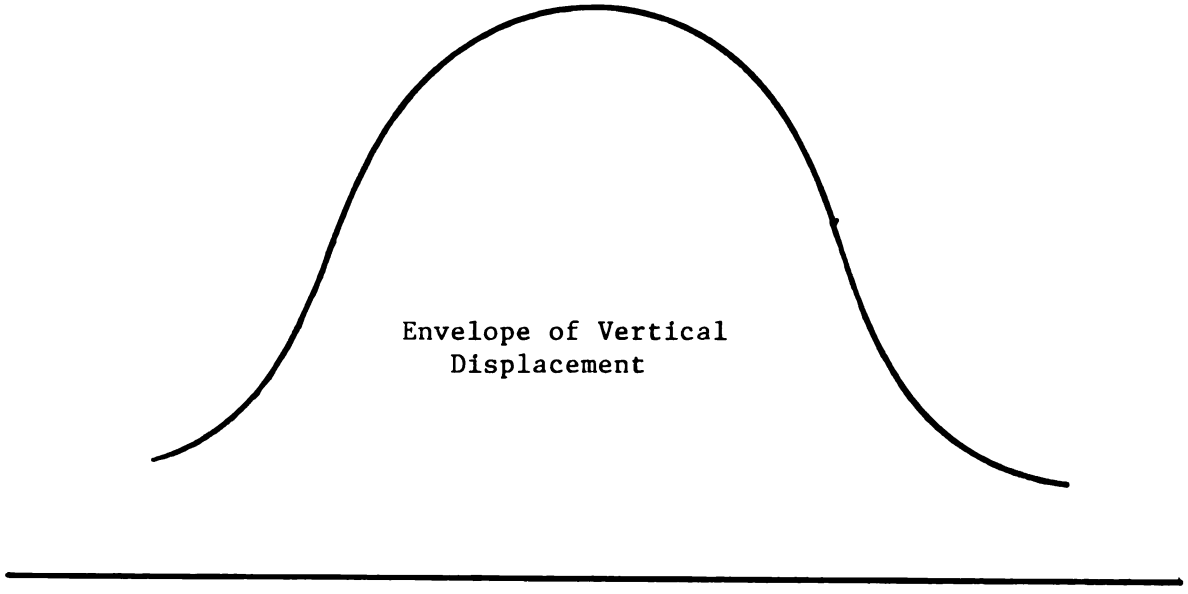

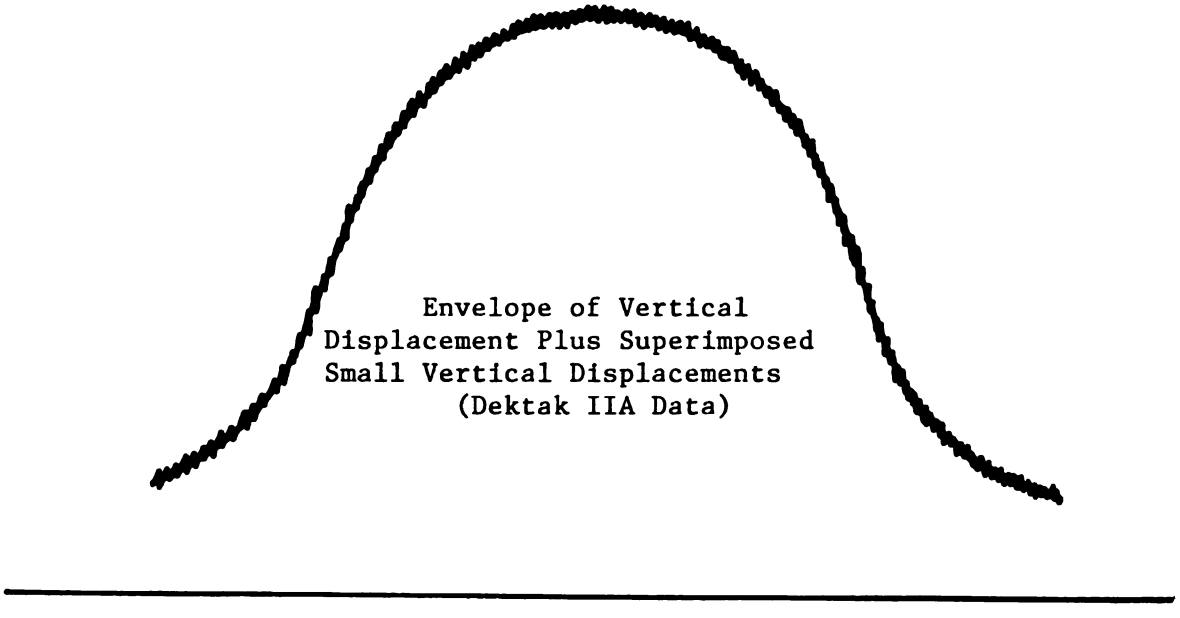

Figure 33b. Schematic representation of local vertical deflections used for rms roughness calculations.

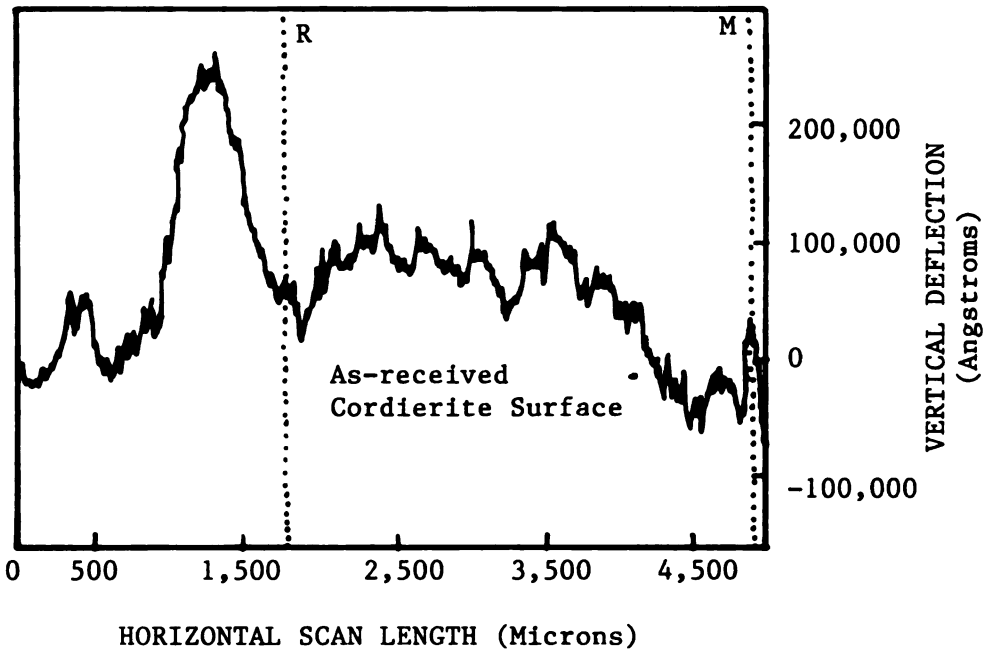

Figure 34. Profilometer trace of as-received, 0.3mm thick cordierite specimen C16.

The surface scanned by the outskirts of the gaussian intensity profile of the carbon dioxide laser beam shows large-scale deflections. The horizontal lines at the bottom of the trace in figure 35 (specimen C4) indicate the regions where the stylus exceeded the lower limit of vertical deflection. The high surface roughness would likely make this specimen unsuitable for metallization.

A 3 millimeter scan through the geometric center of the melt path of the laser beam (figure 36, specimen C4) shows large-scale deflections that may be related to the use of the older X-Y table during laser treatment.

A Nd:YAG laser-treated specimen (figure 37) shows a very high average surface roughness of 56,185 angstroms. The YAG laser was judged not suitable for surface treatment because of the rough, cobblestone-like condition of the surface.

Figure 38 shows another trace of untreated cordierite. Its surface roughness, 26,132 angstroms, is likely not suitable for metallization. Figure 39 is the same specimen and shows the transition from an untreated to a treated zone along the surface. The scan length was 10mm, with a total vertical scale of 600,000 angstroms. The "M" cursor is positioned on the transition zone, and the rms roughness calculated for the untreated portion (24,415 angstroms). A large-scale depression in the smoother, treated region results from densification during melting as a result of

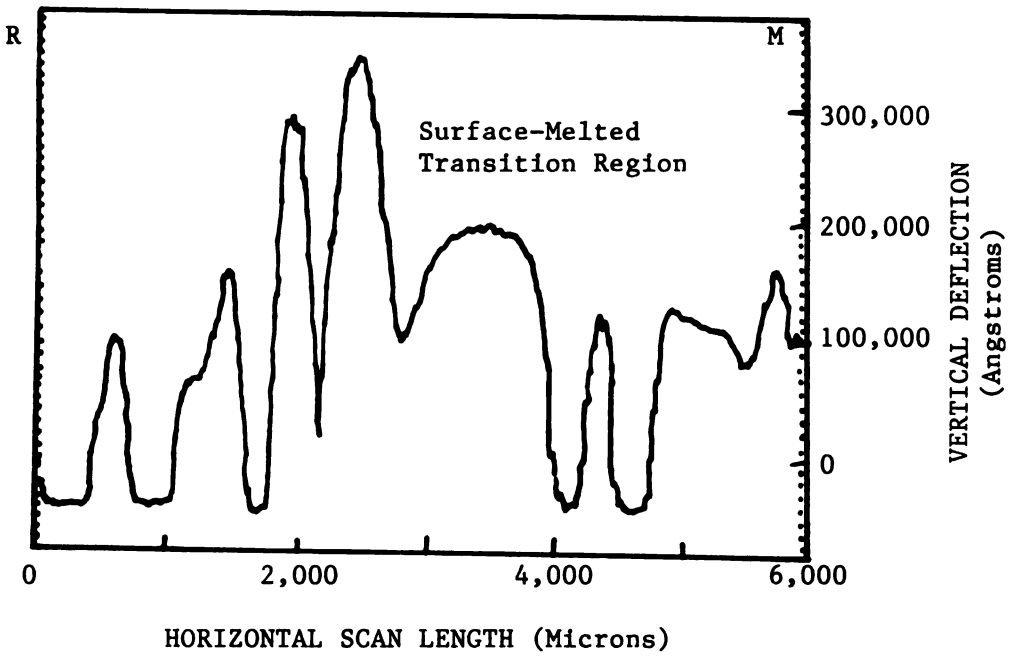

Figure 35. Profilometer trace of a laser-treated specimen scanning the transition region between the porous and surface-melted regions of the specimen. As discussed in section 3.1, the microstructure was formed by laser interaction with the outskirts of the gaussian beam (cordierite specimen C4).

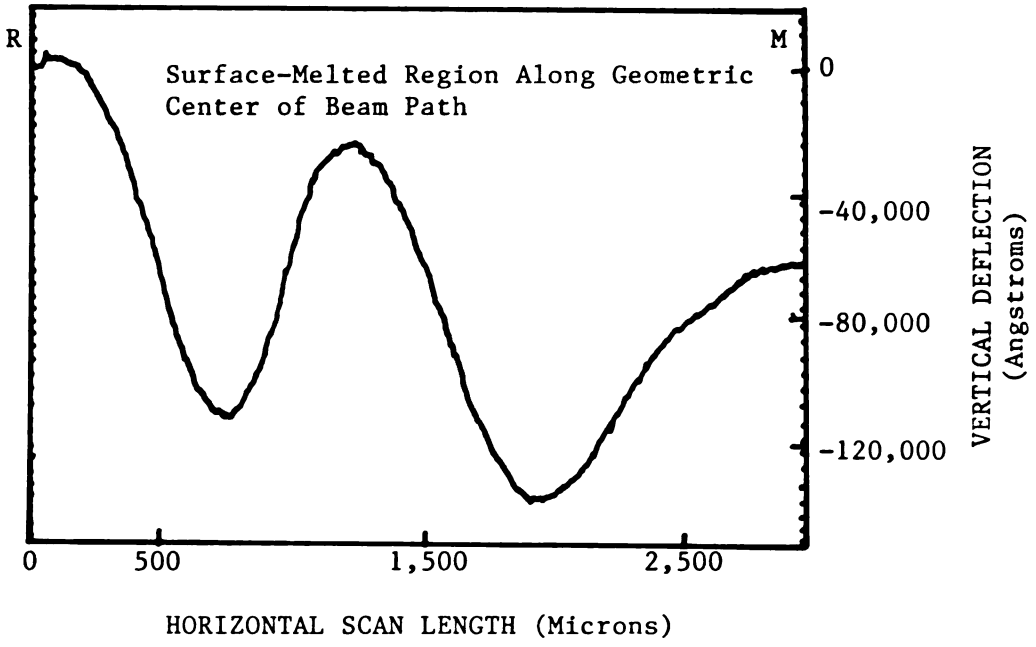

Figure 36. Profilometer trace of CO_2 laser-treated cordierite along the geometric center of the laser beam path (specimen C4).

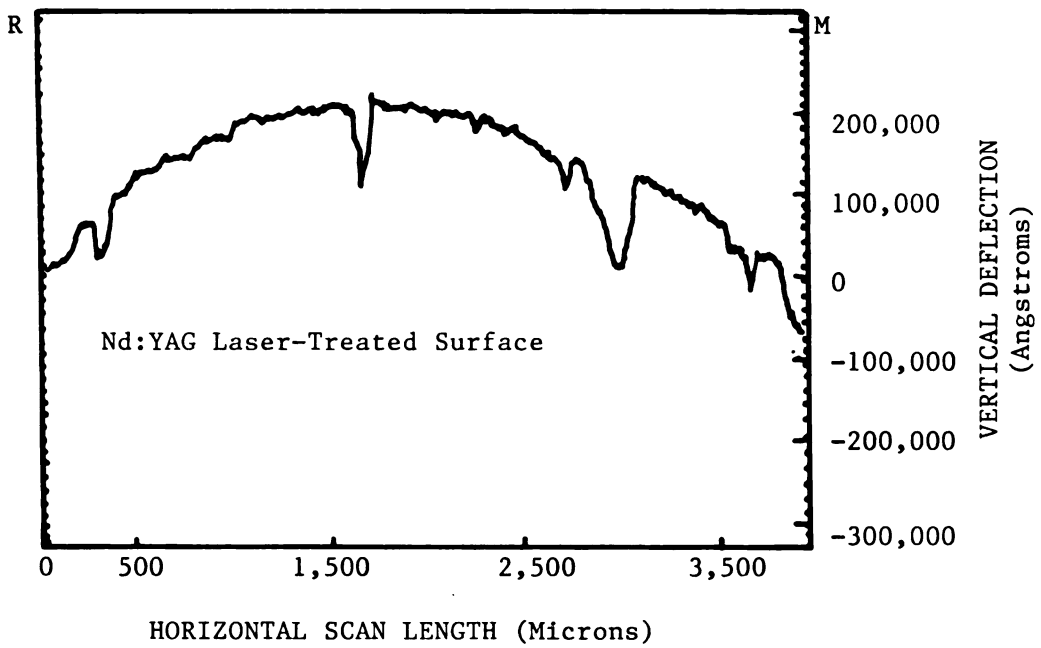

Figure 37. Profilometer trace of Nd:YAG laser-treated cordierite specimen C8.

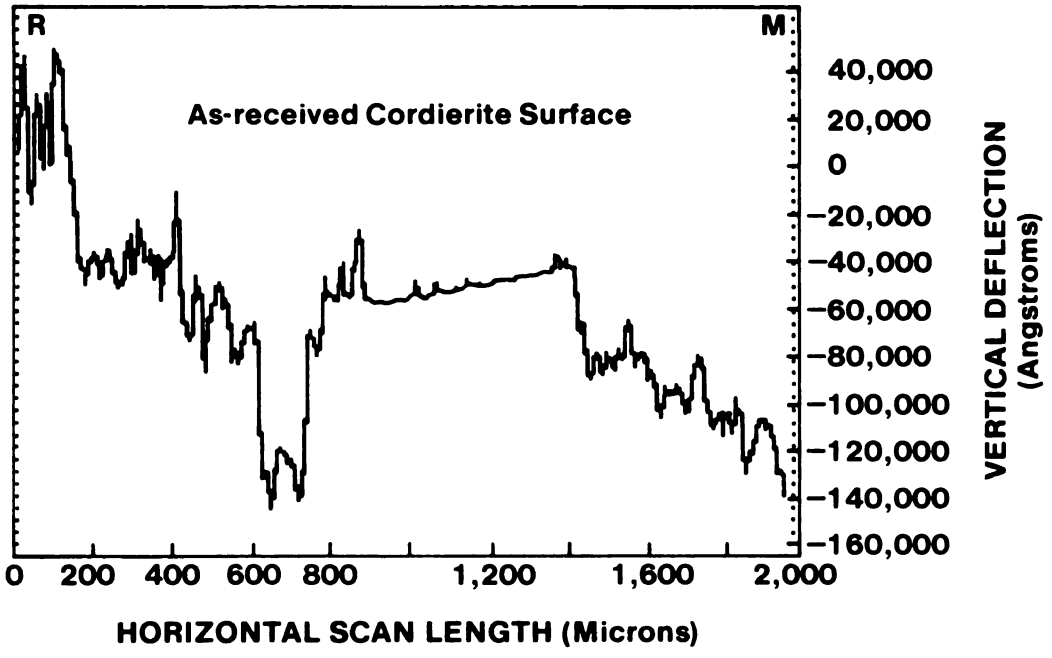

Figure 38. Profilometer trace of the untreated cordierite surface (specimen C17).

a reduction in porosity. A 10,000 angstrom surface depression typically resulted from laser surface-melting of cordierite substrates but the magnitude of this "dip" depends on the depth of the surface-melted layer.

Figure 40 is a 2mm scan along the surface of a treated region. A low roughness average of 6,333 angstroms was produced by local stylus deflection. Again, the trace appears to monotomically increase, indicating that the stylus was "climbing a hill" or undergoing large-scale deflection upward.

For laser-treated specimen C18, the dip shown in the trace (to the right of the "M" cursor in figure 41) clearly shows a densification which took place. The roughness average of the treated region of specimen C18 (figure 42) is 6,867 angstroms, which is less than one sixth of the value for the untreated region.

For treated specimen C11, densification is apparent as is a decrease in surface roughness (figure 43). The rms roughness average for the laser-treated region (figure 44) was 6,768 angstroms which is less than six times the value for the untreated region. The rms roughness value of about 7,000 angstroms is consistant with the rms roughness computed for the other laser-treated specimens.

The information available in profilometer traces and scanning electron micrographs can be used to predict the following: First, the "dip" shown in a profilometer trace allows for calculation of the thickness of the melted

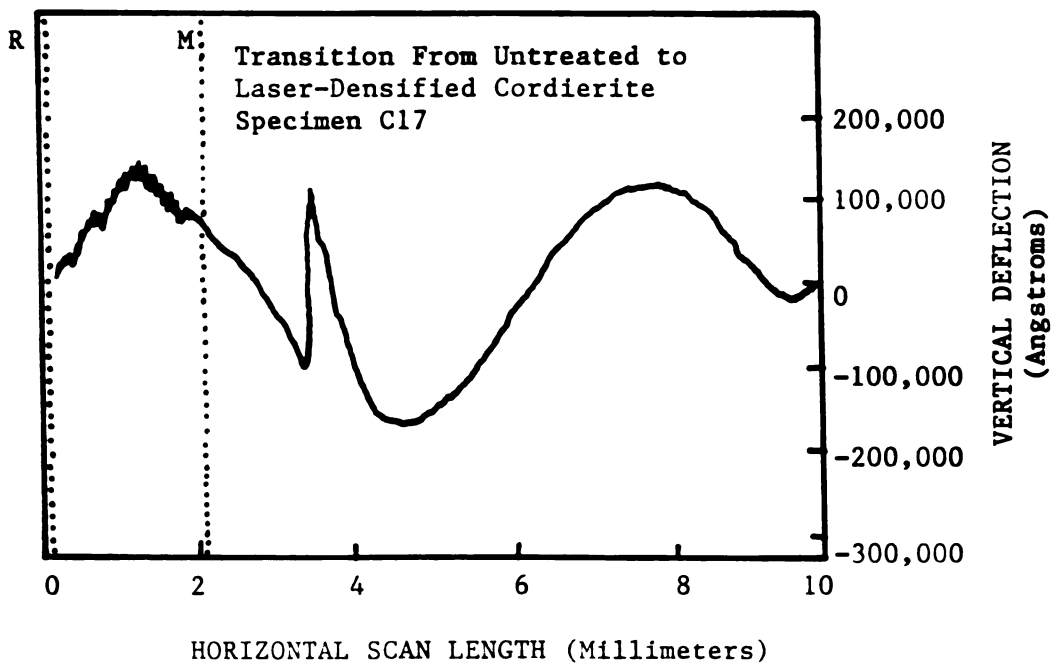

Figure 39. Profilometer trace showing the transition from untreated to laser-treated cordierite (specimen C17).

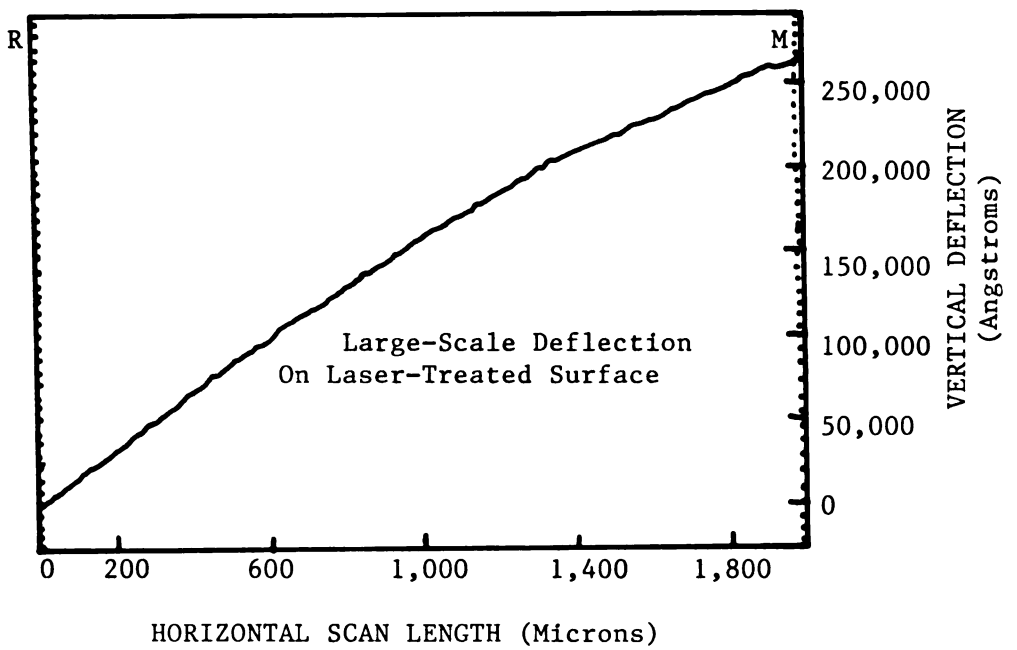

Figure 40. Large-scale deflection on laser-treated surface (cordierite specimen C17).

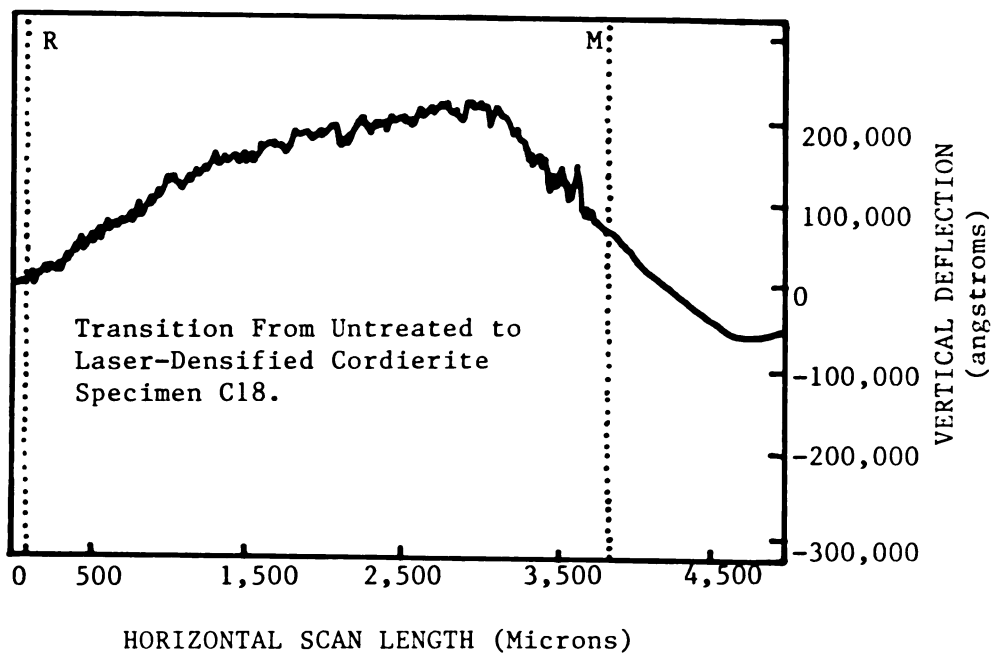

Figure 41. Profilometer trace showing the transition from untreated to laser-treated cordierite (specimen C18).

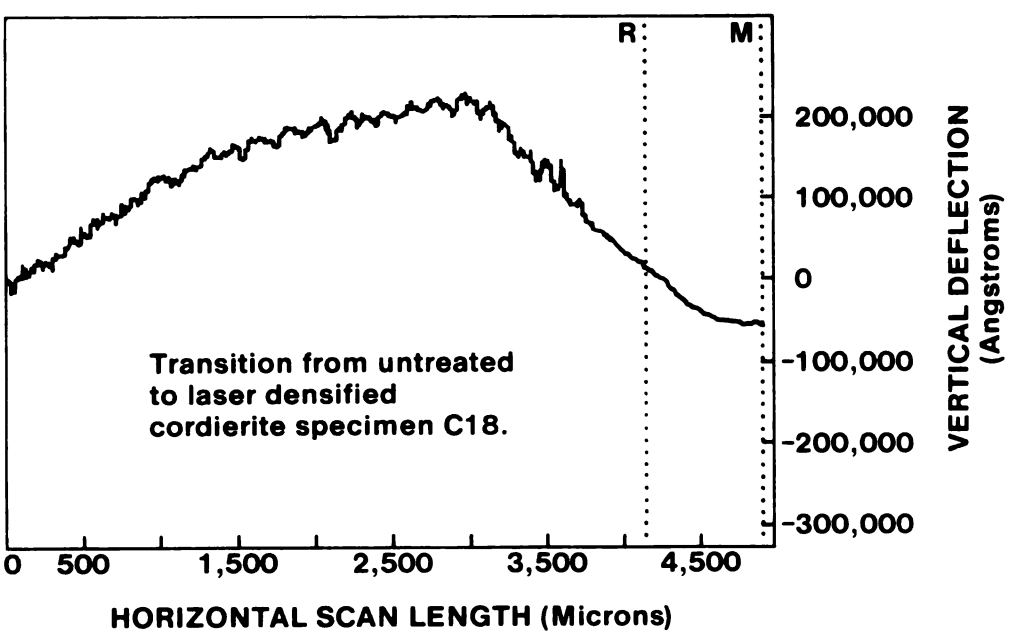

Figure 42. Transition from untreated to laser-treated cordierite (specimen C18).

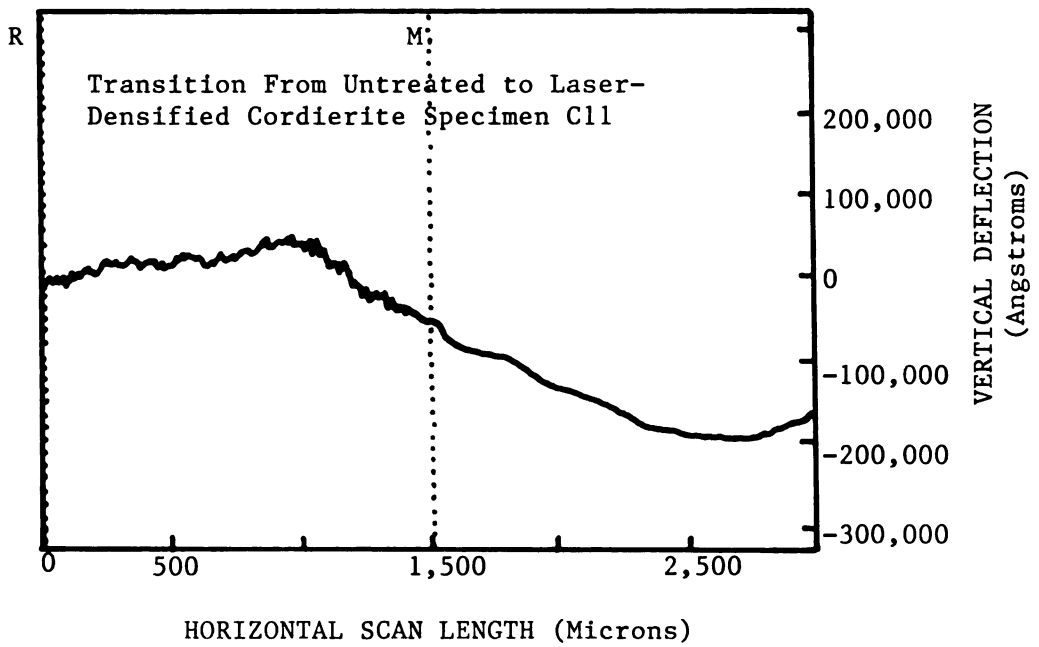

Figure 43. Transition from untreated to laser-treated cordierite (specimen C11).

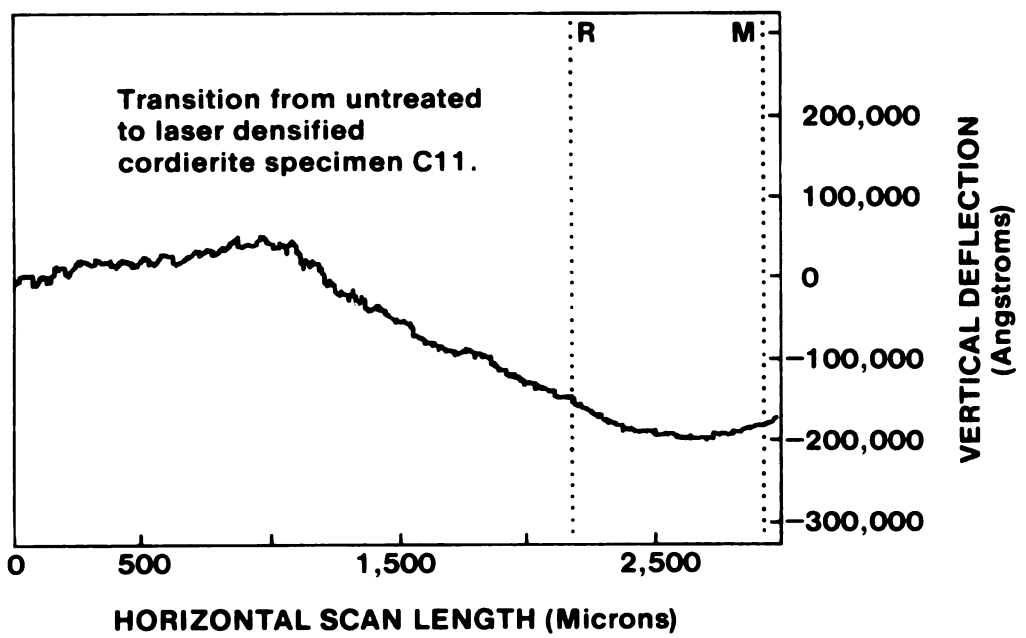

Figure 44. Transition from untreated to laser-treated cordierite (specimen C11).

layer (if the amount of material before densification is known). Second, the thickness of the melted layer shown in a scanning electron micrograph can be used to calculate the extent of the "dip" according to:

$$T = U - V_f(U) = U\ (1-V_f) \qquad (10)$$

Where $d=V_f(U)$ = extent of "dip" (in microns), T = thickness of the melted layer (in microns), U = amount of untreated material (in microns), and V_f = as-received volume fraction of porosity = 0.46 [8]. Therefore, if the amount of untreated material to be laser-densified is known (by microstructural examination), the topographical "dip" can be calculated. As a check, consider the profilometer trace in figure 44 (cordierite specimen C11) which shows a 20 micron "dip". Also consider the micrograph in figure 25 (same cordierite specimen C11) showing a 20 micron thick melted layer. In this case, U is 50 microns (obtained from SEM examination).

$$d = V_f(U) = 0.46 * 50 \text{ microns} = 23 \text{ microns}$$

$$T = 50 \text{ microns} - 23 \text{ microns} = 27 \text{ microns}.$$

Therefore, theoretically the "dip" should be 23 microns and the melted layer should be 27 microns thick. These numbers approximate the experimentally observed values.

3.3 X-Ray Diffraction Analysis

Experimental values for peak intensities and 2θ angles were tabulated and compared to published powder patterns by the National Bureau of Standards (see appendix D for the tabulated values and comparisons). NBS researchers found two crystalline forms of cordierite, which were labeled as "high-cordierite" and "low-cordierite" [36]. According to NBS monograph 25 [36], "high-cordierite" differs from "low-cordierite in that "high-cordierite" was prepared from stoichiometric mixtures of the oxides as a glass devitrified at 1,000^{o}C for 16 days. "Low-cordierite" was devitrified at 1,000^{o}C for 3 days, and then at 1,380^{o}C for 7 days [36]. At room temperature, "high-cordierite" has a hexagonal crystalline structure with lattice parameters: a = 9.770A and c = 9.352A. Room temperature "low-cordierite" has an orthorhombic crystalline structure with lattice parameters: a = 9.721A, b = 17.062A, and c = 9.339A. Table D7 compares experimental data from this study with the published patterns.

The specimens included in this study appear to be "high-cordierite". The d-spacings up to a 2θ value of 21.6^{o} agreed with the "high-cordierite" data [36] to within plus or minus 0.19A. For 2θ values greater than 21.6^{o}, the values are exactly coincident with the published values for "high-cordierite" [36]. Also the

relative intensities, although not numerically exact, are directly proportional to the published values for "high-cordierite" [36].

X-ray diffraction of laser-treated cordierite with with subsequent anneals was done to determine what crystalline phases, if any, existed in the surface-melted layer (figures 48 through 51). The presence of an amorphous "hump" in the laser-treated material indicates that the melted layer contains a significant volume of a glassy phase (figure 48). This was expected since cordierite is a silicate (recall the chemical formula for cordierite is $2MgO*2Al_2O_3*5SiO_2$). The trace in figure 49 was taken using the more sensitive 1000 cps range. One peak, at $2\theta = 16.4^{o}$, disappears into the hump upon annealing in air at a temperature of $900^{o}C$ and an annealing time of 2 hours. We believe that this metastable peak came from mullite since 2:2:5 cordierite is an incongruently melting compound in the mullite phase field (the ternary phase diagram is contained in appendix F). This 16.4^{o} peak has a relative intensity of 48 in mullite. This is a substantial mullite peak and it is not present in untreated "high-cordierite".

Annealing experiments were then conducted to determine if the peaks of high-cordierite would again grow to regain the original crystal structure. If this was the case, thermal expansion mismatch would not be a problem in the service environment. Negligible interfacial stresses could not produce a decohesion at the melted layer - inner bulk interface during thermal cycling. The substrate therefore

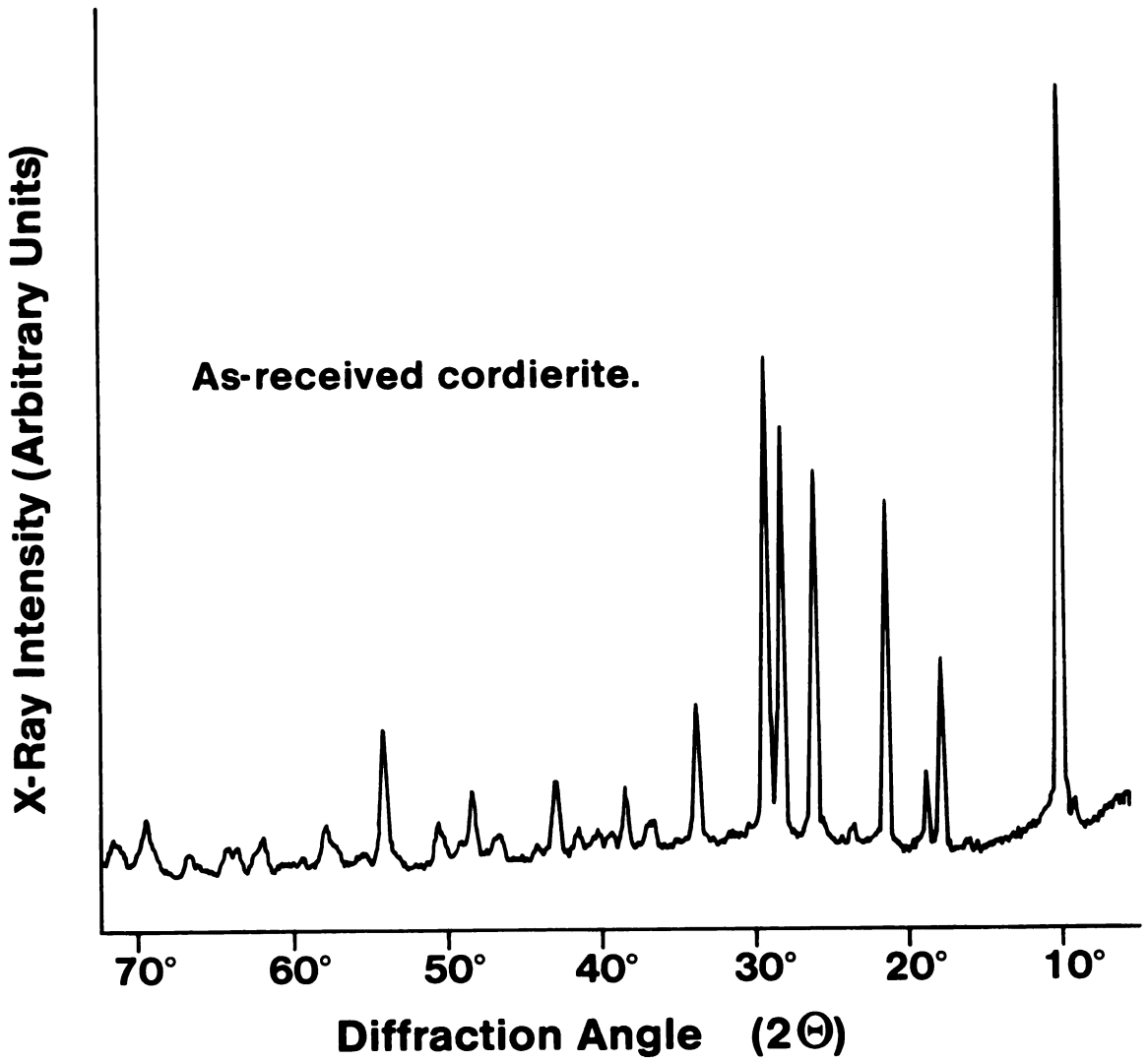

Figure 45. Diffractometer trace for the as-received, 0.4mm thick cordierite.

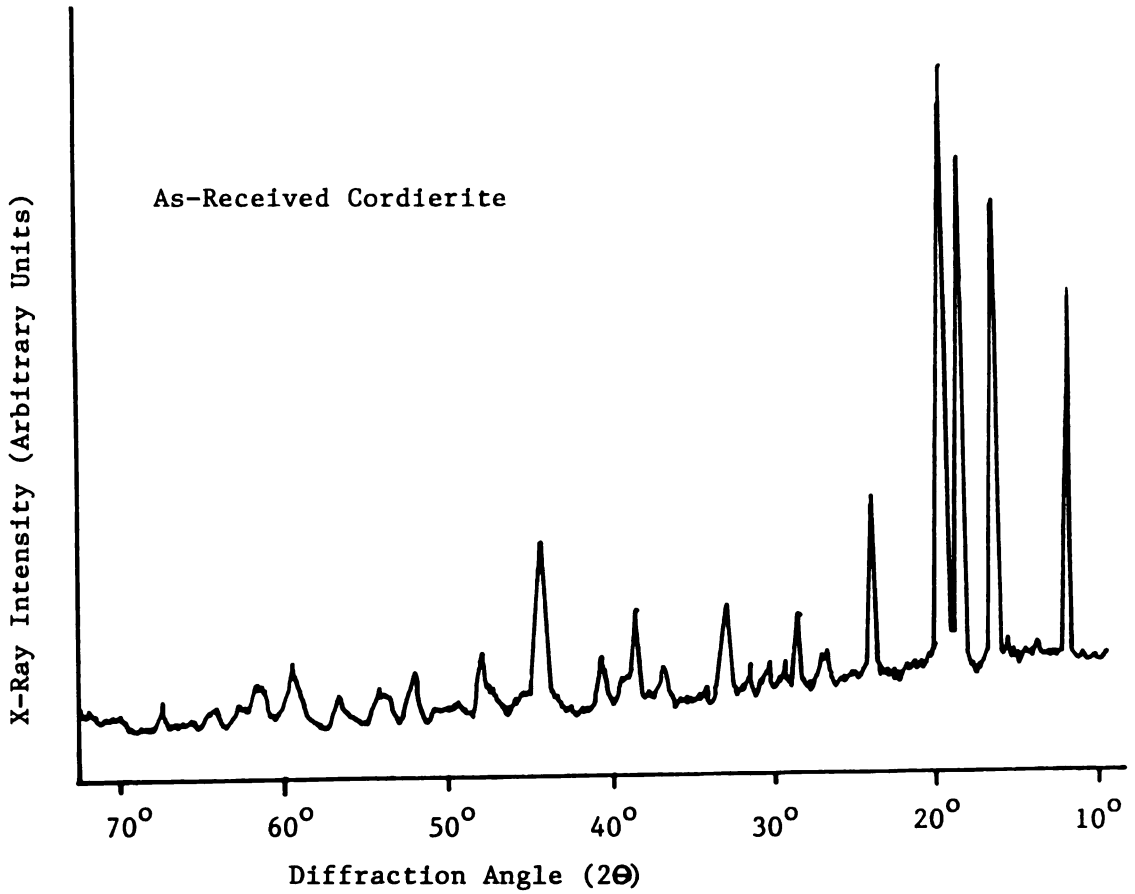

Figure 46. Diffractometer trace for the as-received, 0.9mm thick cordierite.

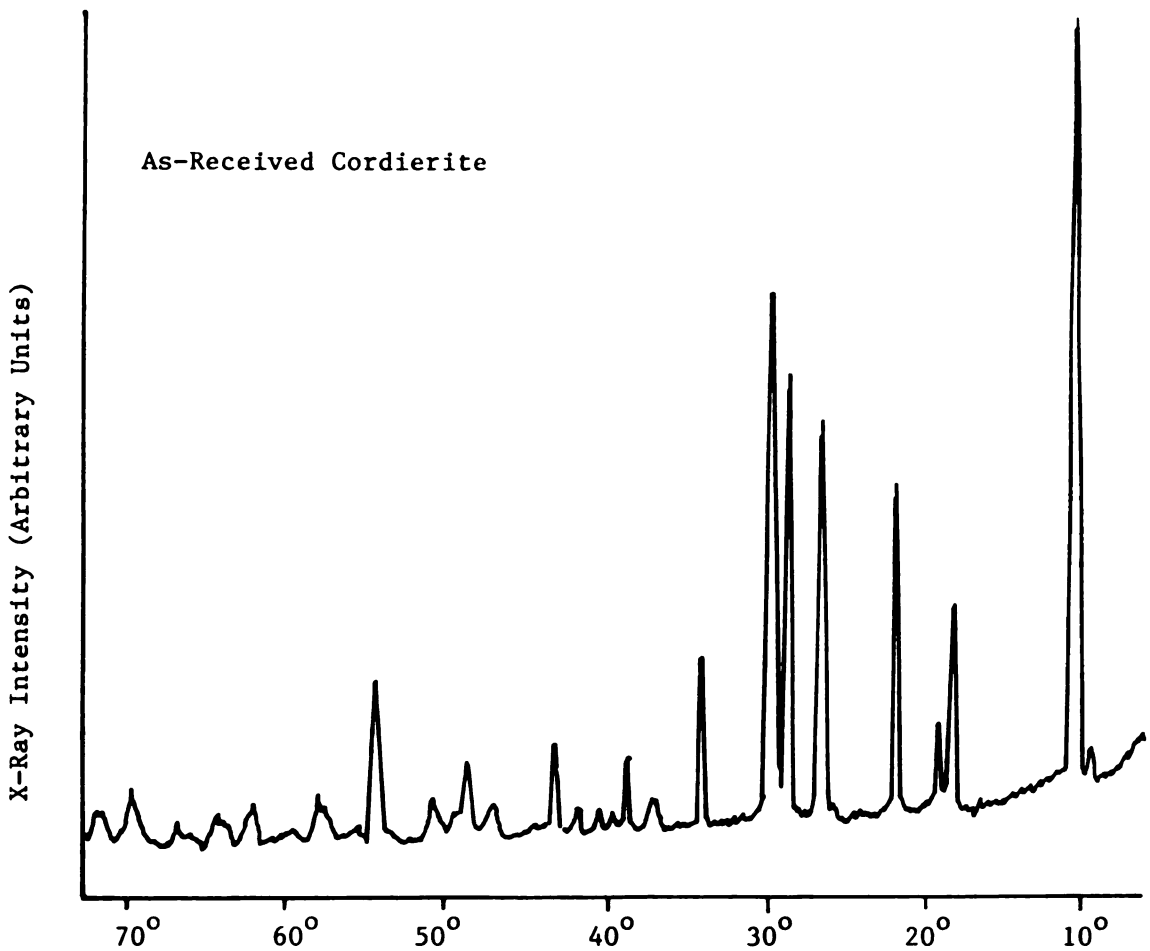

Figure 47. Diffractometer trace for the as-received, 0.3mm thick cordierite.

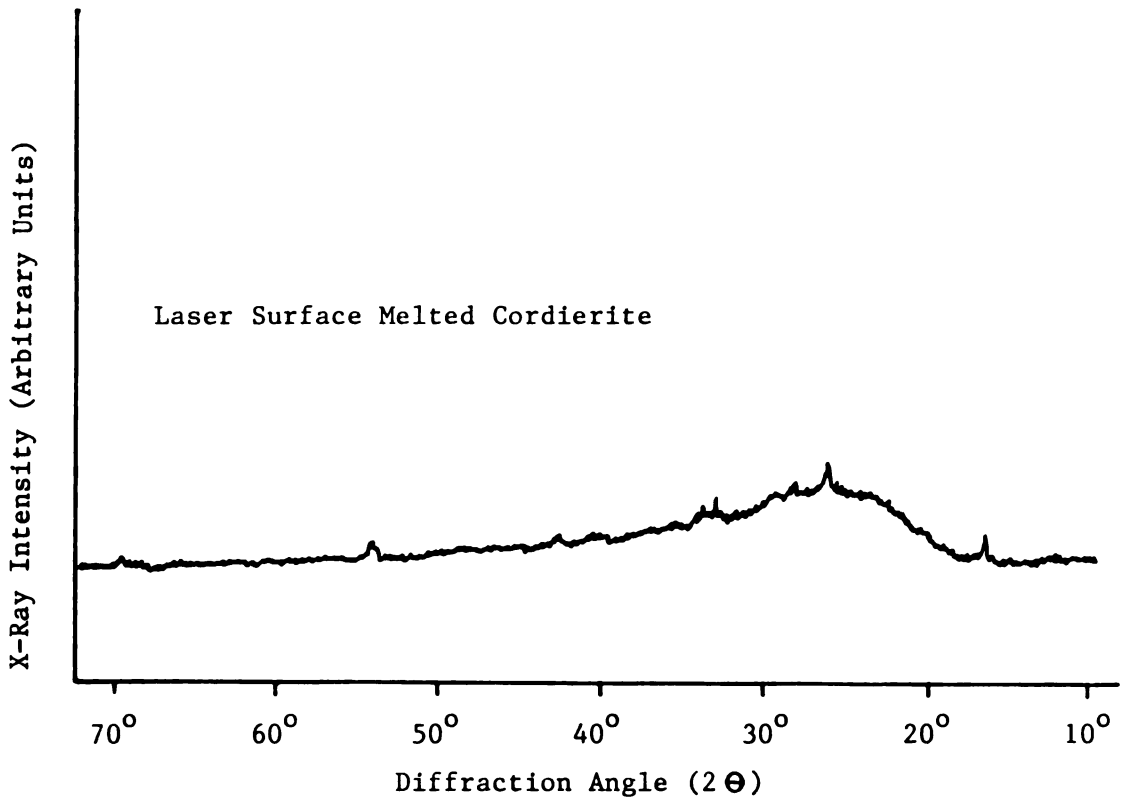

Figure 48. Diffractometer trace of laser-treated material showing the presence of an amorphous hump in unannealed cordierite specimen C21.

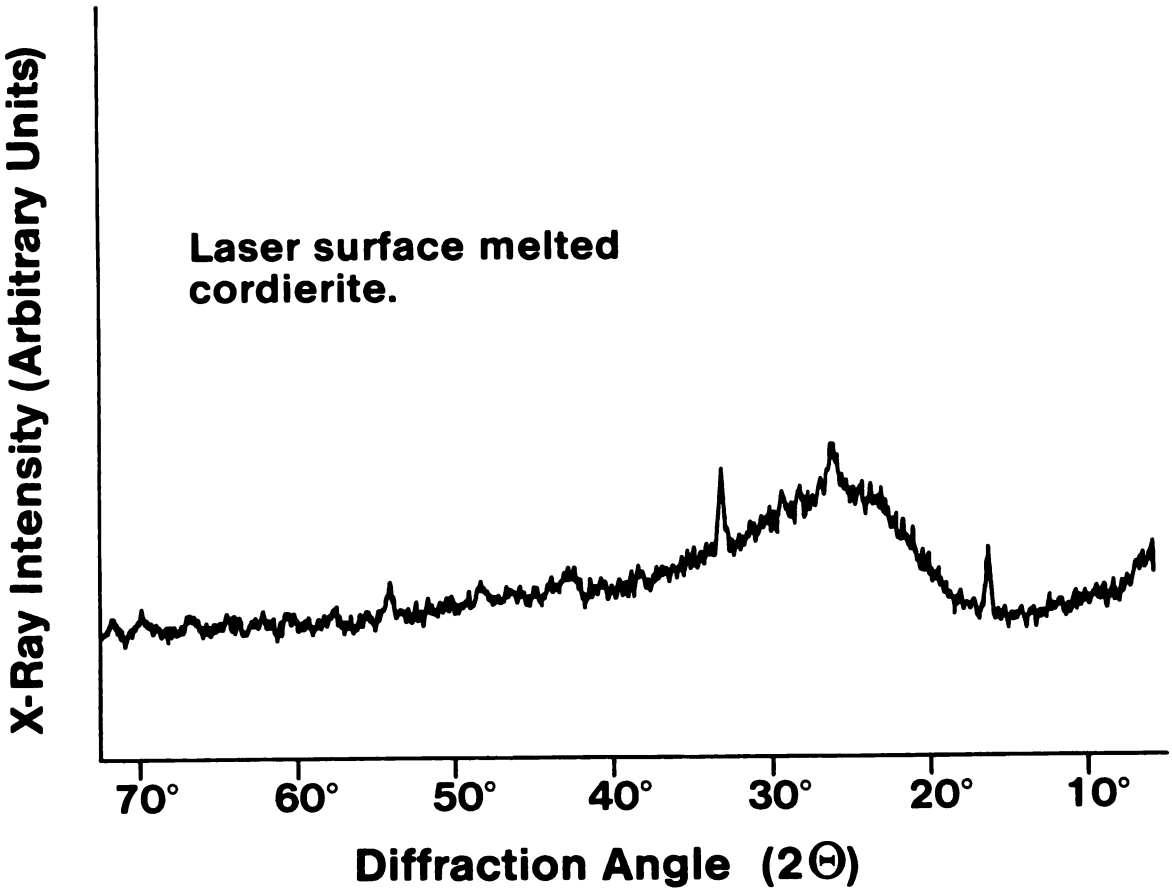

Figure 49. Diffractometer trace of laser-treated material showing the presence of an amorphous hump in unannealed cordierite specimen C21.

would maintain its mechanical integrity. After two anneals at 900°C for two hours (figures 50 and 51) the original "high-cordierite" peaks grew from the amorphous hump. Furnace cooling followed each anneal to prevent thermal shock damage.

After the arrival of the 0.9mm thick substrates, new x-ray diffraction specimens were fabricated with the CO_2 laser. The entire 60mm X 60mm surface of the substrate was melted, again using the X-Y table to scan the specimen under the laser beam. However, these specimens contained a large amount of cracks and surface depressions, which may have hindered the diffraction procedure as some curious results were obtained. The surface depressions were evenly spaced, with an approximate 4 millimeter peak-to-peak separation. The depth of these depressions was approximately 0.2 millimeters. Previous specimens were usually fabricated with one pass, therefore this periodic pattern of surface depressions did not exist.

A trace of laser-treated, unannealed 0.9mm thick specimen C22 shows a relatively large peak at $2\theta = 10.2^{\circ}$ ($I/I_o = 40$, figure 52), which is the 100 intensity peak of the as-recieved material. An amorphous hump is also present.

After two anneals (900°C for a total of 4 hours with a furnace cool) the 100 intensity peak failed to grow (figures 53 and 54). A few cordierite peaks, however, can be seen

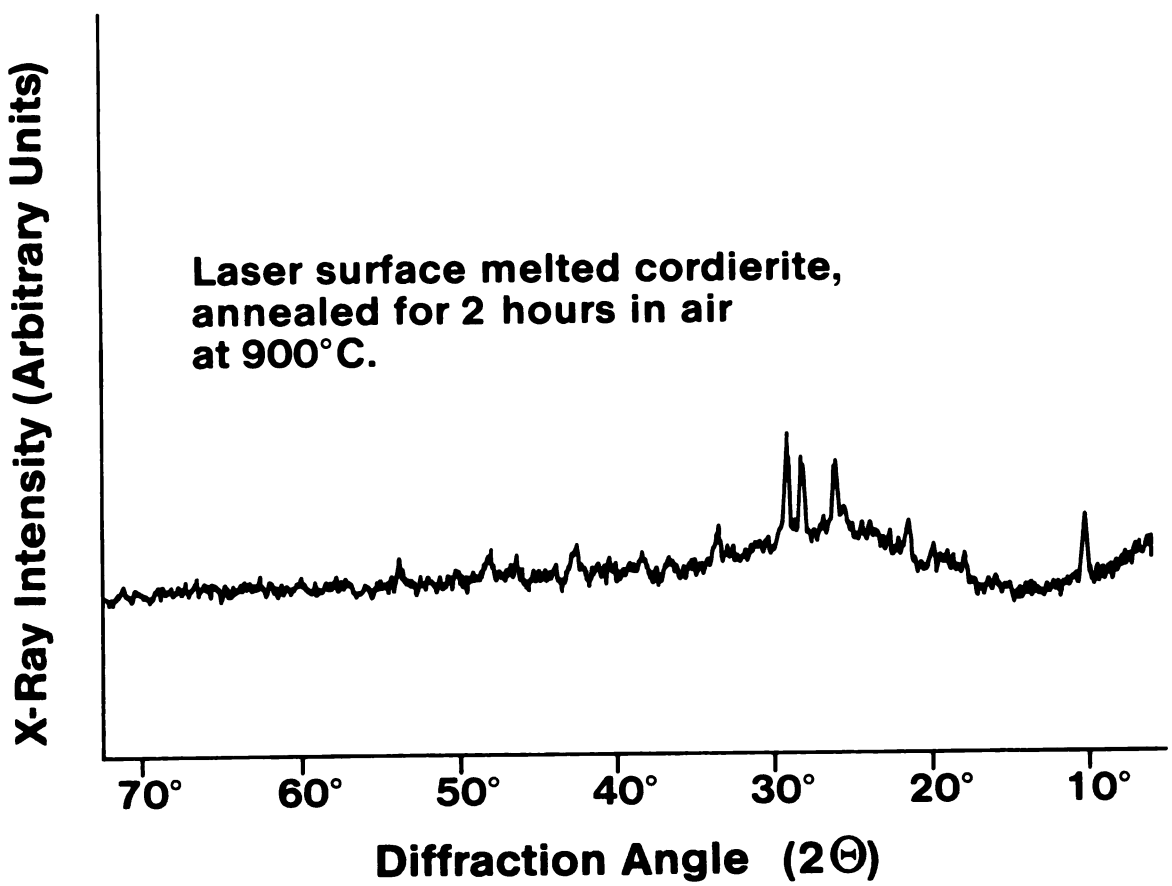

Figure 50. Diffractometer trace of cordierite specimen C21 after the first 900°C anneal for two hours.

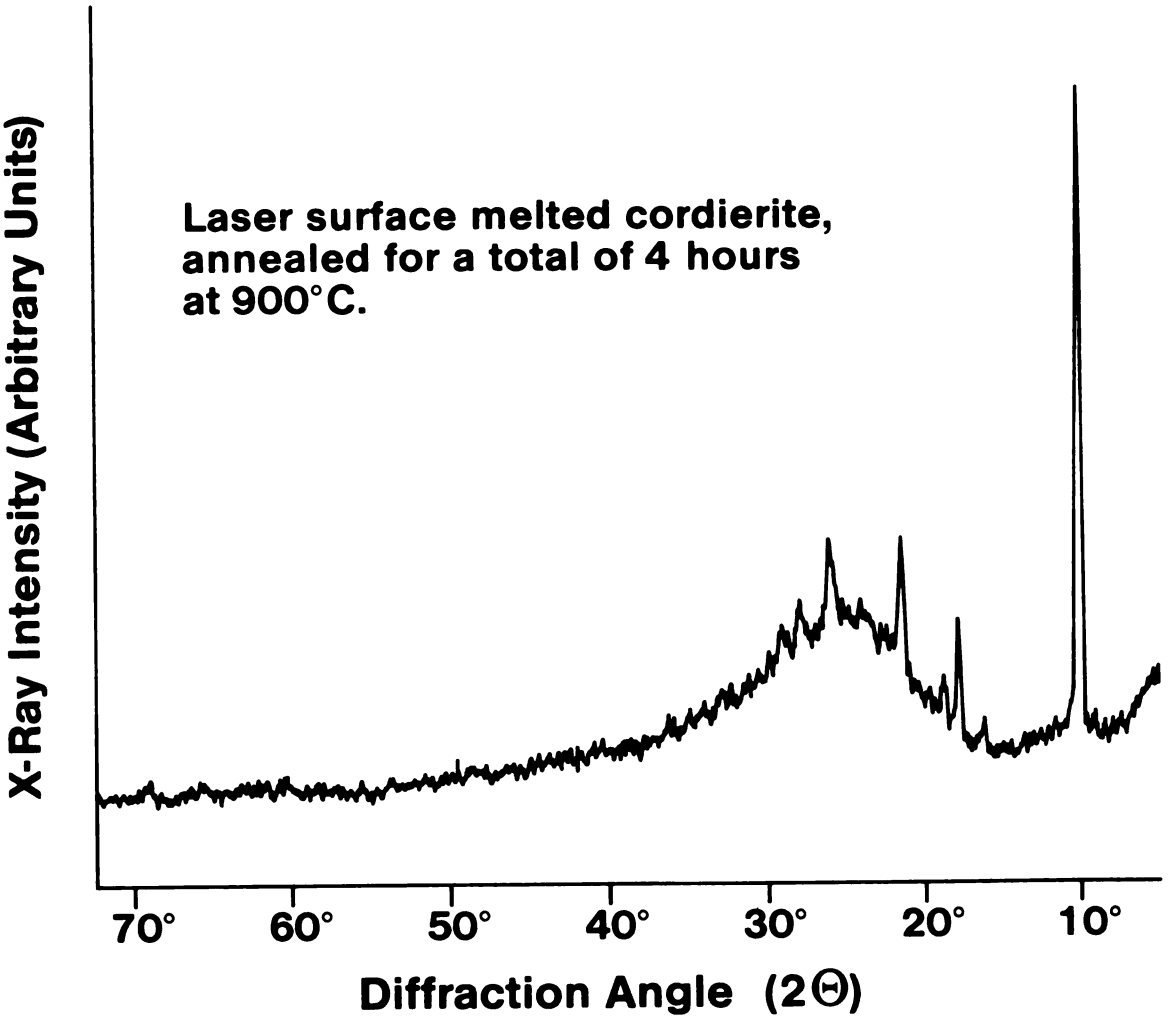

Figure 51. Diffractometer trace of cordierite specimen C21 after the second 900°C anneal for two hours.

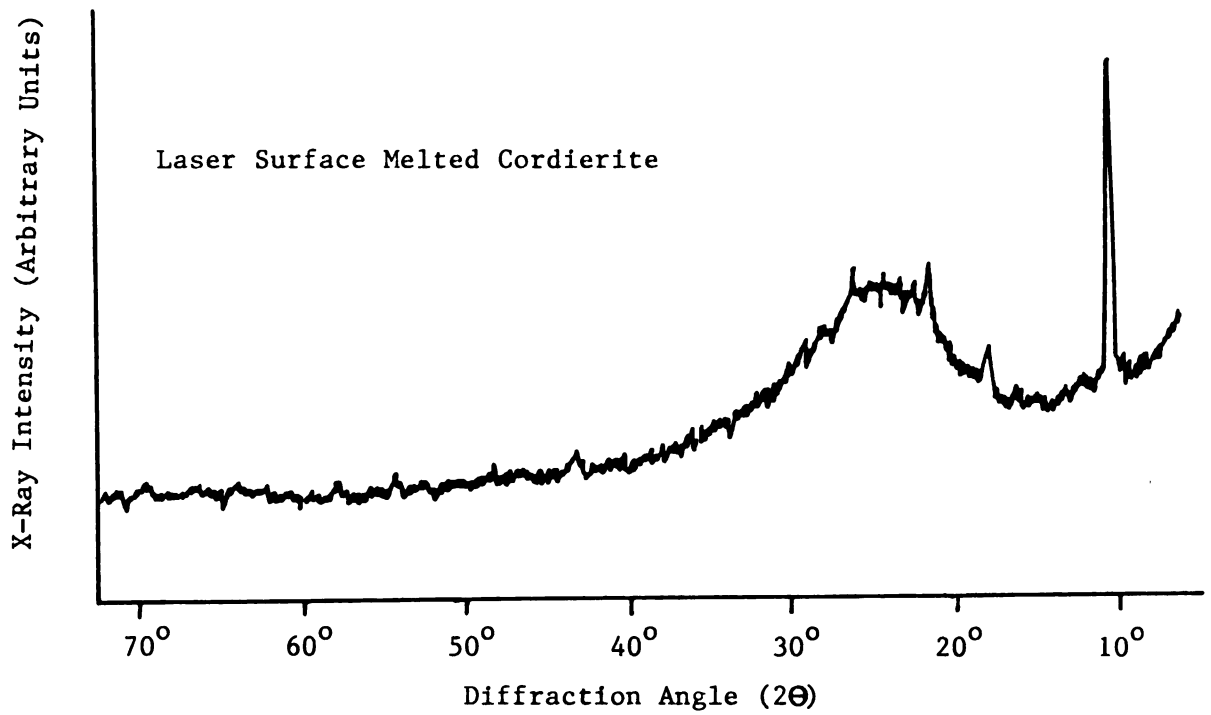

Figure 52. Diffractometer trace of laser-treated, 0.9mm thick cordierite specimen C22 with no anneal.

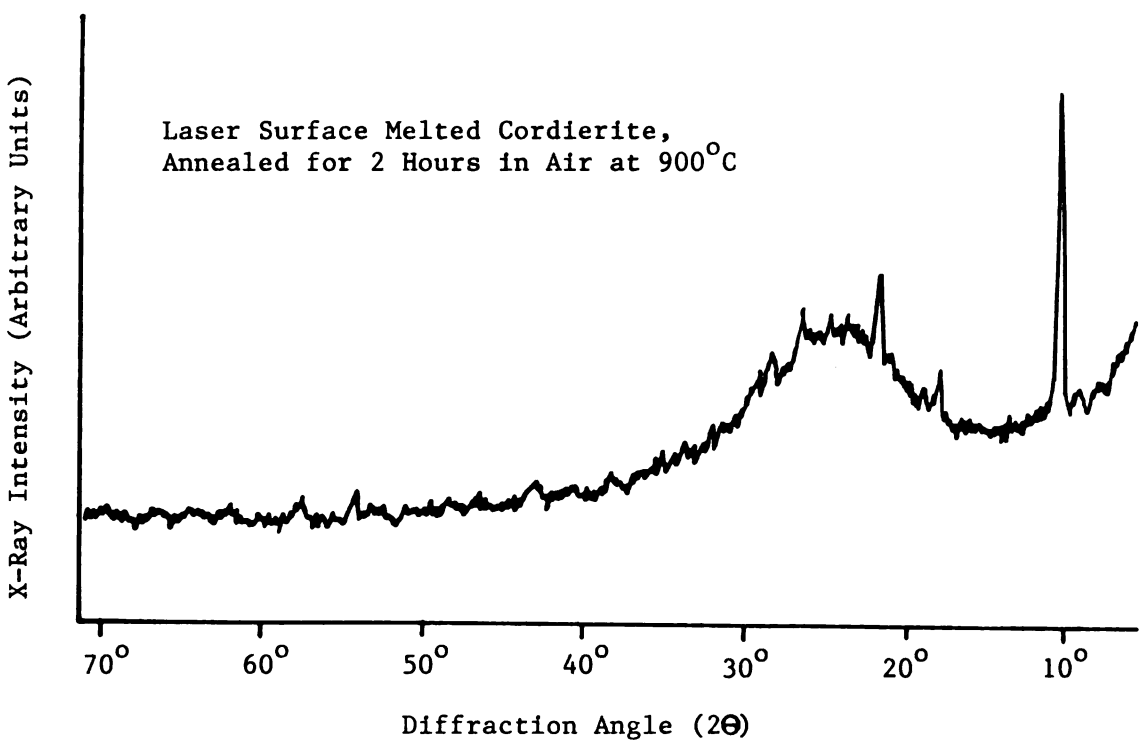

Figure 53. Diffractometer trace of laser-treated, 0.9mm thick cordierite specimen C22 after first 900°C anneal for 2 hours.

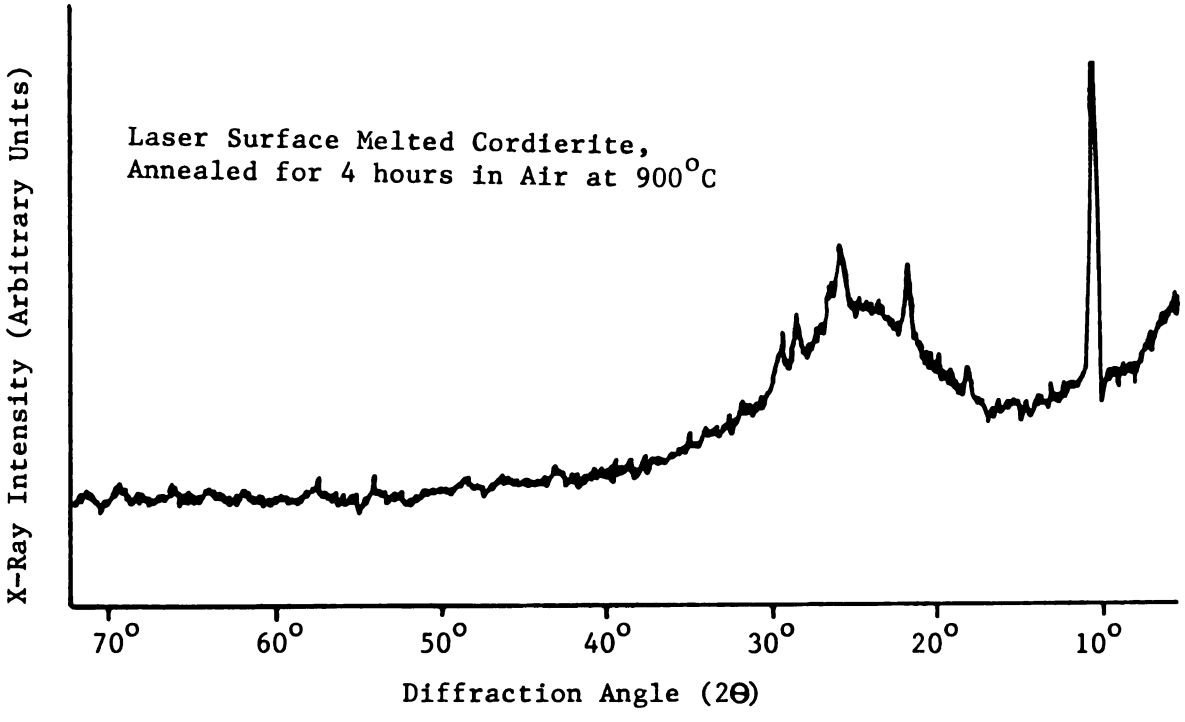

Figure 54. Diffractometer trace of laser-treated, 0.9mm thick cordierite specimen C22 after second 900°C anneal for 2 hours.

growing from the amorphous hump at 2 theta values of 21.6°, 26.4°, 28.4°, and 29.4°.

The x-ray traces in figures 55 and 56 remain a mystery as the x-ray diffraction results were a sensitive function of specimen orientation. The slightest shift or rotation of the sample would cause the results shown in these figures. Oddly enough, figures 55 and 56 are the x-ray diffraction results following a third thermal anneal at 900°C. A variety of specimen positions did not produce a reasonable trace. The previously mentioned cracking and surface depressions may have caused part of this problem.

Another 2 hour, 900° anneal on the same specimen (figure 57) gave a reasonable trace. The $2\theta = 10.2^{\circ}$ peak has not yet grown, in fact it has gotten slightly smaller. An extremely large peak at 25.6°, which does not correspond to either high or low cordierite has grown off the scale. The x-ray traces of figures 48 through 51 more effectively represent the annealing process. These results are discussed further in the Conclusions section.

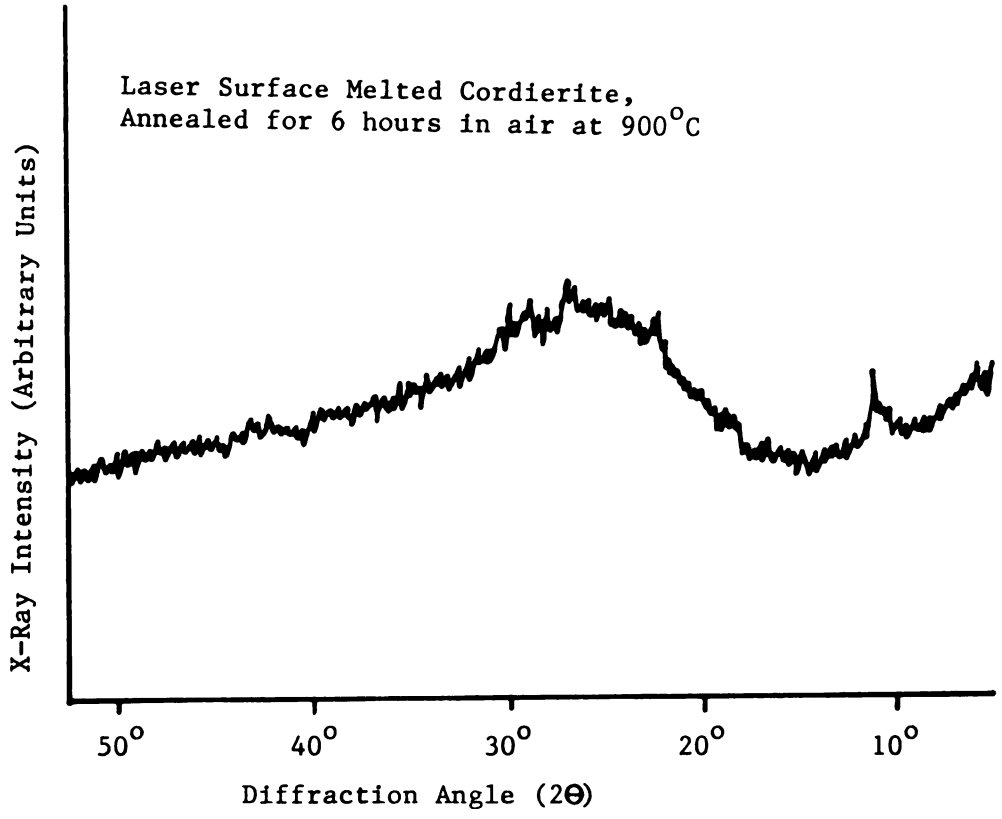

Figure 55. Diffractometer trace of laser-treated cordierite specimen C22 after third 900°C anneal for 2 hours.

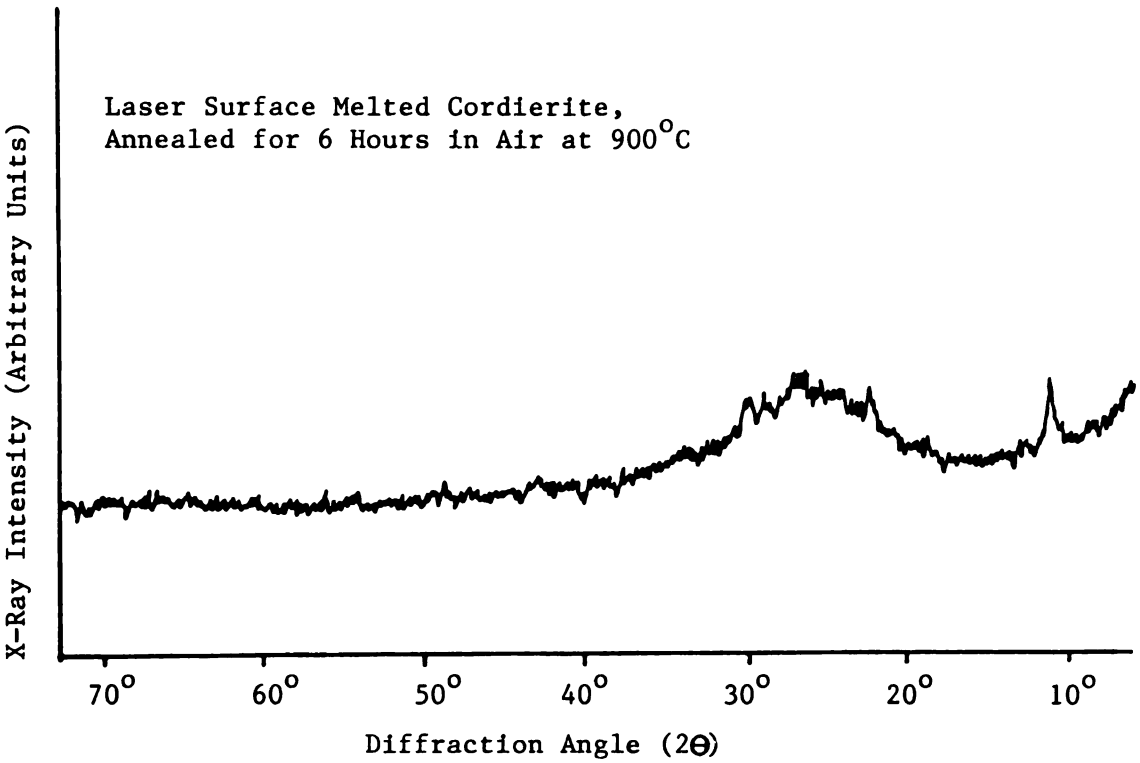

Figure 56. Diffractometer trace of laser-treated cordierite specimen C22 after third 900°C anneal for 2 hours.

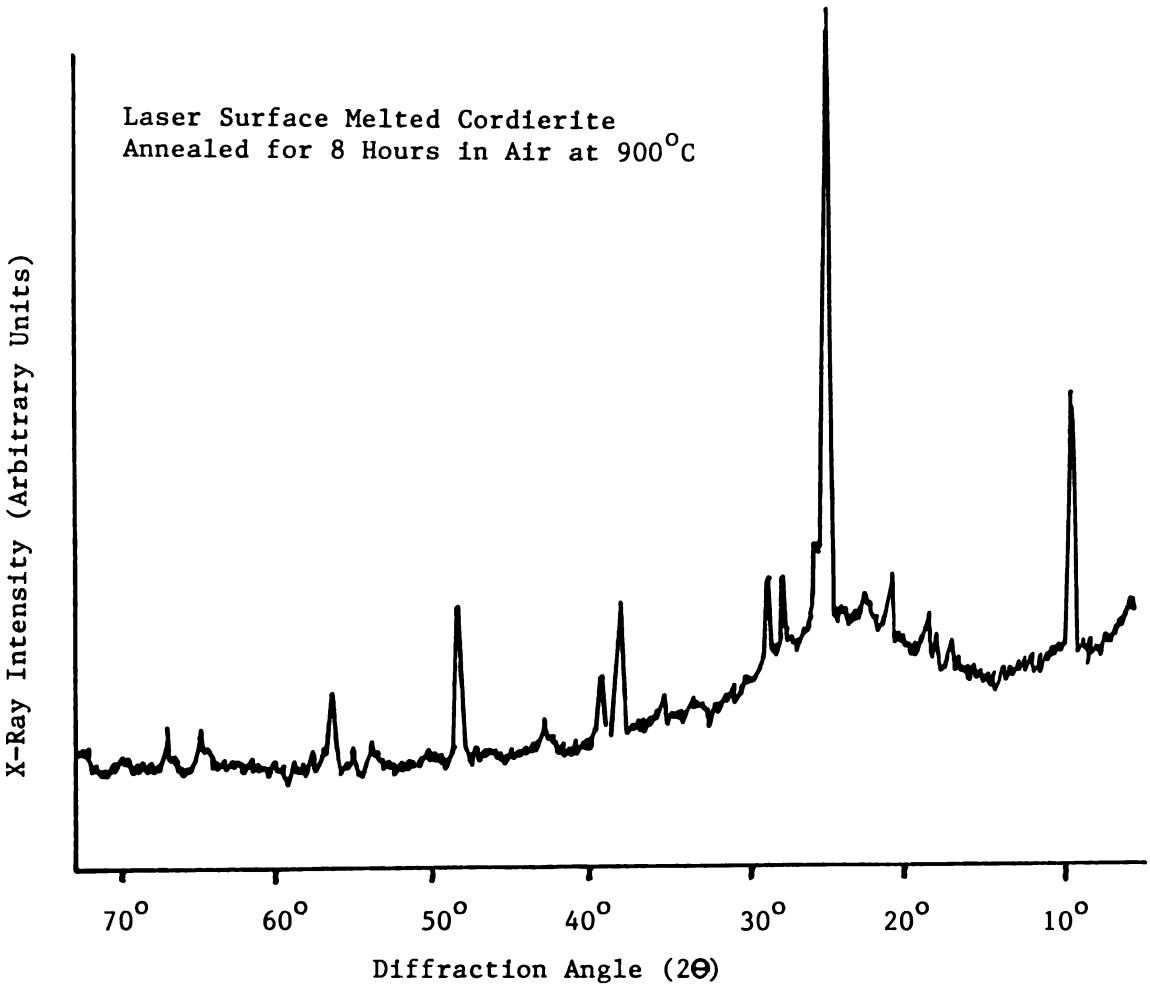

Figure 57. Diffractometer trace of laser-treated cordierite specimen C22 after fourth 900°C anneal for 2 hours.

4. CONCLUSIONS

The scanning electron micrographs presented in the Results and Discussion section of this thesis clearly suggest that an effective laser treatment of the cordierite substrates has taken place. The major problem inherent in the untreated substrates was porosity (on both the edges and surfaces). Such porosity in the cordierite can lead to undesireable water absorption.

Cutting the substrates with the CO_2 laser effectively eliminated porosity on the edges of the specimens. Surface melting reduced porosity on the surfaces of the specimens. Initially, surface melting also introduced a small number of cracks into the specimen surfaces. This was a problem encountered with the original X-Y table, since these cracks were not evident in the untreated cordierite.

A new X-Y table allowed the exploration of a wider range of surface processing parameters. After many different combinations of working distance, output power, and X-Y table speed, our goal was achieved. A crack-free melted layer as thin as 20 microns was produced.

The next step was to use these processing parameters to fabricate the "sandwich" specimen mentioned earlier. This was attempted and accomplished. The substrate was crack-free and likely sealed from the elements. The porous, as-recieved substrates can thus be corpletely

encased in a dense glassy "shell" which will likely protect the substrate against water absorption without greatly affecting the dielectric properties of the material. Water absorption characteristics have not yet been experimentally determined. These substrates could now be used for a multitude of outdoor industrial microwave applications.

Surface ripples normally observed after the laser treatment of metals do not exist after the laser treatment of cordierite. The profilometer results in this thesis (section 3.2) showed that the surface of the melted glassy layer is at least six times smoother than the surface of the as-received substrates. This is a very conservative estimate since much of the reduction in surface roughness is due to a reduction of porosity. Sub-micron pores, and their subsequent elimination will not register on the Dektak IIA because of the size of its stylus (25 microns in diameter). SEM micrographs (figures 11 through 29 in section 3.1) show that the melted cordierite surfaces indeed have a glassy, mirror-like finish. The absence of surface ripples may facilitate the metallization of the melted cordierite surfaces.

X-ray diffraction analysis determined the crystallographic nature of the untreated, laser-treated, and annealed surfaces.

The initial x-ray diffraction experiments were conducted on the as-recieved substrates to determine if, in fact, the material was cordierite. After careful inspection of the

diffraction traces of a specimen of each of the three thicknesses (0.3mm, 0.4mm, and 0.9mm), the material was found to be "high-cordierite". The x-ray data on the laser-melted surfaces were compared to published powder patterns in the National Bureau of Standards monographs. The d-spacings were nearly identical, indicating that high-cordierite was the predominant crystalline phase in the surface-melted cordierite.

X-ray diffraction experiments conducted on the laser-melted surface layer determined crystallinity. As was expected, due to the large amount of silica in the as-received material, the melted layer contained a large amount of glassy phase. An amorphous hump, characteristic of glasses, and the absence of any significant peaks led us to the conclusion that a glass was present.

Also present at this stage was a peak at $2\theta = 16.4^{o}$, which has a relative intensity of 48 in mullite. This was concluded since cordierite is an incongruently melting compound in the mullite phase field. This substantial mullite peak is not present in untreated "high-cordierite" and its disappearance upon annealing was expected.

Further annealing experiments showed the growth of high-cordierite x-ray peaks. The goal is to regain the crystallographic nature of the as-recieved material. The problem of thermal expansion mismatch could now be eliminated in the service environment. Both the melted layer

the porous inner-bulk of the substrate would behave similarly to changes in temperature and the interface could maintain its mechanical adhesion and the service life of the substrate would be greatly extended.

The results of this study suggest that the laser surface melting characteristics of cordierite are worthy of further investigation, and that this treated substrate will have a wide variety of service applications.

PHYSICAL, MECHANICAL, THERMAL, AND ELECTRICAL PROPERTIES OF CORDIERITE ($2MgO \cdot 2Al_2O_3 \cdot 5SiO_2$) [31]

	Reference [32]	Reference [33]	Reference [34]	Reference [35]
PHYSICAL				
Crystal structure	Orthorhombic			
Density g/cm^3*	2.51	2.3	2.1	1.8
Melting point C	1,471			
Gas permeability		0-1	10-15	14-17
MECHANICAL				
Modulus of elasticity psi		$17X10^6$	$8.8X10^6$	
Modulus of rigidity psi		$7X10^6$	$3.8X10^6$	
Poisson's ratio		0.21	0.17	
Flexural Strength psi(25 C)	16,000	15,000	8,000	3,400
Compressive strength psi (25 C)	50,000	50,000	30,000	18,500
Tensile strength psi(25 C)	7,800		3,500	2,500
Impact resistance in.-lb. (Charpy)	4.3	4.0	2.5	2.5
THERMAL				
Coeff. of expansion 10^{-6}/ C				
25-400 C		2.4	2.2	0.6

PHYSICAL, MECHANICAL, THERMAL, AND ELECTRICAL PROPERTIES OF CORDIERITE ($2MgO\ 2Al_2O_3\ 5SiO_2$) [31]

	Reference [32]	Reference [33]	Reference [34]	Reference [35]
Coeff. of expansion 10^{-6}/ C (cont.)				
25-700 C		3.3	2.8	1.5
Conductivity cal/(sec)(cm^2)(C/cm)				
20 C		0.0077	0.0043	
300 C		0.0062	0.0041	
ELECTRICAL				
Dielectric constant at 25 C				
1 kHz		5.3	5.0	4.1
10 MHz			4.9	
Dissipation factor at 25 C (1kHz)		0.0047	0.004	0.012
Loss factor at 25 C (1 kHz)		0.025	0.020	0.048
Dielectric strength (AC volts/mil)				
0.250 in. thick		200	100	60

*The theoretical (x-ray) density of cordierite is 2.54 g/cc [37].

Table A1 (continued)

Appendix B

Table B1. Selected Laser Processing Parameters and Results

Working* Distance (in.)	Table Speed (in/min)	Output Power (Watts)	Power Density ($J/m^2 sec$)	Laser	Result**
4.4	18.9	35	$1.53X10^6$	YAG	(1)
4.4	18.9	40	$1.71X10^6$	YAG	(1)
4.4	18.9	45	$1.88X10^6$	YAG	(3)
4.4	18.9	60	$2.39X10^6$	YAG	(2)
4.4	18.9	75	$2.90X10^6$	YAG	(2)
5.5	100	600	$1.63X10^6$	CO_2	(1)
5.5***	80	700	$2.31X10^6$	CO_2	(3)
5.5	60	650	$2.73X10^6$	CO_2	(4)
5.5	40	700	$4.00X10^6$	CO_2	(4)
5.5	60	950	$4.00X10^6$	CO_2	(2)
4.0	17.7	550	$7.50X10^6$	CO_2	(2)
0.4	18.9	600	$1.10X10^7$	CO_2	(5)
Focal Point	80	700	$8.10X10^7$	CO_2	(5)

*For the carbon dioxide laser, the beam diameter can be obtained using the working distance and the beam focussing chart given in figure 4b of this thesis.

**Results:

(1) No Melting
(2) Slight Degree of Melting with Cracks
(3) Slight Degree of Melting without Cracks (Optimal Parameters)
(4) Complete Melting (Destruction of Specimen)
(5) CO_2 Laser Cut

***These parameters were used to fabricate specimens C11-C13.

Appendix C

Table C1. Dektak IIA's Specifications

Data Display Screen	229 mm (9 in) (diagonal)
Measurement Display Range	200 to 655,000 angstroms
Vertical Resolution	5 angstroms (0.5 nm)
Scan Speed Ranges	Low, Medium, High
Scan Length	50 microns to 30 mm
Scan Time	4 to 65 seconds (depending on scan distance and speed)
Leveling	Automatic and Semiautomatic
Stylus Radius (standard)	12.5 microns
Stylus Tracking Force	10 to 50 mg (field adjustable)
Maximum Sample Thickness	20 mm
Sample Stage Diameter	127 mm
Sample Stage Rotation	continuous
Sample Stage Translation (from center position)	
X axis (left to right)	+/- 10 mm
Y axis (forward to back)	+10 mm, -70mm
Sample Stage Tilt	+/- 3 degrees
Video Camera	90X
Thermal Printer Speed	15 seconds per printout
Printout Size	11cm x 17cm
Overall Dimensions (width x depth x height)	
Control Console:	40.1 cm x 51.3 cm x 27.4 cm
Scanning Head:	26.2 cm x 35.6 cm x 50.8 cm
Thermal Printer:	26.2 cm x 19.1 cm x 9.7 cm

Table C2. Dektak IIA's Scanning Speed Range

Scan Length, microns	SCAN SPEED RANGE					
	Low		Medium		High	
	microns per sample	Number of samples per scan	microns per sample	Number of samples per scan	microns per sample	Number of samples per scan
20,001-30,000	50	400-600	*	*	*	*
10,001-20,000	20	500-1000	40	250-500	*	*
5,001-10,000	10	500-1000	20	250-500	50	100-200
2,001-5,000	5	400-1000	10	200-500	25	80-200
1,001-2,000	2	500-1000	4	250-500	10	100-200
501-1,000	1	500-1000	2	250-500	5	100-200
201-500	0.5	400-1000	1	200-500	2.5	80-200
101-200	0.2	500-1000	0.4	250-500	1	100-200
51-100	0.1	500-1000	0.2	250-500	0.5	100-200
50	0.05	1000	0.1	500	0.25	200

* Invalid speed range

Appendix D

Table D1. X-Ray Diffraction Data for "High-Cordierite" [36]

hkl	d	I*
	A	
100	8.48	100
110	4.89	32
002	4.679	15
102	4.094	51
112	3.379	57
202	3.138	66
211	3.027	86
212	2.640	26
220	2.441	6
302	2.414	4
004	2.338	12
311	2.276	5
213	2.231	5
222	2.165	6
114	2.108	8
312	2.098	12
204	2.046	3
320	1.941	8
402	1.927	6
321	1.901	3
313	1.875	15
410	1.846	6
411	1.811	7
304	1.800	9
412	1.718	3
224	1.6882	28
314	1.6559	3
323	1.6472	4
330	1.6286	4
215	1.6150	3
420	1.5988	6
413	1.5885	9
404	1.5690	2
006	1.5584	3
332	1.5377	3
324	1.4953	8
116	1.4852	5
315,206	1.4625	5

*Normalized Intensities of Diffraction Peaks, 1961 National Bureau of Standards. Cu, 1.5405A at 25°C [36].

Table D2. X-Ray Diffraction Data for "Low-Cordierite" [36]

hkl	d	I*	hkl	d	I*
	A				
020	8.52	98	243	2.234	4
110	8.45	100	313	2.225	5
130	4.91	28	262	2.173	5
200	4.86	10	402	2.156	2
002	4.67	13	080	2.132	<1
040	4.27	1	172	2.107	11
112	4.09	52	204,352	2.102	11
221	3.84	1	422	2.091	8
132	3.381	51	224	2.044	2
202	3.369	38	280	1.954	4
042	3.149	25	370	1.948	6
222	3.132	56	082	1.942	5
151	3.039	64	510	1.932	3
241	3.035	64	263,442	1.925	4
311	3.012	56	281	1.912	<1
152	2.650	22	314,173	1.882	8
242	2.644	22	353	1.876	11
312	2.637	12	423	1.870	10
260	2.454	4	460	1.848	1
400	2.430	5	530	1.839	2
332	2.409	3	115	1.825	<1
261	2.373	1	461	1.811	4
004	2.334	11	064	1.804	7
171	2.293	2	334	1.798	8
351	2.278	2	225,0.10.0	1.706	6
			264	1.691	18

*Normalized Intensities of Diffraction Peaks, 1961 National Bureau of Standards. Cu, 1.5405A at 25°C [36].

Table D3. X-Ray Diffraction Data for Mullite [36]

hkl	d	I*	hkl	d	I*
	A				
110	5.39	48	241	1.4731	<2
200	3.774	8	421	1.4605	7
120	3.428	96	002	1.4421	17
210	3.390	100	250	1.4240	3
001	2.886	21	520	1.4046	7
220	2.694	40	112	1.3932	<2
111	2.542	52	341	1.3494	6
130	2.428	13	440	1.3462	6
310	2.393	<2	151	1.3356	12
021	2.308	3	122	1.3290	5
201	2.292	19	212	1.3266	5
121	2.206	61	511	1.3172	4
230	2.121	23	350	1.3120	3
320	2.106	7	530	1.3004	4
221	1.969	2	060	1.2814	7
040	1.923	2	251	1.2771	13
400	1.887	8	222	1.2714	6
140	1.863	<2	521	1.2630	12
311	1.841	10	600	1.2574	<2
330	1.7954	<2	132	1.2396	6
240	1.7125	6	312	1.2349	2
321	1.7001	14	441	1.2199	2
420	1.6940	10	260	1.2131	<2
041	1.5999	20	232	1.1924	4
401	1.5786	11	531	1.1855	3
141	1.5644	2	402	1.1457	<2
411	1.5461	2	261	1.1190	1
331	1.5242	37	242	1.1032	4
150	1.5067	<2	422	1.0981	5
510	1.4811	<2	270	1.0548	<2
			171	1.0172	4
			252	1.0133	4
			370,522	1.0065	8

*Normalized Intensities of Diffraction Peaks, 1961 National Bureau of Standards. Internal Standard, Tungsten, a=3.1648A Cu, 1.5405A at 25°C [36].

Appendix E

Table E1. Comparison of X-Ray Diffraction Data for As-Received Cordierite

As-Received Specimen			Published Values					
2	I/I_o	d	d [37]	d [36]	d [38]	I/I_o [37]	I/I_o [36]	I/I_o [38]
10.2	100	8.67	8.48	8.48	8.48	100	100	100
17.8	25	4.98	4.89	4.89	4.89	30	32	32
18.7	10	4.74	4.68	4.68	4.68	16	15	15
21.6	45	4.11	4.10	4.10	4.09	50	51	51
26.4	49	3.38	3.38	3.38	3.38	55	57	57
28.4	55	3.14	3.14	3.14	3.14	65	66	66
29.4	64	3.04	3.03	3.03	3.03	85	86	86
33.8	18	2.65	2.64	2.64	2.64	25	26	26
36.9	4	2.44	2.44	2.44	2.44	6	6	6
38.6	8	2.33	2.34	2.34	2.34	12	12	12
39.5	2	2.28	2.28	2.28	2.28	6	5	5
40.5	2	2.23	2.23	2.23	2.23	6	5	5
41.5	2	2.18	2.17	2.17	2.17	6	6	6
43.0	10	2.10	2.10	2.11	2.11	8	8	8
44.2	1.5	2.05	2.05	2.05	2.05	4	3	3
46.6	3	1.95	1.94	1.94	1.94	8	8	8
48.5	8	1.88	1.88	1.88	1.88	16	15	15
50.5	5	1.81	1.80	1.80	1.80	10	9	9
54.2	18	1.69	1.69	1.69	1.69	30	28	28
57.7	5	1.60	1.60	1.60	1.60	6	6	6
62.1	4	1.49	1.49	1.49	1.49	8	8	8

Table E2. Comparison of X-Ray Diffraction Data for Cordierite Specimens with Surface Treatment and Subsequent Anneals.

As-Received		Laser-Treated Specimen C21		1st 900°C Anneal Specimen C21		2nd 900°C Anneal Specimen C21	
2	I/I_o d	I/I_o	d	I/I_o	d	I/I_o	d
10.2	100 8.67	no peak		9	8.67	90	8.67
16.4	no peak	9	5.41	no peak		3	5.41
17.8	25 4.98	no peak		no peak		15	4.98
18.7	10 4.74	no peak		no peak		7	4.74
21.6	45 4.11	no peak		4	4.11	16	4.11
26.4	49 3.38	7	3.38	10	3.38	11	3.38
28.4	55 3.14	4	3.14	10	3.14	7	3.14
29.4	64 3.04	5	3.04	13	3.04	5	3.04
33.8	18 2.65	12	2.65	5	2.65	2	2.65

Appendix F

Portion of the Magnesia-Alumina-Silica Ternary Phase Diagram Showing Cordierite Composition Point and Phase Field.

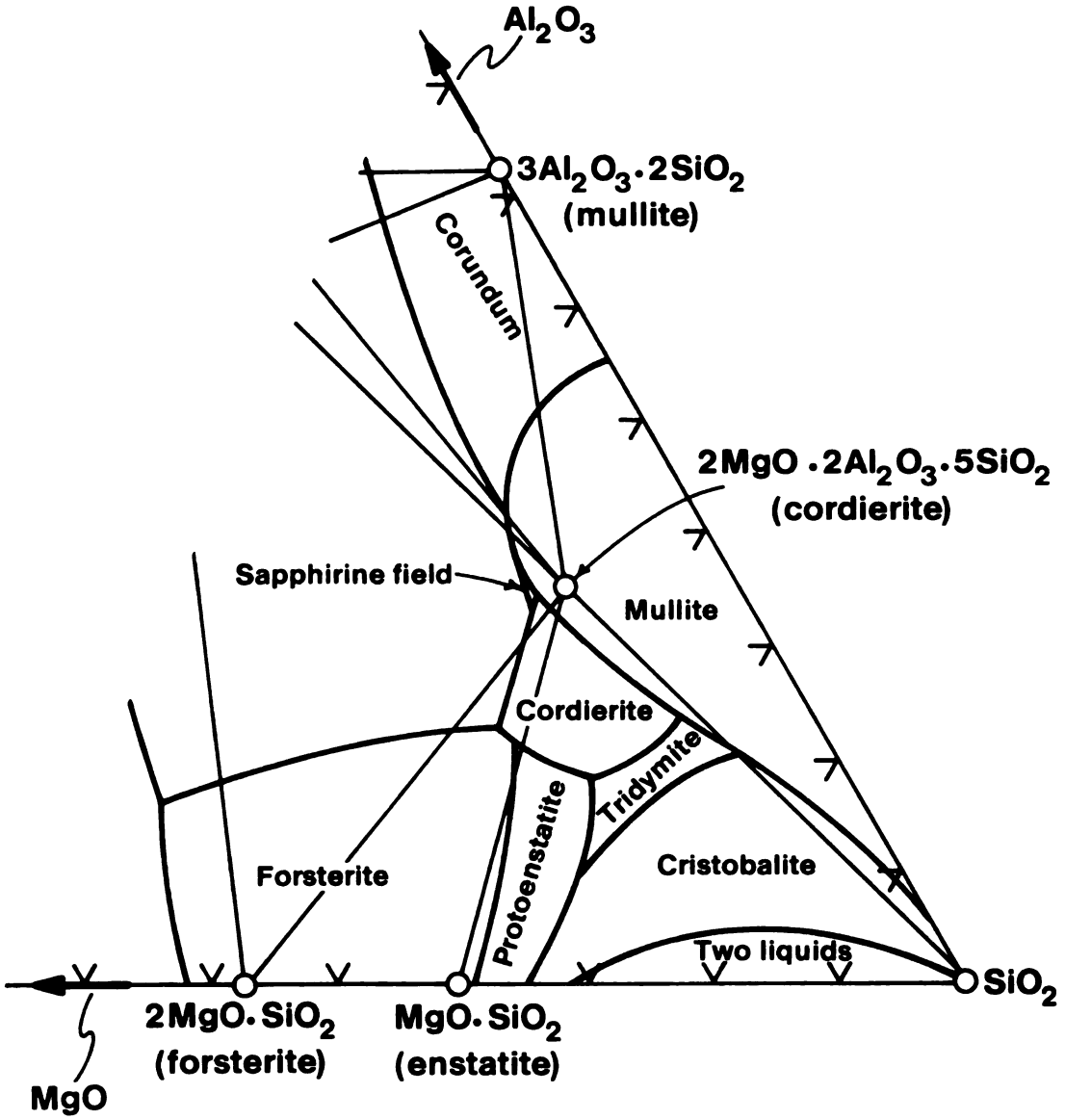

Figure F1. Ternary phase diagram showing 2:2:5 cordierite existing in the mullite phase field (after W. D. Kingery et. al., [2]).

REFERENCES

1. D. G. Carson, G. R. Rossman, and R. W. Vaughan, "Orientation and Motion of Water Molecules in Cordierite", Phys. Chem. Minerals., 8: 14, 1982.

2. W. D. Kingery, H. K. Bowen, D. R. Uhlmann, p. 310 in Introduction to Ceramics, Second Edition, John Wiley & Sons, Inc., 1976.

3. C. J. Fairbanks, H. L. Lee, and D. P. H. Hasselman, "Effect of Crystallites on Thermal Shock Resistance of Cordierite Glass Ceramics", Communications of the American Ceramic Society, C-236, 1984.

4. D. I. Evans, "Thermal Expansions and Chemical Modifications of Cordierite", Am. Ceram. Soc. Bull., 59[3]: 357-361, 1980.

5. D. W. Richerson, p. 381 in Modern Ceramic Engineering, Marcel Dekker, Inc. 1982.

6. Y. Hirose, H. Doi, and O. Kamigaito, "Thermal Expansion of Hot-Pressed Cordierite Glass Ceramics" Journal of Materials Science Letters, 3: 153, 1984.

7. C. T. Lynch, p. 356 in the Handbook of Materials Science, CRC Press, Inc. 1975.

8. D. Cronin, Trans-Tech Inc., Adamstown Maryland. A personal communication, August, 1989.

9. W. A. Yarbrough, T. R. Gururaja, and L. E. Cross, "Materials for IC Packaging With Very Low Permittivity Via Colloidal Sol-Gel Processing", Am. Ceram. Soc. Bull., 66: 692-698, 1987.

10. E. Case, Associate Professor, Michigan State University, East Lansing, Michigan. A personal communication, June, 1987.

11. I. M. Lachman, R. D. Bagley, and R. M. Lewis, "Thermal Expansion of Extruded Cordierite Ceramics", Am. Ceram. Soc. Bull., 60[2]: 205, 1981.

12. C. S. Rossington, An Indentation Technique to Measure the Fracture Toughness of Thin Film/Substrate Interfaces, M.S. Thesis, University of California, Berkeley, 1983.

13. F. A. Jenkins and H. E. White, p.446 and 520 in Fundamentals of Optics, Third edition, McGraw-Hill Book Co. Inc., 1957.

14. M. Born and E. Wolf, p.611 in Principles of Optics, Fourth edition, Pergamon Press. 1970.

15. W. T. Walter, N. Solimene, K. Park, T. H. Kim, and K. Mukherjee, "Optical Properties of Metal Surfaces During Laser Irradiation", 3rd Advanced Materials Workshop. Sept.15-17, 1986.

16. J. Mazumder and W. M. Steen, "Heat Transfer Model For cw Laser Material Processing", J. Appl. Phys. 51[2]: 941, 1980.

17. S. M. Copley, "Laser Materials Transformations", International Congress on Applications of Lasers and Electro-Optics (ICALEO), Laser Institute of America (L.I.A.), 31: 1-7,1982.

18. P. Gay and G. Manassero, "Absorption Measurements for High Power Laser Material Processing", ICALEO, L.I.A., 36: 224-228, 1983.

19. R. Jeanloz and D. L. Heinz, "Measurement of the Temperature Distribution in CW-Laser heated materials", ICALEO, L.I.A., 45: 239, 1985.

20. H. S. Carslaw and J. C. Jaeger, p.284 in Conduction of Heat in Solids, Second Edition, Oxford University Press, 1959.

21. R. D. Dixon and G. K. Lewis, "The Influence of a Plasma During Laser Welding", ICALEO, L.I.A., 38: 157-162, 1983.

22. M. Hutchinson, K. T. Lee, W. C. Murphy, A. C. Beri, and T. F. George, "Theoretical Aspects of Laser Induced Periodic Surface Structure Formation", p.389 in Laser-Controlled Chemical Processing of Surfaces, Vol.29, 1984.

23. G. N. Maracas, G. L. Harris, C. A. Lee, and R. A. McFarlane, "On the Origin of Periodic Surface Structure of Laser-Annealed Semiconductors", Appl. Phys. Lett., 33: 453, 1978.

24. G. S. Fischman, C. H. Chen, J. M. Rigsbee, and S. D. Brown, "Character of Laser-Glazed, Plasma-Sprayed Zirconia Coatings on Stainless Steel Substrates", Ceramic Engineering and Science Proceedings, 6: 908-917, 1985.

25. I. Zaplatynsky, "Performance of Laser Glazed ZrO_2 TBC's in Cyclic Oxidation and Corrosion Burner Test Rigs", NASA Technical Memorandum TM-82830, NASA Lewis Research Center, Cleveland, OH. 1982.

26. M. L. Capp and J. M. Rigsbee, "Laser Processing of Plasma-Sprayed Coatings", Mater. Sci. Eng., 62: 49-56, 1984.

27. From the British Oxygen Company's Series 9000 2 Kilowatt Carbon Dioxide Laser Machine, Operators Manual, page 3.

28. R. Saunders, W. Shiner, T. Conklin, D. Bennett, and G. Thoman, p.42 in Lasers - Operation, Equipment, Application, and Design, McGraw-Hill Book Co., 1980.

29. From the Polaron Semiconductor Sputter Coater (serial number E5175), Instruction Manual. Polaron Equipment Limited, pp. 5-6.

30. B. D. Cullity, p.189 in Elements of X-Ray Diffraction, Second edition, Addison-Wesley Publishing Co., Inc., 1978.

31. C. T. Lynch, pp. 374-376 in the Handbook of Materials Science, CRC Press, Inc., Volume 2, 1975.

32. Engineering Properties of Selected Ceramic Materials, American Ceramic Society, Columbus, Ohio. 5.4.1-1, 1966.

33. American Lava Corporation. Chart Number 711 (Alsimag 701). Cited in reference 18.

34. American Lava Corporation. Chart Number 711 (Alsimag 202). Cited in reference 18.

35. American Lava Corporation. Chart Number 711 (Alsimag 447). Cited in reference 18.

36. H. E. Swanson, M. C. Morris, R. P. Stinchfield, and E. H. Evans, Standard X-Ray Diffraction Powder Patterns, NBS Monograph 25, section 1. pp.28-29, 1962.

37. Powder Diffraction File - Inorganic, Joint Committee on Powder Diffraction Standards, 12: 272, 1972.

38. W. Schreyer and J. F. Schairer, "Compositions and Structural States of Anhydrous Mg-Cordierites: A Re-Investigation of the Central Part of the System $MgO-Al_2O_3-SiO_2$", J. Petrol., 2: 366, 1961.

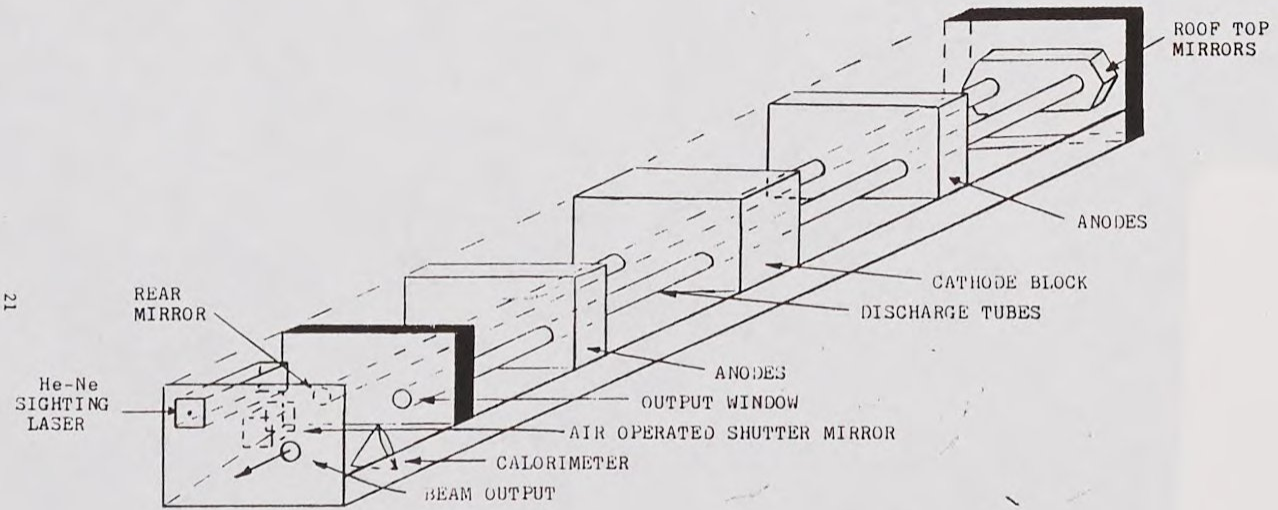

Figure 2. General view of CO_2 laser head.

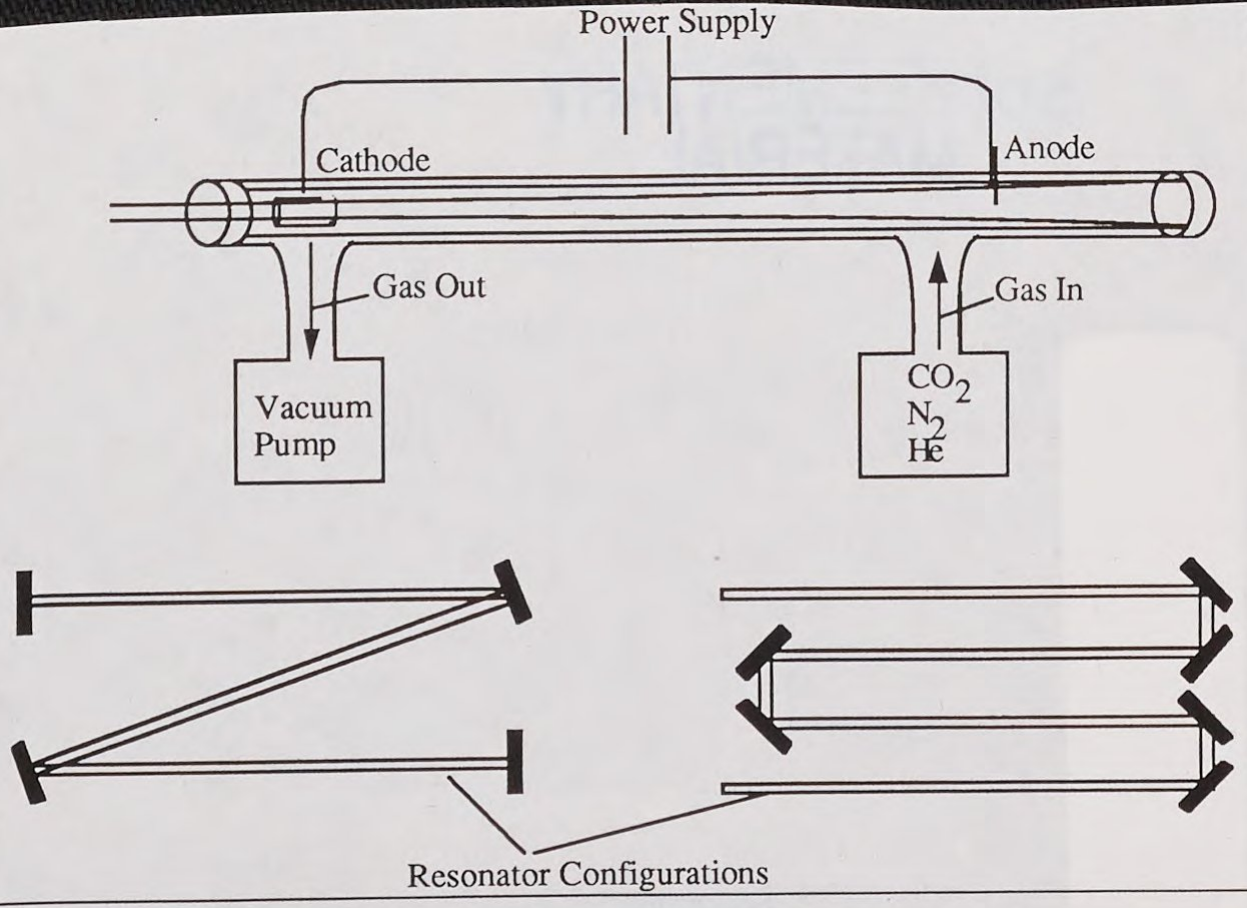

FIGURE 2.11 Axial Flow CO_2 Laser

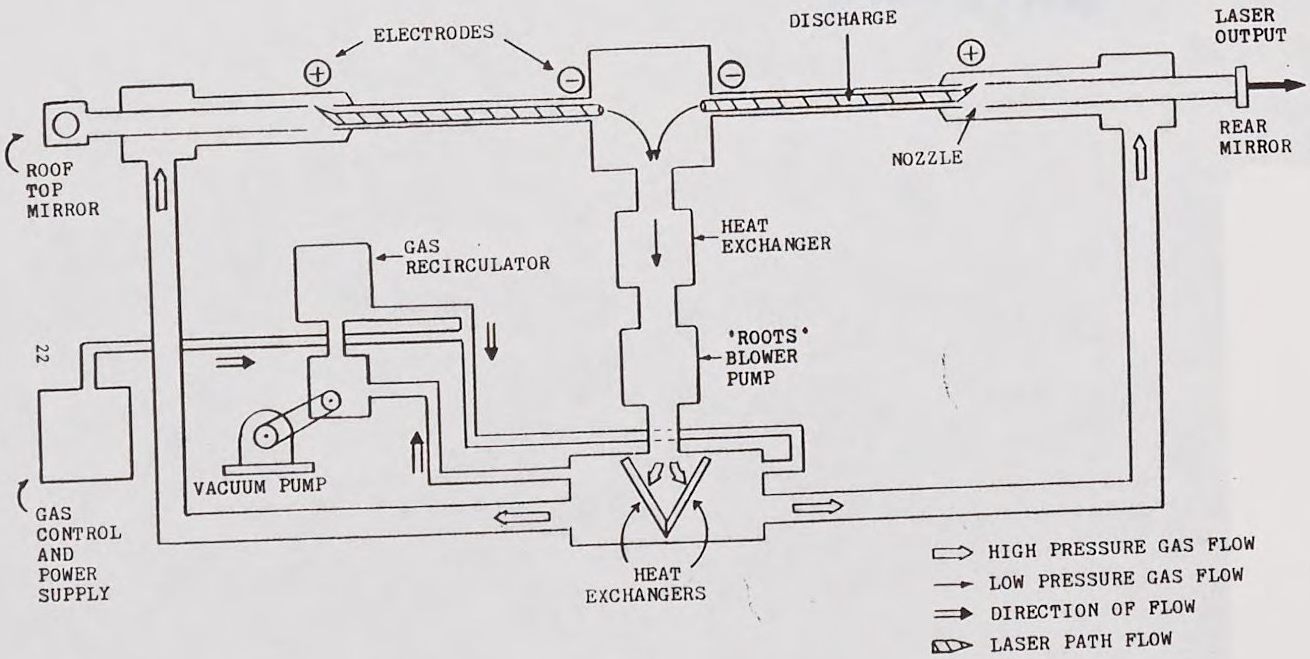

Figure 3. Gas and discharge paths of the CO_2 laser.

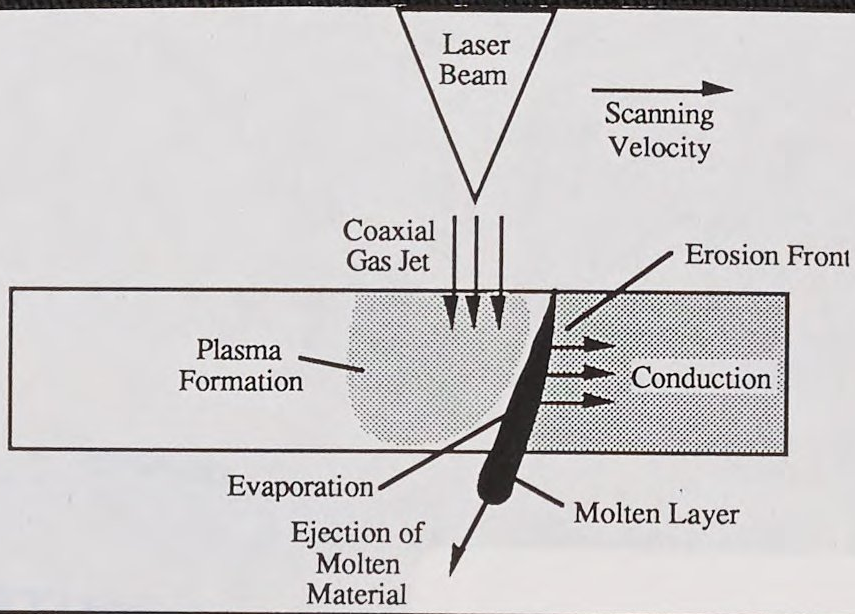

FIGURE 3.4 Laser Through-Cutting

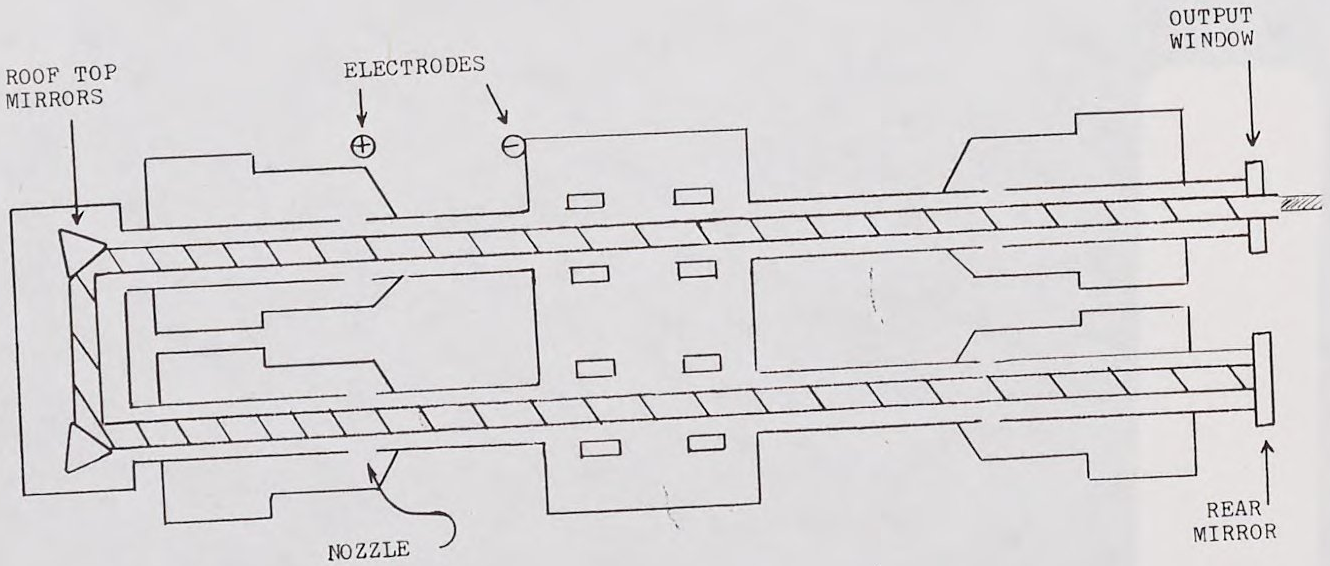

Figure 4a. Overhead view of CO_2 laser path.

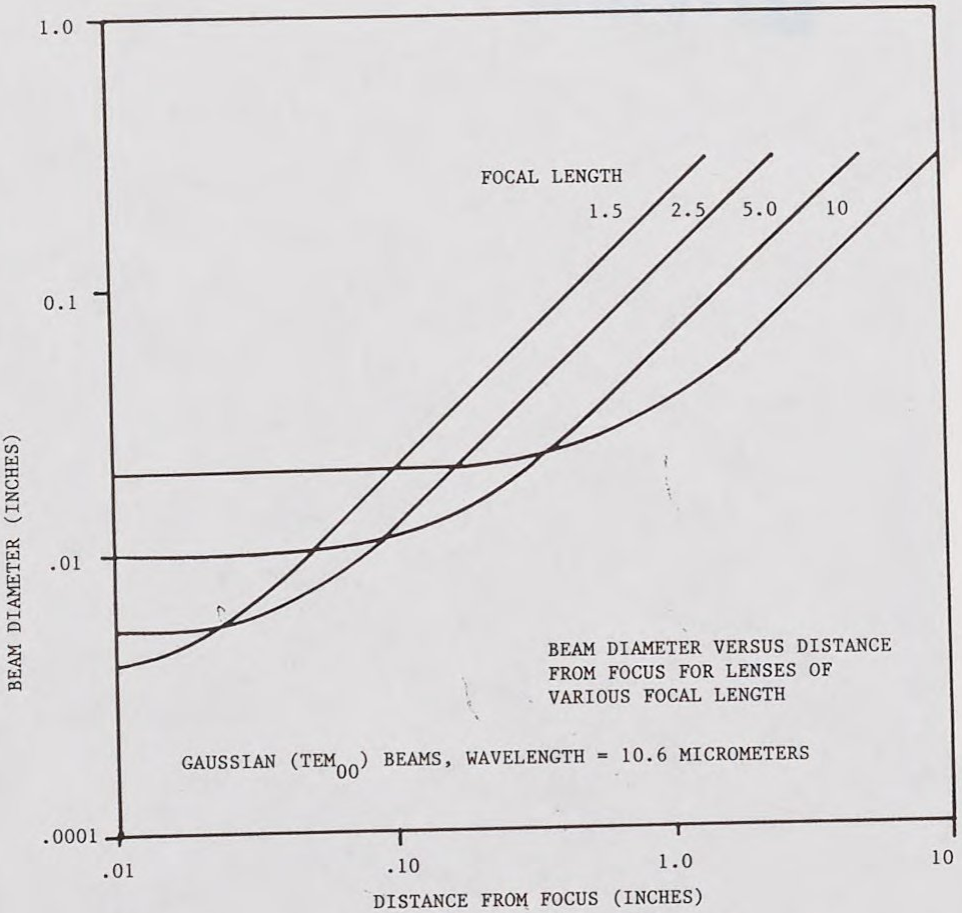

Figure 4b. Beam focussing chart which allows for the determination of laser beam spot size at various points in the path of the laser beam. [28]

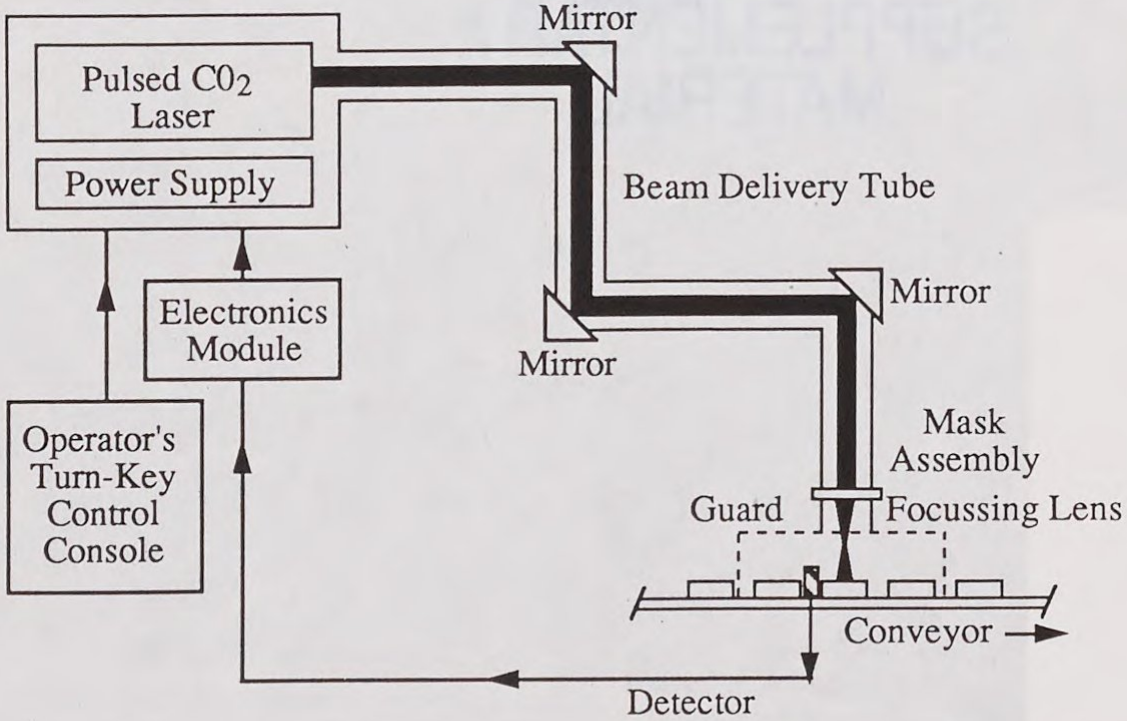

FIGURE 6.11 Setup for Laser Marking Equipment [25]

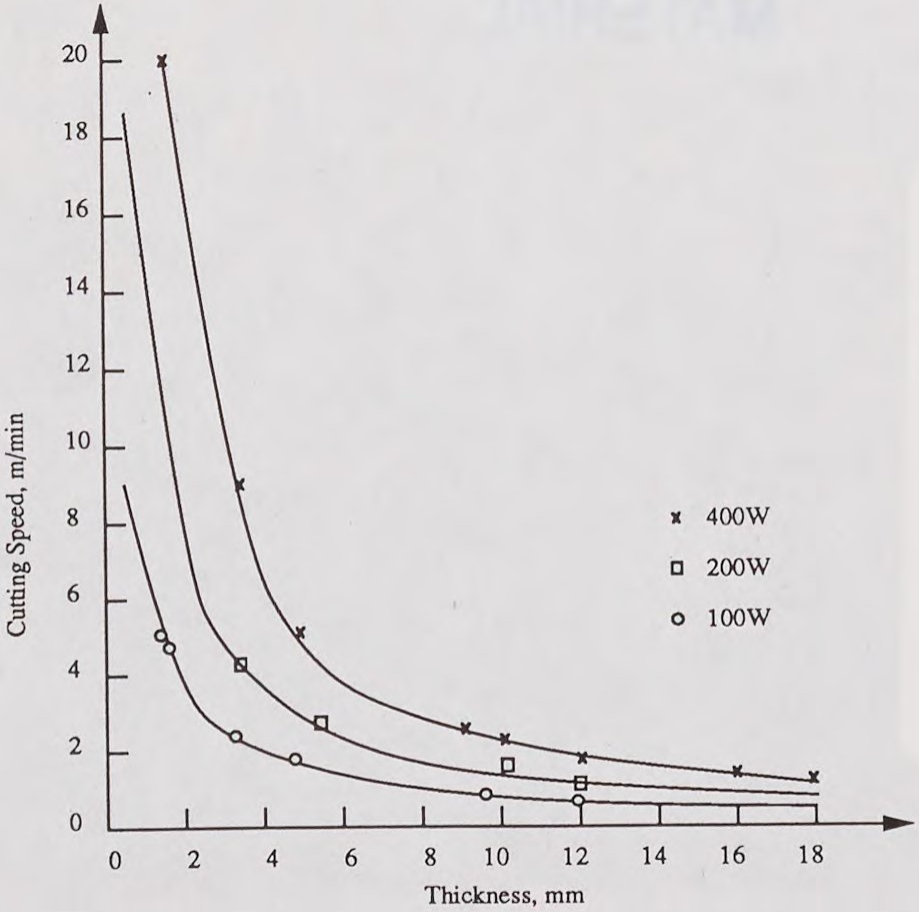

FIGURE 6.30 Cutting Speed vs. Workpiece Thickness for Acrylic

Pocket Insert 8 Figures
Fig. 2, 2.11, 3, 3.4, 4a, 4b, 6.11, 6.30